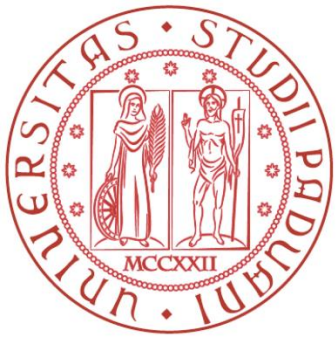

UNIVERSITA' DEGLI STUDI DI PADOVA

Dipartimento di Fisica e Astronomia "Galileo Galilei"

Corso di Laurea Magistrale in Fisica

Optimization of an advanced optical imaging apparatus suitable for intravital multiphoton microscopy

Relatore
Mario Bortolozzi

Laureanda
Chiara Nardin

Correlatore
Fabio Mammano

Anno accademico 2014/2015

a Tommaso e Giacomo

SOMMARIO

Il presente lavoro di tesi illustra l'esperienza svolta presso l'Istituto Veneto di Medicina Molecolare di Padova (V.I.M.M.). Lo scopo dell'attività di laboratorio è stato l'ottimizzazione di un microscopio *laser scanning* a due fotoni, proprietà del Dipartimento di Fisica e Astronomia, attraverso l'implementazione di tecniche di microscopia avanzate, quali la microscopia *multicolor multiphoton* e la nanoscopia *STED*. Una volta ottimizzato, lo strumento potrà essere sfruttato per l'imaging intravitale in modelli animali e costituirà uno strumento senza precedenti per lo studio dei processi biologici *in vivo* sulla nano scala, con la possibilità di osservare contemporaneamente dettagli diversi del campione biologico in esame. Il lavoro di tesi è consistito nell'assemblaggio, taratura ed ottimizzazione di un banco ottico che permettesse di generare due fasci laser pulsati opportuni per generare effetti di florescenza in multicolor e STED. Le due modalità di imaging richiedono configurazioni ottiche intercambiabili, la cui progettazione è stata parte del lavoro di tesi. Le nuove potenzialità acquisite dal microscopio multifotone sono state validate su campioni fluorescenti, in attesa di caratterizzarne le performance direttamente su modelli animali. Un setup di imaging con tali potenzialità è ciò che attualmente manca a Padova nel campo della ricerca contro il cancro per raggiungere una più profonda comprensione dei processi biologici del microambiente tumorale.

RINGRAZIAMENTI

Desidero ringraziare *in primis* Michele Gintoli, che durante il mio lavoro di tesi ha sempre risposto pazientemente alle mie domande e chiarificato i miei dubbi; Andrea Filippi, per aver condiviso con me quest'esperienza di primo avvicinamento al mondo della ricerca e di introduzione nel campo della microscopia ottica.

Ringrazio Valentina Scattolini, Giulia Crispino e Alessandro Leparulo (V.I.M.M.) per il loro fondamentale aiuto nella preparazione dei campioni su cui testare l'apparato di imaging e verificare i risultati del mio lavoro.

Ringrazio Giorgio Delfitto e Luca Bacci (Dipartimento di Fisica e Astronomia) per la realizzazione del circuito ritardatore di fase, che mi ha permesso di svolgere uno fra i più importanti esperimenti del lavoro di tesi.

TABLE OF CONTENTS

TABLE OF FIGURES

LIST OF ABBREVIATIONS

VIMM	Venetian Institute of Molecular Medicine
IVM	Intravital Microscopy
PSF	Point Spread Function
MPM, (MPE)	Multiphoton (Excitation) Microscopy
2PE	Two Photon Excitation
1PA	One Photon Absorption
SHG	Second Harmonic Generation
THG	Third Harmonic Generation
SFG	Sum Frequency Generation
DFG	Difference Frequency Generation
STED	Stimulated-emission-depletion
FWHM	Full Width Half-Maximum
OPO	Optical Parametric Oscillator
PMT	Photomultiplier
QD	Quantum Dot
KDP	Ammonium Dihydrogen Phosphate
ADP	Potassium Dihydrogen Phosphate
S-H	Shack-Hartmann

INTRODUCTION

The aim of the present work is the optimization of a two-photon laser scanning microscope by means of simultaneous implementation of two advanced microscopy techniques, multicolor multiphoton microscopy and STED nanoscopy. Once optimized, the instrument will be suitable for intravital multiphoton imaging in live models, like mice, and will be a great resource for biomedical studies.

The possibility of imaging biological processes in living multicellular organisms constitutes the basis of present and future research in biomedical fields, such as neurobiology, immunology and cancer biology. Intravital microscopy (IVM), the term we refer to this practice, has an enormous impact on cell biology studies, opening the way to direct observations of dynamic i*n vivo* processes not only in live tissues, but also at cellular and subcellular scales.

The first attempt to perform imaging in live animals dates back to the nineteenth century, when the available technique was the brightfield transillumination (1). This approach has been used for over a century, until the development of technologies allowed fundamental improvements in the direction of high-resolution cellular processes investigation. First of all, scientists obtained access to tissues not directly observable from the outside, by implanting optically transparent windows on model organisms, often mice (2). Subsequently, the introduction of fluorescence microscopy permitted to follow the dynamics of single cells and subcellular structures.
In the last decades several techniques have been developed to carry out advanced IVM. In particular the use of femtosecond lasers, able to provide intensities in the order of tens GW per square centimeter but relatively low average powers (milliwatts), marked the beginning of a new class of optical observations, derived from time-varying polarization at higher order. This nonlinear polarization is currently produced by light pulses with temporal duration in the range of 10 fs. Multiphoton excitation microscopy (MPE), that achieved high contrast imaging in thick and scattering specimens, and STED microscopy, which broke the diffraction limit, with other not linear optical techniques are destined to supply increasing quality images of biological specimens.

The opportunities offered by IVM can be exploited in the study of tumor growth and its response to therapy; in particular, understanding cell-cell communication through intracellular signalling is now within reach. Cancer progression is a process that consists of alternated phases of deregulated cell growth and migration, resulting from an altered survival signalling due to interactions between cancer cells and the reactive tumor microenvironment (3). We define "tumor microenvironment", also called "stroma", as the tissue environment surrounding the

tumor, composed of supporting structures, extracellular matrix (ECM), vasculature, immune cells and other non-malignant cells. It has a fundamental and often ambiguous role in cancer invasion and migration: it is actively involved in cancer progression, undergoing modifications such as remodeling of blood and lymphatic vessels, new vessels construction, different organization of matrix proteins. This can produce a cancer promoting effect derived from adjacent environment, especially from vasculature, nerves, trafficking routes of leukocytes, along which the invading tumor cells move and spread (3). Simultaneous detection of tumor cells and physical microenvironment by means of intravital microscopy over time can disclose the key mechanisms of tumor growth and response to therapy. This kind of analysis becomes essential for a deeper comprehension of biological effects of anti-cancer treatments and for addressing the therapy approach. In conclusion, intravital superresolution microscopy can and will undoubtedly be exploited to advance our knowledge of tumor progression mechanisms and consequently to develop cures to oppose it. A high performance optical setup for intravital microscopy will have the chance to provide new insights in the scope of microenvironment and cancer interaction as well as cancer cell-cell signalling.

In the present thesis we propose to optimize the advanced optical imaging apparatus currently under construction in a laboratory of the Venetian Institute of Molecular Medicine of Padua. It is composed of a new laser scanning confocal multiphoton microscope fed by two laser beams and the connected beams conditioning optics. Starting from the optimization of the performance of each component in the setup, such as beam power modulation system, fluorescence signal acquisition, temporal and spatial overlap of the two beams, the further aim is to set the best conditions to perform intravital multicolor multiphoton microscopy deep into biological tissues. The new acquired potentialities of the imaging apparatus must be tested observing fixed biological samples, looking forward to characterize its capabilities in live models.

The first chapter provides an overview about the development of optical imaging techniques, from traditional fluorescence microscopy to more recent and advanced methods exploited in top research in physical and biomedical fields. In particular, the optical nonlinear phenomena which will be employed as imaging techniques in the apparatus are illustrated.

The second chapter contains the detailed description of each element in the setup, pointing out its functionality with respect to the final purpose of setting the conditions required to perform multicolor multiphoton microscopy or STED nanoscopy.

In the third chapter the methods for the beams alignment, temporal synchronization of pulses and beam analysis are elucidated.

The fourth chapter presents the achievements obtained in the setup optimization and exhibits the experimental results of the tests executed to verify the capability of the imaging apparatus to perform multicolor multiphoton microscopy.

1 INTRAVITAL MICROSCOPY TECHNIQUES

In this chapter, taking the first steps describing the foundations of conventional modern microscopy, we present the principles underling the techniques that will be implemented in the imaging setup of the laboratory. First of all, some non-linear optic effects of materials exploited in microscopy are described, such as multi-photon absorption and higher harmonic generation; secondly STED microscopy is illustrated, the imaging technique that improves resolution under the limit dictated by diffraction. Finally, we give an overview of how the potentialities of these technologies can be employed in biology and medicine.

1.1 FLUORESCENCE MICROSCOPY

The phenomenon of fluorescence in specific molecules, called "fluorophores", is the main tool used to image subcellular structures in biological studies. Spontaneous fluorescence emission is a radiative de-excitation mechanism through which a molecule, brought in a superior energy level S_1 by the absorption of a quantum of light, can reach again its ground state S_0.
When a fluorophore absorbs light energy, it is usually carried to a higher vibrational level of an excited state, for example S_1, but it rapidly reaches the lowest vibrational level of the same state, $S_1(0)$, by means of internal conversion. In this kind of vibrational relaxation the excess energy is transferred from vibrational to kinetic modes in the molecule or to its neighbours, with a characteristic time of 10^{-12} seconds. Later, many mechanisms can compete to de-excite the molecule to the ground state; if the process occurs through the emission of a photon after a period on the order of 10^{-9} seconds, it is termed spontaneous fluorescence emission. The sequence of processes is summed up in Figure 1.1.1a.

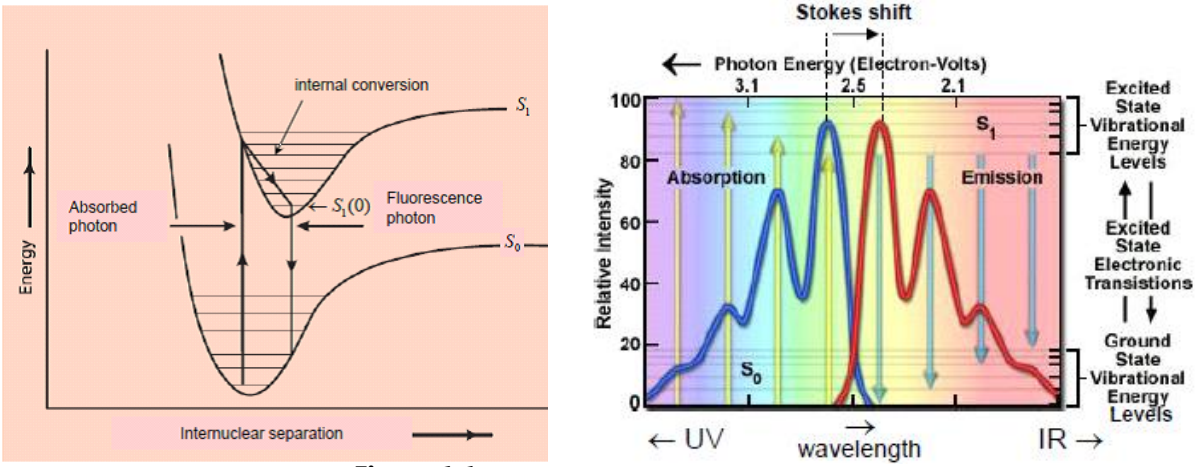

Figure 1.1 Fluorescence emission mechanism
(a) Excitation and relaxation of a fluorophore (b) Fluorophore absorption and emission spectra

The spectrum of fluorescence emission wavelengths depends on the energy gap between final and initial states the electron experiences in the transition. As a rule, the emission wavelength is always longer than the excitation wavelength, since some of the absorbed energy is lost during vibrational relaxation. This fact causes a relative shift, named Stokes shift, between absorption and emission spectra of a molecule, whose size can range from few to several hundreds of nanometers. The two are however similar in shape because of the comparable structure in the vibrational energy levels spacing both in ground and excited states. The situation is described in Figure 1.1b.

The difference between excitation and emission wavelengths allows the construction of the fluorescent microscope, whose working principle is to irradiate the specimen with light belonging to the absorption spectrum and collect fluorescence light, separating the two by means of a combination of dichromatic mirror, also called beam splitter, and filters, that act as follows, with reference to the Figure 1.2b:

- the excitation filter selects a narrow band of excitation wavelengths from the illumination beam in entrance to the mirror;
- the beam splitter, positioned at 45° with respect to the optical axis, transmits only over a certain value wavelengths, while the remaining light is reflected. The fluorophore excitation wavelength used is under threshold, so it is reflected towards the objective, that focus it on the specimen;
- longer fluorescence emitted wavelength crosses the objective again, which behaves also as a condenser, the mirror and the following emission filter for a finer selection; finally it proceeds along the axis up to the ocular and the detector.

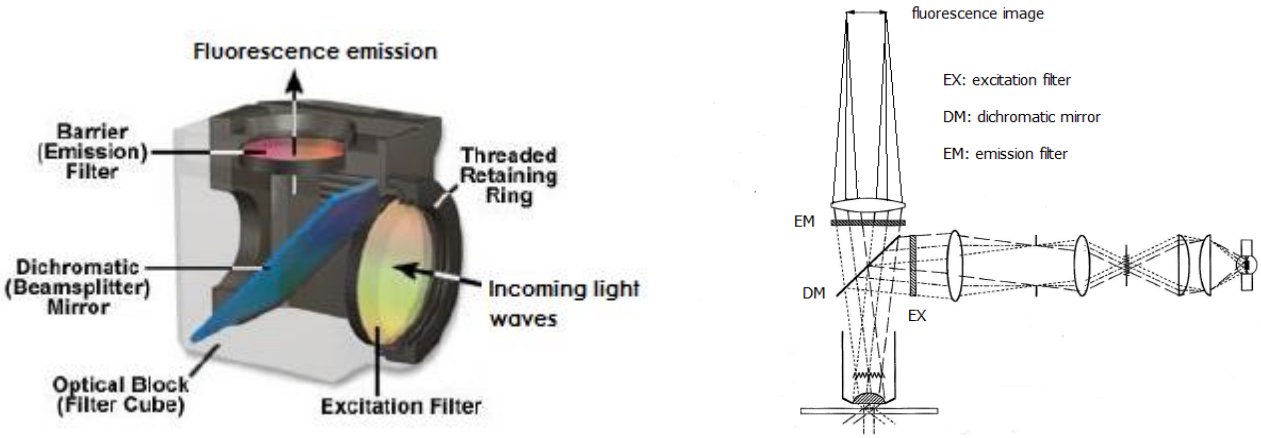

Figure 1.2 Fluorescence microscope

(a) Dichromatic mirror joined to filters (b) Scheme of fluorescence upright microscope

The presented mode of operation for the microscope is also known as "epifluorescence microscopy", where the configuration is compact because the function of objective and condenser is carried out by the same optical element, automatically ensuring the perfect alignment of objective and condenser.

The illumination condition in conventional fluorescence microscopy is in "widefield": a collection of plane waves, incident at different angles, illuminates a large volume of the sample, allowing the image formation of a wide portion of the focal plane, observed with a camera.

1.2 FROM WIDEFIELD TO CONFOCAL MICROSCOPY

1.2.1 Point Spread Function

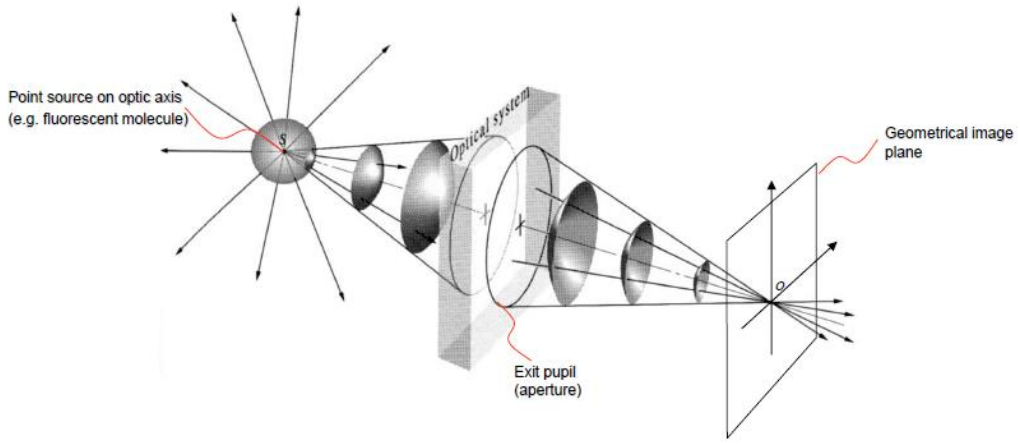

Figure 1.3 Ideal optical system

To form an image of a source of spherical waves, such as a fluorescent molecule, an optical system able to reverse diverging wavefronts into converging ones is needed (Figure 1.3). The ideal work of the optical system in geometrical optics is to establish a univocal relation between points in the object space and points in the image space. Because of the diffraction of the wavefront at the borders of the system circular exit pupil, this relation is not one-to-one, but the image of a geometrical point O in the object space always corresponds to a spot with a certain volume around the point expected to be the geometrical image point or focal point O' in the image space. The volume of the spot, defined by light distribution near focus, has a precise shape both in axial direction (along the optic axis) and radial direction (in the normal plane to the optical axis). The three-dimensional irradiance distribution near focus is called 3D Point Spread Function (3D-PSF). It can be calculated in an approximated way considering the model represented in Figure 1.4:

- a is the radius of the optical system exit pupil;
- W indicates the converging spherical wavefront of radius R at the exit of the optical system pupil;
- Q is a generic point belonging to it;
- P can be any point past the circular aperture, whose position relative to the focus is individuated by the vector V ;
- s is the distance between Q and P ;
- θ is the angle between QP direction and the optic axis;

- $\mu \cong \sin\mu = \frac{a}{R}$ is the angular aperture of the system.

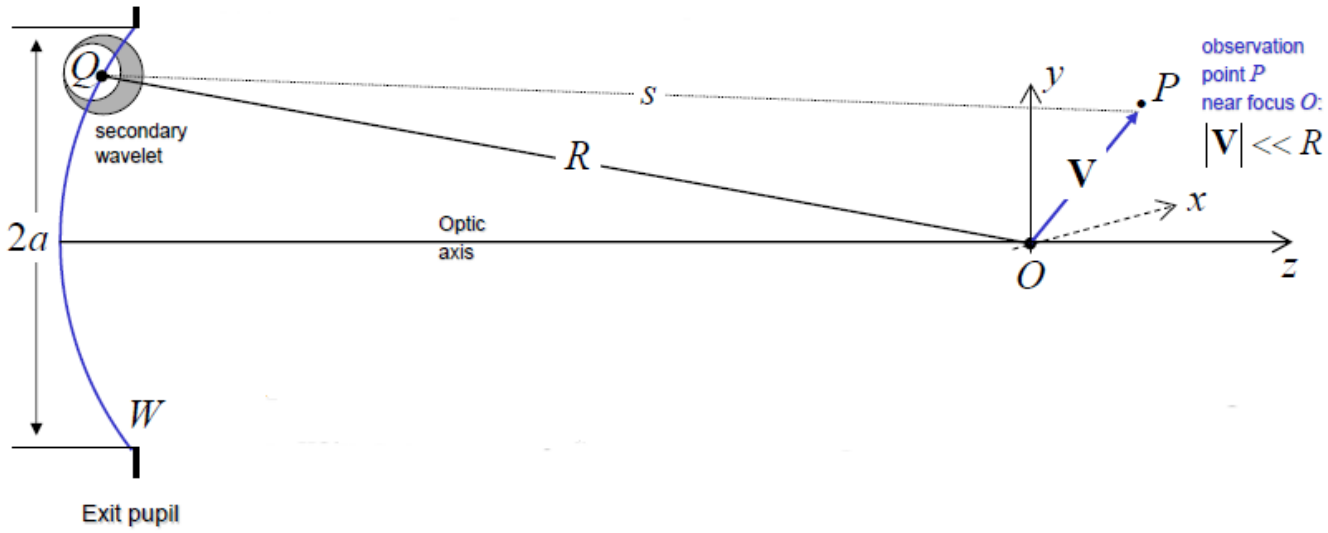

Figure 1.4 Scheme for PSF calculation

The Rayleigh-Sommerfeld diffraction integral (equation 1) expresses the diffracted field $U(P)$ knowing the incident field $U^i(Q)$ on the aperture, with λ and k respectively the incoming wave wavelength and wave number.

$$U(P) = \iint_W U^i(Q)\left[\frac{1}{j\lambda}\frac{\exp(jks)}{s}\right]\cos\theta \; d\Sigma \qquad (1)$$

This expression is nothing but the mathematical transcription of Huygens-Fresnel principle, according to which every point of an illuminated diffracting structure becomes a secondary source of spherical waves. This equation holds under validity of diffraction conditions, namely $\lambda \ll s$, and it is often expressed in dimensionless variables, known as optical coordinates (u, v), defined as follows:

$$\begin{cases} u = \frac{2\pi}{\lambda}\left(\frac{a}{R}\right)^2 z \quad \text{axial coordinate} \\ v = \frac{2\pi}{\lambda}\frac{a}{R} r \quad \text{radial coordinate} \end{cases} \qquad (2)$$

where $r = \sqrt{x^2 + y^2}$. After imposing the boundary condition $U^i(Q) = \frac{e^{-jkR}}{R}$, which describes the converging spherical wave at the exit of the optical system, thanks to a series of approximations and calculations the final expression for $U(P)$ is obtained; the 3D-PSF is

$$h(u, v) \equiv |U(u, v)|^2 \cong I_0 \left|2\int_0^1 J_0(v\rho)\exp\left(-\frac{1}{2}ju\rho^2\right)\rho \, d\rho\right|^2$$

with $0 \leq \rho \leq 1$ and $I_0 = \left(\frac{\pi a^2 |A_0|}{\lambda R^2}\right)^2$.

Its normalized form (divided by the irradiance at geometrical image point I_0) is often used. The irradiance distribution is drawn in Figure 1.5, where the lines locate the surfaces with constant value luminous intensity.

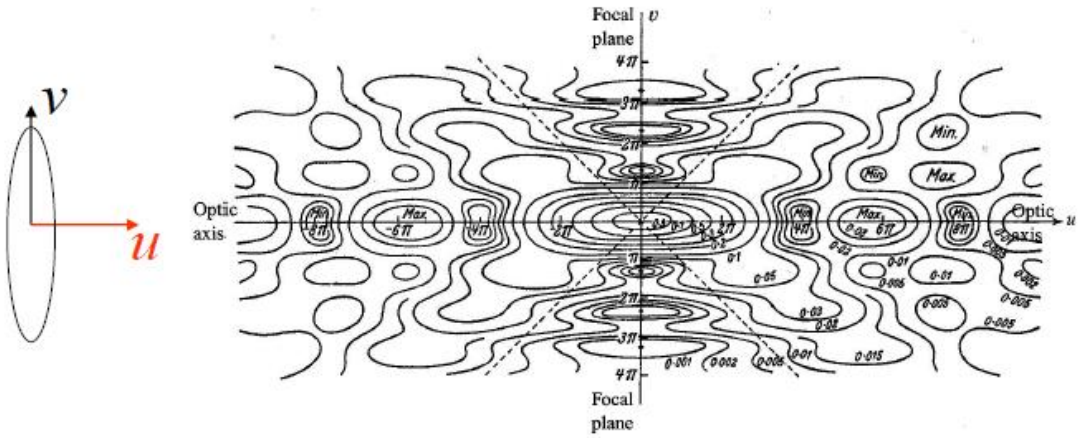

Figure 1.5 Point Spread Function contour lines

The obtained pattern near the focus represent the diffraction limit on focusing light by means of an optical system. In the context of fluorescence microscopy, the volume of light spot in the image space (see Figure 1.5) determines the extension of the excited region in the specimen, consequently it constitutes the inferior limit in imaging resolution.

According to Rayleigh criterion, two equally bright points are just resolvable in the image when the maximum of one intensity distribution coincides with the minimum of the other, as represented in Figure 1.6. We can then quantify the optical axial and radial resolutions as the distance between the two maxima, namely the coordinate value corresponding to PSF first zero in axial and radial directions respectively.

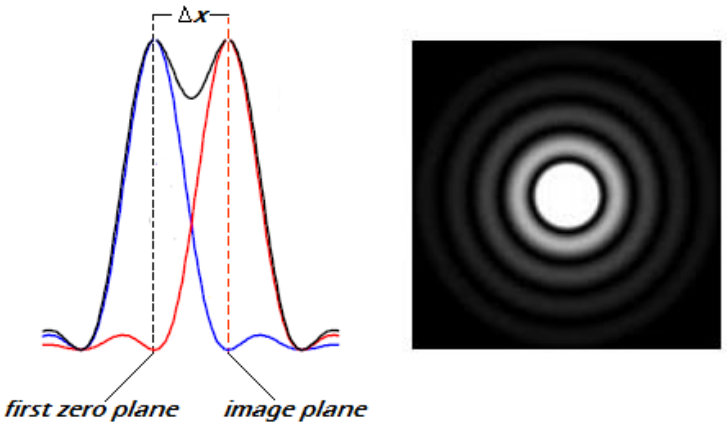

Figure 1.6 Rayleigh criterion for resolution determination
(a) Minimal condition for resolvable images (b) Airy diffraction image

Therefore, in order to calculate them, it is necessary to extract the intensity distribution along the optic axis $v = 0$ and in the focal plane $u = 0$:

$$h(u,0) = \left(\frac{\sin u/4}{u/4}\right)^2, \quad \text{first zero } |u| = 4\pi,$$
$$h(0,v) = \left(\frac{2J_1(v)}{v}\right)^2, \quad \text{first zero } |v| = 1.22\pi$$

$J_1(v)$ is the first order Bessel function; $h(0,v)$, the PSF in the image plane, is called Airy diffraction image. It is composed of a series of alternated bright and dark rings surrounding the central illuminated disk (Figure 1.6b). This last contains more than 80% of light and it is confined by the first dark ring, corresponding to the first minimum of $h(0,v)$, therefore lateral resolution coincides with its radius, the Airy radius.
Finally, axial and radial resolutions are expressed in cylindrical coordinates inverting equations (2),

$$\Delta z = \frac{2\lambda_0 n}{NA^2}$$

$$\Delta r = \frac{0.61\,\lambda_0}{NA}$$

where $NA = n \sin \mu$ is the numerical aperture of the system.

1.2.2 Confocal microscope

The main problem in widefield fluorescence microscopy derives from contributions of out of focus sample regions, which produce unwanted light that is collected by the objective. The consequence is a reduction of contrast due signals emitted by fluorescent sources placed in the focal plane, which can seriously compromise the ability to resolve the specimen details. The problem is known as "axial blurring".
The decisive idea was found by Lee Minsky in 1955 (4): to avoid axial blurring the object has to be illuminated and imaged point-by-point through the use of two pinholes, one placed at the exit of the source of a collimated light beam, the source pinhole, the other positioned just before the photodetector, called detection pinhole, as can be seen in Figure 1.7. The invention was not immediately available just because the microscope in this configuration can see only a point of specimen at a time, therefore it needs a system to scan the illumination spot over the entire focal plane to obtain an image of the object. The method started to be applied in biology later, during the 80's.

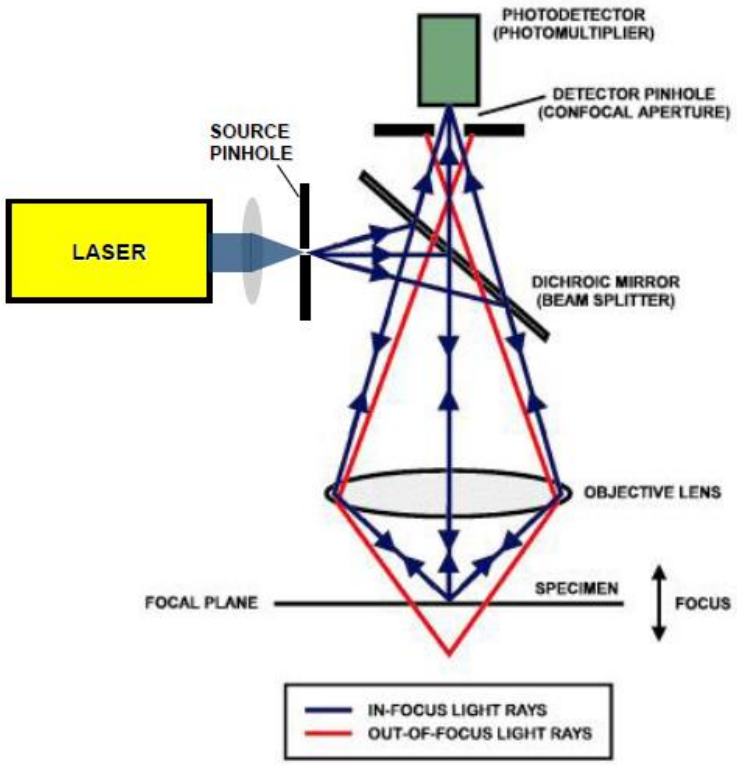

Figure 1.7 Scheme of a confocal microscope

In 1979 Brakenhoff and others (5) tested the goodness of the technique, experimentally proved its potentialities and expanded its application into cell biology. They also first used the word "confocal" to refer to this kind of microscopy, to underline the fact that both illumination and detection are confined to diffraction limited spots, which are optically conjugates. The results showed that confocal microscopy presents a high intrinsic capability of "axial optical

sectioning", removing almost completely the blurring effect; furthermore, resolution (measured as full-width at half maximum of imaged PSF) is improved by a factor $\sqrt{2}$ compared to traditional microscope (6).

The physical reason for better performances of confocal microscope lies in the approximately square dependence of the effective PSF on illumination intensity. The illumination point spread function $\mathrm{h}(\mathrm{u},\mathrm{v})$ is nothing but the probability density for a photon belonging to the laser beam to reach the point (u,v). In order to take part in image formation, this photon must excite a fluorescent molecule and the emitted photon must be detected. We expect a detection probability density similar to the illumination one, since light can travel the same optical path from one point to another and in the opposite way. The only difference between the two PSF is the wavelength, emission being longer than excitation, which enters in the definition of optical coordinates at denominator, as seen in equations (2); as a consequence, detection PSF coordinates are contracted by a factor $\beta = \frac{\lambda_{\mathrm{em}}}{\lambda_{\mathrm{ex}}}$, namely the irradiance distribution occupies a broader volume. The effective intensity distribution for confocal image formation is computed as the product of illumination and detection PSF because excitation of a point (u,v) and consequent detection of photon emitted in that point are statistically independent events. Considering typical values of the Stokes shift, 50-70 nm, it is possible to approximate λ_{em} with λ_{ex} and to affirm that confocal PSF is the square of illumination PSF. As a consequence, contributions from points out of focus, which have a small probability to be illuminated, thanks to the quadratic dependence, have an even smaller probability to take part to the image formation and so are effectively suppressed. The resulting PSF is shown in Figure 1.8 and compared with the PSF produced by a single lens.

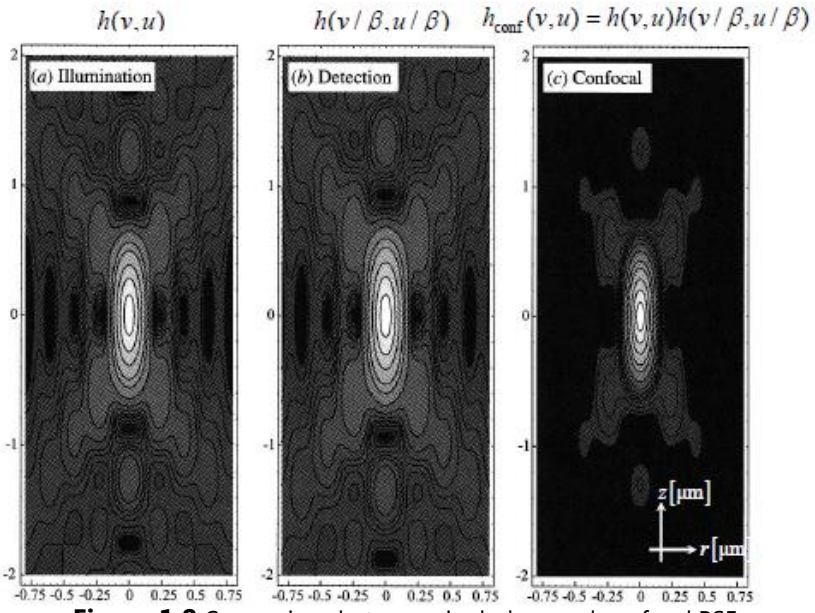

Figure 1.8 Comparison between single-lens and confocal PSF

The improvement of a factor $\sqrt{2}$ in confocal fluorescence microscope resolution applies to both lateral and axial extents of PSF intensity, both about 30 % narrower than those of conventional fluorescence microscope. In fact, axial and lateral resolutions are

$$\Delta z_{conf} \cong 0{,}7\Delta z = \frac{1{,}4\lambda_0 n}{NA^2}$$

$$\Delta r_{conf} \cong 0.7\Delta r = \frac{0.4\,\lambda_0}{NA}$$

In conclusion, in the history of microscopy the confocal technique turned out to be a fundamental tool for investigating biological specimens, in particular for the possibility to obtain the z-stack, a series of thin optical sections produced by modifying finely in incremental steps the position of focus along the optical axis. Converting these images through a digital image processor, it is possible to build a tomographic three-dimensional reconstruction of the object.

The main problem with conventional confocal point-scanning imaging is that regions above and under the focal plane in specimens are subjected to intense cones of excitation light. In fact, they can produce both an unwanted effect of fluorophores bleaching (photon-induced damage) in large areas and a considerable loss in signal: absorption of photons by intervening material prevents them to reach the focus, moreover scattering of fluorescence emission light keeps out the majority of photons from the objective angular acceptance (7). This phenomena lead to an inefficient signal generation, until deep in specimen confocal microscopy becomes completely unacceptably; an increased excitation light intensity would cause an even more serious damage, therefore the technique is not recommended for biological tissues, while it is best applied to thin specimens like cultured preparations or superficial cell layers in the tissue ($< 20\ \mu m$) (8). The problem of loss of signal in scattering samples and the impossibility to image deeper in thick objects have been overcome later, with the advent of multi-photon microscopy.

1.3 MULTIPHOTON MICROSCOPY

Multiphoton microscopy (MPM) is a form of laser-scanning microscopy based on nonlinear excitation of fluorescence, strongly localized within the raster-scanned plane. The process is defined "nonlinear" because the absorption rate depends on a higher than first power of illumination intensity. MPM allows to contain the problem of signal-loss due to light scattering in regions above the focal plane and constitutes the best noninvasive means to image deep in

explanted tissues or in living animals (9; 10). It has provided unprecedented possibilities to study angiogenesis, metastasis, lymphocyte traffics, embryos development, thanks to its capability to perform high-resolution imaging, fundamental to analyze physiology, morphology and cell-cell interactions deep in tissues or live animals (10).

1.3.1 Two-photon and multi-photon excitation

The primary signal source in MPM is fluorescence induced by two-photon excitation. The technique is based on absorption of two photons by a fluorophore in a single quantum event. The possibility for a molecule to absorb simultaneously two photons was predicted by Maria Goeppert-Mayer in 1931 (11), but experimentally verified only after the invention of lasers in 1961 (12).

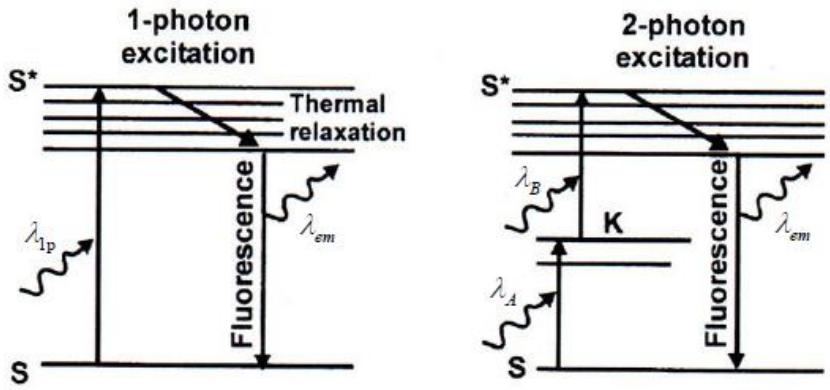

Figure 1.9 Schemes for 1P and 2P excitation processes

The principle of two-photon excitation (2PE) process is represented in Figure 1.9. and compared to single photon absorption (1PA). The energy required by the electron to perform the molecular electronic transition is the same in both cases, but in two-photon excitation it is provided in nearly equal parts by the combination of the energies of two different photons, through the passage in an intermediate virtual state. As the photon energy is inversely proportional to the wavelenght, the two photons must have wavelengths $\lambda_A \approx \lambda_B \approx 2\lambda_{1P}$, double with respect to the one used for 1PA. The occurrence of the event is determined by both photons interaction with the fluorophore, therefore they must incide upon the molecule with relative delay less than $\sim 10^{-16}$ s, the intermediate virtual state life time (10). Two-photon excitation rate depends on the second power of light intensity (8), but it is very small, about 10^{-14} times smaller than 1P absorption rate. This is the reason why high photon fluxes are needed (10^{30} photons/s cm^2), in fact the relatively wide spread use of multiphoton microscopy

in biomedical fields had to wait for the development of mode-locked lasers, with pulse durations below 1 ps and frequencies about 100 MHz (7).

Although 2PE requires elevated light intensities, it is convenient because it presents several advantages compared to single-photon excitation. First of all, the wavelengths used in 2P microscopy, deep red and near IR, are less subjected to scattering and absorption from tissue above the focal plane; this determines a deeper penetration inside specimens. Moreover, the technique allows great localization of excitation light, in volumes that can be small as $\sim 0.1\ \mu m^3$ (10): the effective two photons PSF contains a quadratic dependence on illumination intensity, because the absorption of two different photons are statistically independent events, so the total probability density is the product of two excitation probability densities $h(u/2, v/2)$, each one at wavelenght $\lambda_{2P} \approx 2\lambda_{1P}$. The resulting illumination PSF is

$$h_{2P}(u, v) = [h(u/2, v/2)]^2.$$

It leads to imaging resolutions slightly worse than confocal microscopy (with about a factor 1.3 for lateral and 1.5 for axial resolution (13)), as expected in theory, since they are linearly dependent on light wavelength, which is approximately doubled in 2PE.

On the contrary, thanks to localization of excitation, both ballistic (not scattered) and scattered fluorescence photons that are detected by the objective contribute to the signal, while in widefield or single-photon excitation the majority of scattered emitted photons is lost (excluded by the detection pinhole), or worse, part of background (8). This fact determinates the 2PE intrinsic ability to perform axial sectioning of samples, without the presence of pinholes and also the increased confinement of bleached fluorophore volume, which is restricted to the focal plane (13).

Multi-photon excitation is based on the same principles at longer wavelengths. It presents the same advantages of 2PE, but simultaneous events become rarer (the probability of absorption of *n* photons is proportional to the *n*-th power of illumination intensity), it requires higher instantaneous photon densities at the diffraction-limited focal volume of the objective in the specimen. Such concentrations of photons can be achieved only thanks to shorter laser pulses, to provide extremely high instantaneous intensities delivered to the sample, while the received average power remains not excessive.

In biologic microscopy the advantages offered by multi-photon excitation technique, in particular deeper penetration inside samples, are fundamental because they extend the analysis in the range of about 1 mm from the surface of the sample.

1.3.2 Higher harmonic generation

The phenomena of harmonic generation are widely exploited in biological microscopy. They are optical nonlinear processes, due to higher order terms in the expression of material system polarization $\mathrm{P}(\mathrm{t})$ in presence of external electrical field $\mathrm{E}(\mathrm{t})$ (here for simplicity assumed as scalar quantities). In fact, in nonlinear optics the optical response is described as a power series in the external field

$$\mathrm{P}(\mathrm{t}) = \epsilon_0\left[\chi^{(1)}\mathrm{E}(\mathrm{t}) + \chi^{(2)}\mathrm{E}^2(\mathrm{t}) + \chi^{(3)}\mathrm{E}^3(\mathrm{t}) + \ldots\right] = \quad (3)$$
$$= \mathrm{P}^{(1)}(\mathrm{t}) + \mathrm{P}^{(2)}(\mathrm{t}) + \mathrm{P}^{(3)}(\mathrm{t}) + \cdots$$

where $\epsilon_0$is the vacuum permittivity, $\chi^{(1)}$ the linear susceptibility, $\chi^{(2)}$and $\chi^{(3)}$ the second- and third-order nonlinear susceptibilities, which, if not vanishing, give raise to higher order nonlinear polarizations and consequently to higher order nonlinear processes, such as second harmonic generation (SHG) and third harmonic generation (THG) respectively. The emission frequency in these processes is a higher harmonic of the incident frequency ω ($2\omega, 3\omega$…), namely the emitted wavelengths are$^1/_2$, $^1/_3$… of the incident wavelength. Note that $\mathrm{P}(\mathrm{t})$ in equation (3) is assumed depend on the instantaneous value of the electric field strength; this is true only for lossless and dispersionless media, as implied by the Kramers-Kronig relations (see Appendix B). In the general case for dispersive medium, susceptibilities becomes complex quantities that relate complex amplitudes of electric field and polarization.

Phenomena of harmonic generation are examples of parametric processes (a process is "parametric" when the initial and final states of the system are identical). The population in the system is removed from the ground state only for a brief interval of time, according to the indetermination principle, for about $\hbar/\delta\mathrm{E}$, where $\delta\mathrm{E}$ is the energy gap between the virtual level and the nearest real level. This kind of process always conserves energy and it can be described through a real susceptibility. On the contrary, a process that involves only real levels is called "nonparametric" and it is described by means of complex susceptibility, namely there is dissipation, so photon energy doesn't need to be conserved because an energy exchange with material medium can happen.

Similarly to 2PE, nonlinear dependency on incident light intensity allows a greater localization of excitation and consequently an ability of optical axial sectioning of specimens. Since harmonic generation is exploited as a contrast mechanism, no fluorescence is needed; the main consequence is the elimination of photodamage and phototoxic effects, together with the possibility to avoid the use of fluorophores, which are instead commonly used in MPM (14). Harmonic generation is a particularly important source of signal in intravital microscopy because it reports the distribution of collagen, which delineates the boundaries between

different tissues and cells within the extracellular matrix. Furthermore, harmonic signals are easily identified because they are distinct from other potentially confounding sources.

In the present work we will limit to a qualitative description of main optical nonlinear processes actually observed in laboratory, referring to Boyd (15) for further details.

Second Harmonic generation (SHG)

The discovery of SHG in 1961 marked the beginning of nonlinear optics study (16). The technique finds important application in the field of nonlinear microscopy, often coupled with confocal imaging and excitation through femtosecond laser pulses. This configuration was first used by Curley (17).

Given a laser beam with harmonic electric field strength $\mathrm{E}(\mathrm{t})$ and frequency ω

$$\mathrm{E}(\mathrm{t}) = \mathrm{E}_0 \mathrm{e}^{-\mathrm{i}\omega\mathrm{t}} + \mathrm{E}_0^* \mathrm{e}^{\mathrm{i}\omega\mathrm{t}},$$

in the illuminated material system with nonzero second-order susceptibility, a second-order polarization is created

$$\mathrm{P}^{(2)}(\mathrm{t}) = \epsilon_0 \chi^{(2)} \mathrm{E}^2(\mathrm{t}) = 2\epsilon_0 \chi^{(2)} \mathrm{E}_0 \mathrm{E}_0^* + \left(\mathrm{E}_0^2 \mathrm{e}^{-\mathrm{i}2\omega\mathrm{t}} + (\mathrm{E}_0^*)^2 \mathrm{e}^{\mathrm{i}2\omega\mathrm{t}}\right)$$

The first term is at zero frequency, instead the second is at frequency 2ω; while the former does not lead to any radiation generation because its second time derivative vanishes (optical rectification), the latter is responsible for the emission of signal at the second harmonic frequency.

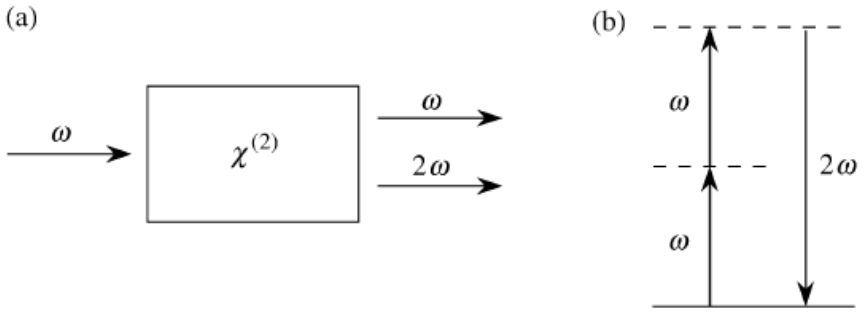

Figure 1.10 Second Harmonic Generation
(a) Scheme of the process (b) Energy-level diagram

The process can be interpreted as an exchange of photons between different frequency components of the electric field: in a single quantum event two photons of frequency ω are destroyed and simultaneously one photon of frequency 2ω is created, as can be seen in Figure

1.10b. The dashed lines represent virtual energy levels, not eigenstates of free illuminated atom or molecule, but a level resulting from the interaction between it and incident radiation photons.

SHG does not occur in media that present inversion symmetry, called "centrosymmetric". The fact is easy to demonstrate in the case of instantaneous response to the applied harmonic electric field $\mathrm{E}(\mathrm{t})$. Because of inversion symmetry, if the field sign is changed, also the polarization sign will result inverted; in particular, for second-order contribution we would have

$$-\mathrm{P}^{(2)}(\mathrm{t}) = \epsilon_0\chi^{(2)}\big(-\mathrm{E}(\mathrm{t})\big)^2 = \epsilon_0\chi^{(2)}\mathrm{E}^2(\mathrm{t}) = \mathrm{P}^{(2)}(\mathrm{t}) \equiv 0,$$

therefore the only possible solution is

$$\chi^{(2)} = 0.$$

Third Harmonic generation (THG)

Third-order contributions to medium polarization produces a radiative phenomenon at the third harmonic frequency. The THG signal is weaker than the SHG signal by orders of magnitude (14), but it is well observed, especially in centrosymmetric materials, such as several crystals. Given a laser beam with electric field strength $\mathrm{E}(\mathrm{t})$ and frequency ω

$$\mathrm{E}(\mathrm{t}) = \mathrm{E}_0 \cos \omega \mathrm{t},$$

using the identity (10)

$$(\cos \omega \mathrm{t})^3 = \frac{1}{4}\cos 3\omega \mathrm{t} + \frac{3}{4}\cos \omega \mathrm{t}$$

third order polarization results

$$\mathrm{P}^{(3)}(\mathrm{t}) = \epsilon_0\chi^{(3)}\mathrm{E}^3(\mathrm{t}) = \frac{1}{4}\epsilon_0\chi^{(3)}\mathrm{E}_0^3 \cos 3\omega \mathrm{t} + \frac{3}{4}\epsilon_0\chi^{(3)}\mathrm{E}_0^3 \cos \omega \mathrm{t}.$$

The first term leads to a process of radiative emission at third harmonic, which is microscopically described as destruction of three photons of frequency ω and following construction of one photon of frequency 3ω (Figure 1.11b).

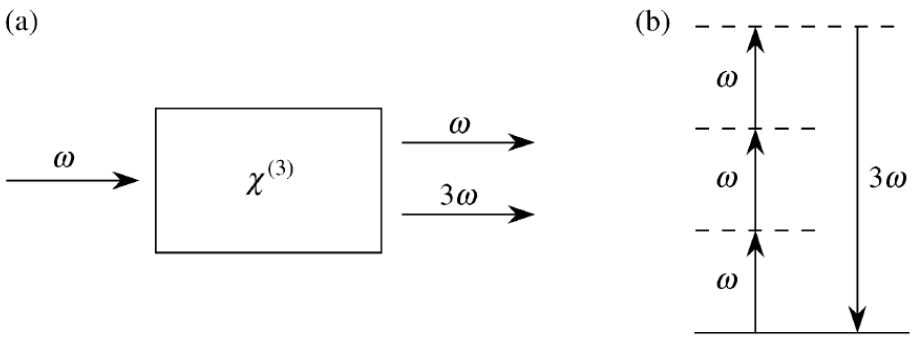

Figure 1.11 Third Harmonic Generation
(a) Scheme of the process (b) Energy-level diagram

Also third harmonic generation can be used in biological microscopy, as Muller (18) demonstrated, especially for imaging of transparent objects.

Sum-frequency generation

When a total optical field incident upon a second-order nonlinear medium is composed of two different frequency components ω_1 and ω_2 (like in the case of two different excitation beams), in addition to SHG related to each of them, other nonlinear optical effects can occur. In fact, if we visualize the electrical field as

$$\mathrm{E(t)} = \mathrm{E_1(t)} + \mathrm{E_2(t)} = \mathrm{E_1 e^{-i\omega_1 t}} + \mathrm{E_1^* e^{i\omega_1 t}} + \mathrm{E_2 e^{-i\omega_2 t}} + \mathrm{E_2^* e^{i\omega_2 t}},$$

second-order contribution to nonlinear polarization results

$$\mathrm{P^{(2)}(t)} = \epsilon_0 \chi^{(2)} \left[\mathrm{E_1^2(t)} + \mathrm{E_2^2(t)} + 2\left(\mathrm{E_1 E_2 e^{-i(\omega_1+\omega_2)t}} + \mathrm{E_1 E_2^* e^{-i(\omega_1-\omega_2)t}} + \mathrm{c.c.}\right)\right]$$

c. c. standing for complex conjugate. The first two terms leads exactly to SHG for both incident frequency components plus a static term, while second and third correspond respectively to the process of sum-frequency generation (SFG)

$$\mathrm{P}(\omega_1 + \omega_2) = 2\epsilon_0 \chi^{(2)} \mathrm{E_1 E_2 e^{-i(\omega_1+\omega_2)t}}$$

and difference-frequency generation (DFG)

$$\mathrm{P}(\omega_1 - \omega_2) = 2\epsilon_0 \chi^{(2)} \mathrm{E_1 E_2^* e^{-i(\omega_1-\omega_2)t}}.$$

These phenomena appear like radiative emissions at frequencies equal to the sum or the difference between the incident frequencies.

A sum-frequency generation effect is exploited in optical microscopy because in experiments with two laser beams, where it provides a third virtual channel of excitation useful to image

further details of the specimen. In other words, it allows to perform simultaneous three-color imaging of samples.

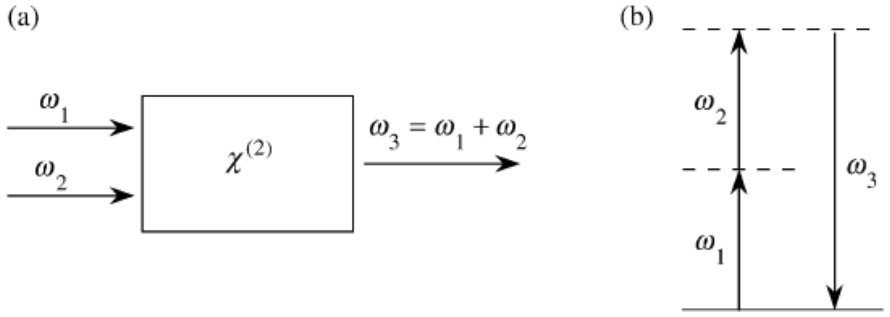

Figure 1.12 Sum-frequency generation
(a) Scheme of the process (b) Energy-level diagram

1.3.3 Two-beam multicolor fluorescence imaging

When a sample is illuminated by two laser beams with wavelengths λ_1 and λ_2, it can experience two-photon excitation of two different chromophores; in addition to these nonlinear independent processes, another chromophore can be excited by the simultaneous absorption of two photons, each belonging to one of the beams. The phenomenon, called two-color two-photon mechanism (2C2P), takes place when the pulses are temporally synchronized and present a submicrometer overlay of focuses (19). This combination provides an additional "virtual" excitation wavelength, which permits to perform simultaneous three-color imaging of the same specimen, provided suitable fluorophores are present.

In 1996 Gryczynski et al. (20) observed fluorescence emission from a fluorophore using two different wavelengths λ_1 = 380 nm and λ_2 = 760 nm. These wavelengths were obtained from the frequency-doubled and fundamental outputs of a dye laser, which was synchronously pumped with a mode-locked argon-ion laser, and cavity dumped at 1 MHz. The pulse width was near 7 ps. If the sample was illuminated with both beams, the emission intensity showed a square dependence on the total illumination power, when both sources were simultaneously attenuated to the same extent, indicating two-photon excitation. Instead, when the intensity at one wavelength was attenuated, the signal depended linearly on the power at each wavelength, indicating the participation of one-photon at each wavelength to the excitation process. Observation of the 2C2P signal required temporal and spatial overlap of the 380- and the 760-nm pulses. The emission spectrum generated by 2C2P overlapped with the emission spectrum observed for one-photon excitation with an equivalent energy of 250 nm (20).

To explain these experimental observations, let us consider the energies of photons belonging to the two beams, namely $\epsilon_1 = \frac{hc}{\lambda_1}$ and $\epsilon_2 = \frac{hc}{\lambda_2}$. In order to realize three-color imaging, their sum has to be equal to the energy required for *one-photon* absorption:

$$\epsilon_1 = \frac{hc}{\lambda_1} + \frac{hc}{\lambda_2}$$

Hence

$$\lambda_{3(1p)} \cong 250 \text{ nm}$$

whereas, for two-photon absorption,

$$\lambda_s = 2\lambda_{3(1p)} = \frac{2}{\left(\frac{1}{\lambda_1} + \frac{1}{\lambda_2}\right)} \cong 500 \text{ nm}$$

As shown by Mahou et al. (19), the three emission intensities, assuming Gaussian temporal profiles of the pulses and no overlap between excitation spectra, scale as

$$I_{\lambda_1} \sim (P_1)^2, \qquad I_{\lambda_2} \sim (P_2)^2, \qquad I_{\lambda_3} \sim 2P_1P_2 \exp\left(-\frac{\tau^2}{2\sigma^2}\right),$$

where P_1 and P_2 are the two average beam powers, τ is the temporal delay and σ the half $1/e^2$ width of the temporal intensity intercorrelation function between the two pulses. Assuming Gaussian profiles for both incident pulses, temporal intensity intercorrelation function can be treated as temporal intensity autocorrelation function, whose $1/e^2$ width measures about $\sqrt{2}$-fold the pulse temporal width.

The described method is more convenient than other multicolor imaging techniques, such as single-beam excitation of multiple chromophores or sequential excitation at different wavelengths. For quantitative multicolor imaging it is crucial to have independent control of different chromophores signals; actually the main advantage in 2C2P microscopy is the possibility to adjust simultaneously and independently the intensities of the three emissions, together with a reduction of acquisition time. For these reasons, multicolor two-photon imaging is likely to find several applications in experimental biology (19).

1.4 STED MICROSCOPY

Although imaging performances in confocal and multiphoton imaging are largely improved compared to widefield microscopy, the resolution limit is still dictated by diffraction. Two atomic emitters can not be distinguished if they both fall within the extent of the (effective) point spread function (PSF) of the microscope, which is never limited to a geometrical point. The method proposed in 1994 by Hell and Wichmann (21) to break the diffraction limit is known as stimulated-emission-depletion (STED) microscopy. The method has earned by Stefan W. Hell the 2014 Nobel Prize in Chemistry "for the development of super-resolved fluorescence microscopy"[1].

Stimulated emission is a radiative molecular transition mechanism first described by Einstein in 1917 (22). When a photon carrying an energy (approximately) equal to the gap between a higher $S_1(0)$ state and a lower vibrational state S_0^{vib} interacts with the molecule in the excited state $S_1(0)$, it promotes the transition from $S_1(0)$ to S_0^{vib} and generates another photon indistinguishable from itself. The principle on which is based STED microscopy is to tightly intertwine in time and space an illumination beam, responsible for spontaneous fluorescence excitation in the proximity of the geometrical focus, and a STED beam, responsible for molecular de-excitation outside the focal point. To this end, the STED beam focused on the sample by the microscope objective features a zero intensity point in the geometrical focus. By a suitable combination of excitation and depletion, it is possible to lower the resolution limit to few tens of nanometers, well below the value of the emission wavelength, tipically in the order of hundreds of nanometers.
The best STED microscopy results have been obtained with pulsed lasers by satisfying simultaneously three critical conditions:

1) Spectral conditions: the STED beam wavelength must be selected within the fluorophore emission spectrum, with minimal overlap with the absorption spectrum, in order to maximize stimulated emission and to avoid re-excitation by the STED beam; as a consequence, the STED wavelength is red-shifted compared with the best single-photon excitation wavelength.
2) Temporal conditions: these are rather strict, because several factors must be considered for each type of laser pulses; first of all, the excitation pulse width τ_{exc} must be shorter than the average vibrational relaxation time $\tau_{vib} \leq 1$ ps. This situation prevents the vanishing of excited molecules population caused by quenching even during excitation; typical pulse duration are $\sim$ 200 fs. Furthermore, in order to block spontaneous fluorescence emission in the regions around geometrical focus, the STED pulse must follow the excitation pulse with a delay significantly shorter than $\tau_f \sim 1$ ns, the characteristic spontaneous fluorescence lifetime. Another potential problem arises in

[1] http://www.nobelprize.org/nobel_prizers/chemistry/laureates/2014/hell-facts.html

fluorophore re-excitation by the STED pulse, in the presence of a large population in higher vibrational state S_0^{vib}; the solution consists in keeping the STED rate lower than vibrational decay rate, namely the STED pulse width τ_{sted} has to be considerably larger than τ_{vib}, so that re-excitation is prevented simply by vibrational quenching within S_0. Typical STED pulse widths are in the range of several picoseconds.

3) Spatial conditions impose that the two beams are co-axial. Upon traversing the microscope objective, excitation generates an ordinary three dimensional PSF around the geometrical focus. Instead, the STED beam is phase-modulated prior to entering the objective. A common procedure consists in producing a Gauss-Laguerre beam (characterized by a spiral shape of the wavefront), by means of a vortex phase-plate positioned in the beam path. Once focalized by the objective, the phase-encoded STED beam produces a destructive interference at its geometrical center, resulting in a radially symmetric three dimensional PSF h_{STED} with a central zero. In the focal plane h_{STED} is shaped like a doughnut centered on the geometrical focus. In the focal plane, the two irradiance functions can be approximated as

$$\begin{cases} h(r) \cong \cos^2(ar) \\ h_{sted}(r) \cong \sin^2(ar) \end{cases}$$

where $r = \sqrt{x^2 + y^2}$ is the radial coordinate in the focal plane and $a = \frac{\pi}{2\delta r_{min}} = \frac{\pi n \sin \mu}{\lambda_0}$ (Figure 1.13).

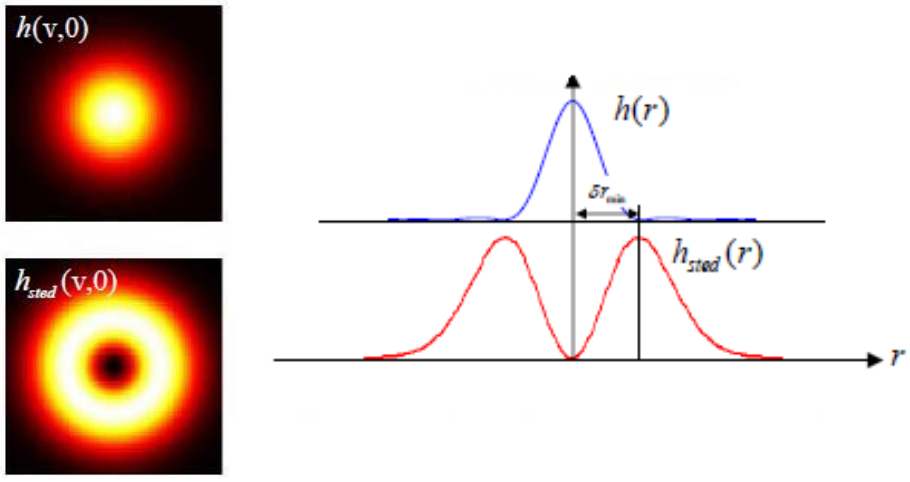

Figure 1.13 Focal distribution of light in STED microscopy
(a) focal spots of excitation (top) and STED (bottom) beams (b) irradiance profiles vs. radial distance from the focal point

δr_{min} is the value of the first minimum of $h(r)$, namely the diffraction limited resolution. After the incidence of the STED pulse, the effective excitation PSF is a product between excitation PSF h and the population of molecules still in the excited state n_1^{sted}:

$$h_{eff}(v,u) = h(v,u)n_1^{sted}(v,u). \qquad (4)$$

n_1^{sted} represents the remaining spontaneous fluorescence probability. To evaluate the efficacy of depletion we can refer to the depletion ratio d; for a Gaussian STED pulse of duration τ_{sted}, it is defined as the ratio between the excited state population after a time $t = 4\tau_{sted}$ with and without exposure to the STED pulse

$$d = \frac{n_1^{sted}(t = 4\tau_{sted})}{n_1(t = 4\tau_{sted})}$$

For a given $\tau_{sted} \ll \tau$ (τ spontaneous fluorescence lifetime), we can assume $n_1(t = 4\tau_{sted}) \approx 1$, hence

$$d \cong n_1^{sted}(t = 4\tau_{sted}) \cong \exp\left(-\frac{I_{sted}}{I_{sat}}\right)$$

I_{sat} is known as STED saturation irradiance and it is defined as the irradiance at which the depletion ratio is reduced by a factor $1/e$. Typical values for I_{sat} are comprised between 1 and 100 MW/cm^2 in order of magnitude.
After the STED pulse is terminated, we can express the fluorescence probability of a molecule as

$$n_1^{sted}(v,u) \cong \exp[-h_{sted}(v,u)\, I_{max}/I_{sat}],$$

with I_{max} the peak irradiance of the STED pulse. I_{max} is fixed by the source and the microscope setup, usually $\sim 1\ GW/cm^2 \gg I_{sat}$, but always limited by the photodamage of specimen and the photobleaching of fluorophore. Substituting the approximated forms for excitation and STED point spread functions in the expression (4) and making use of the asymptotic series for sine, cosine and exponential up to the second order, we obtain

$$h_{eff}(r) \approx 1 - \left(1 + \frac{I_{max}}{I_{sat}}\right) a^2 r^2.$$

Since resolution can be defined through the FWHM of the effective irradiance, namely the double radial distance for which $h_{eff}(r) = 1/2$, we can invert (19) and solve for r,

$$r \approx \frac{1}{\sqrt{2}a\sqrt{1 + I_{max}/I_{sat}}}$$

In conclusion, using $a = \pi n \sin\mu/\lambda_0$, the new inferior limit for optical microscopy resolution is

$$\delta r_{sted} = 2r \approx \frac{\sqrt{2}}{\pi} \frac{\lambda_0}{n \sin \mu} \frac{1}{\sqrt{1+I_{max}/I_{sat}}}.$$

The crucial change with respect to diffraction limited resolution is the presence of the factor $\frac{1}{\sqrt{1+I_{max}/I_{sat}}}$: the higher the ratio I_{max}/I_{sat}, the smaller the inferior distance that can be distinguished with the microscope. This theoretically infinite resolution is obviously limited, in particular for increasing I_{max}, by practical constraints such as photodamage of samples and how deep is the central zero in STED irradiance distribution at focal plane.

The great possibility offered by STED microscopy finds fundamental applications in molecular biology, medicine and in physics of matter: for example in the field of neuroscience dendritic spines have been imaged with 60-nm resolution (23) or in solid state physics nitrogen vacancy centres in diamond have been observed at nanoscales, with measured point spread function FWHM of 6 nm (24). Because of these surprising results, where the resolving power exceeds the wavelength of light by two orders of magnitude, STED microscopy gained the epithet of "superresolution technique", furthermore referring to this method it would be actually more appropriated to speak about "nanoscopy".

1.5 INTRAVITAL MICROSCOPY OF THE TUMOR MICROENVIRONMENT

During the past decades scientists have tried to understand the mechanisms that underlie tumor growth, migration and metastasis. The goal still remains a challenge because of high variability of tumor cell behaviors, due to interdependence between the cancer development and the local microenvironment reactions. To construct a more complete comprehension of the dynamic biological processes in tumors, they have to be monitored over time at cellular scales and in their natural environment: the living animals. The emerging techniques and protocols of intravital microscopy (IVM) can give insights not only about tumor progression mechanisms, but also about optimization of candidate drugs and success or failure of therapies (25).

The importance of intravital microscopy resides in the fact that it can provide information about the real dynamics of biological processes, otherwise unpredictable by *in vitro* or *ex vivo* studies. In fact, the *in vivo* environment has such a profound effect on tumor progression that it gained the adjective "reactive"; as an example, it can determinate the mode of tumor cell migration. The first step to perform long-term high-resolution imaging in live models (mice) is to ensure the optical access to tissues that have to be observed. With exception of superficial tissues like skin (or cerebral cortex, which can be imaged even through the method of skull thinning), this aim requires a surgical procedure for the implantation of an optically transparent window. It consists in the surgical exposure, accomplished in sterilized and controlled environment of the

site, followed by the setting of a glass coverslip, fixed by glue. The procedure is invasive, but it provides direct access to large areas (from ~ 0.8 to $12\ \mathrm{mm}^2$) lasting for several weeks or months, even if duration depends on the quality of surgical operation (26). The optical windows become available to study tumors are the dorsal skin-fold chamber (subcutaneous tumors), the ear chamber, the cranial imaging window (brain tumors), the mammary imaging window (breast tumors), and the abdominal imaging window (tumors in the intestine, pancreas and liver) (25). Most tissue structures generate intrinsic signals when illuminated with appropriate wavelengths; this fact enables a multispectral analysis of tumor microenvironment through label-free imaging methods. As an example, the extracellular matrix can be mapped by second harmonic generation (SHG) signals, which highlight fibrillary collagens, while third harmonic generation (THG) is used to image water-lipid and water-protein interfaces, such as cellular membranes and tissue discontinuities, or interfaces along vessels and nerves. When intrinsic signals are not delivered, as in the case of vasculature, the study is carried out by means of injection of fluorescent tracers like quantum dots and fluorescently labelled dextran or red blood cells. The alternatives are to use genetically modified fluorescent reporter mice, in which fluorescent proteins are expressed in endothelial cells, or adopt the technique of immunolabelling. Tumor cell cytoplasm and nuclei are usually labelled by different fluorophores. The described overview shows how multi-parameter IVM can create a map of tumor cell functions and behaviors with regard to stromal structures, best realized by combining different contrast mechanisms (3; 25).

The risk of cancer-related death is represented by tumor metastasis. It is a dynamic, microenvironment-dependent process in which only a minority of tumor cells, the "invading cancer cells", separate from solid tumor, develop different morphologies and kinetics, migrate and invade other tissues. They can be single cells or cohesive multicellular units. In contrast to *in vitro* models where the substrate is uniform, *in vivo* observation accounts for the behavior of invading cells in relation to tissue geometry: to move collectively, they often exploit already existing tracks in the tissue, such as blood vessels (perivascular or intravascular migration), nerves, myofibres or 1D fibrillary strings of individual collagen fibers to spread until reaching the sessile state and beginning a new tumor growth. Intravital microscopy experiments show that extracellular matrix and its modifications during disease have a fundamental role in successful organ invasion: tumor colonization is just an adaptive and reciprocal process between invading cells and local microenvironment, with contribution of other circulating cells and factors (3). Among the enormous number of cells in the solid tumor, only a small minority takes part to metastasis formation; IVM can contribute to the identification those rare cells that present intrinsic motility properties, combined to the description of the microenvironment metastasis promotion. A fundamental component in cancer progression is the process of angiogenesis, the formation of new blood vessels which will supply nutrients for tumor growth. Nowadays the effects of anti-angiogenic treatments are not satisfying: IVM offers the capability of monitoring vasculature, variations of blood flow or vessel permeability during the progression or under therapy conditions, for example through the quantification of oxygen level

by imaging oxygen probes. Another expression of the paradoxical role of tumor microenvironment is the behavior of the immune system: immune cells infiltrated in the tumor stroma can either attach cancer or have a pro-tumor action. IVM of fluorescently labelled lymphocytes that infiltrate tumors can clarify the role of immune system, indicating the convenience of stimulating it to enhance cancer rejection or not, identifying the best therapy approach (25).

The deregulated growth of tumor mass essentially derives from an alteration of normal apoptosis process, namely the form of programmed cell death that is responsible for the maintenance of a constant number of cells in a system. One of the aim of anti-cancer therapy in general is to enhance apoptosis induction in tumor cells, a goal for which a profound knowledge of inter- and intra-cellular signaling is needed. Monitoring cell-cell communication and biological signal transduction by IVM is currently challenging: it has a crucial significance, considered for example the importance of calcium (Ca^{2+}) signaling in the regulation of cell death, in fact the dynamics of Ca^{2+} can change cell sensitivity to apoptosis (27). Although intracellular Ca^{2+} transport mechanisms have been successfully studied *in vitro*, at present scientists are trying to construct a complete comprehension of their physiological role in the tumor microenvironment. Intravital imaging techniques are joined to the use of photo-activatable fluorophores; this kind of fluorophores remain in a dark non-fluorescent state until they are activated by multiphoton excitation. The strategy allows to push even deeper multiphoton imaging depth limit in scattering samples because of the greater contrast created by the disparity of bright-dark states in space (28). This approach is exploited just to identify the stimulus able to induce an apoptotic Ca^{2+} signal within the tumor mass under cancer therapy conditions.

Intravital microscopy has become a fundamental tool in biomedical studies; it enabled an unprecedented exploration in living animals, but it still presents some important limitations: imaging depth up to 1 mm for fluorescent signals, acquisition speed, resolution, light aberrations, sensitivity to low fluorescent signals, access to organ with minimal invasion. To improve temporal resolution, confocal and two-photon microscopes can be equipped with resonant scanners that allow a scanning speed of 30 frames per second (29). Recent researches demonstrated the successful employment of spatial light modulators for parallel acquisition over multiple points of interest, without the need of mechanically moving parts; in such a way, the imaging system achieves frame rates up to 1 kHz (30). Light aberrations, *in vivo* mostly specimen-induced aberrations, affect both imaging resolution and maximum depth of penetration. They can be overcome thanks to adaptive optics, for example applying sensorless adaptive techniques to correct spherical aberrations and improve quality of multiphoton images (31). More sensitive detectors could permit detection of low signals, furthermore permanently implanted microlenses into living models could minimize the exposure of the organs and consequently the risk of altering their physiology. In the last few years the effort was directed

also through the development of strategies to minimize the motion of specimen caused by the heartbeat or the respiration of the animal. This attention made possible to image subcellular structures with temporal and spatial resolution comparable to those achieved *in vitro* models (32).

2 MATERIALS

This chapter describes a fluorescence laser scanning imaging system of the UNIPD Department of Physics and Astronomy, currently under construction in a laboratory of the Venetian Institute of Molecular Medicine of Padua. The following test provides insight into the position, function and potentialities of each optical element or device which compose the system.

The system is built around a two-photon excitation laser scanning microscope (Bergamo II System B232, Thorlabs Inc., Newton, New Jersey, USA) fed by two high power laser beams which travel along separate paths on the optical bench before being merged at the entrance of the microscope. Once completed and optimized, the system is designed to perform two-beam multicolor multiphoton microscopy as well as super-resolution STED nanoscopy.

Both techniques require the simultaneous use of two laser beams, which must be focused with sub-micrometric precision in the proximity of the geometrical focus. The beams are generated by a mode-locked Ti:Sapphire laser (Chameleon Ultra II, Coherent Inc., Santa Clara, California, USA), with tunable wavelength in the range 680-1080 nm, which provides 140 fs pulses at frequency of 80 MHz. This laser is used as a pump for an optical parametric oscillator (Chameleon Compact OPO, Coherent), which extracts a fixed percentage from the main beam power to produce a second beam, henceforward called "OPO beam", tunable in the interval 1000 - 1550 nm, with pulse duration of 200 fs. Pump and OPO pulses are intrinsically synchronized, but temporal alignment is lost the moment the two beams travel different paths.

The imaging setup is divided basically into three parts: laser sources, beam conditioning optics (laid down on the optical bench which supports both lasers and microscope) and the microscope itself. The beams are accessible and can be manipulated manually while travelling on the optical bench, but access is precluded after they are recombined at the entrance of the periscope which feeds the beams to the microscope body.

To perform multicolor multiphoton imaging, each beam provides excitation light at predefined wavelength. Instead, to perform STED nanoscopy the OPO beam is used for sample excitation, while the pump beam is used for depletion. The two working modalities require different spatial and temporal conditions to be satisfied:

Multicolor multiphoton microscopy

- Focusing of the pump and the OPO beam in the same spatial region of the sample, with sub-micrometric precision in the overlay;

- temporal synchronization of the two pulses with precision in the order of ten femtoseconds.

STED nanoscopy

- Focusing of the pump and the OPO beam in the same spatial region of the sample, with sub-micrometric precision in the overlay;
- delay of the pump pulse with respect to the OPO pulse less than one hundred picoseconds;
- temporal stretching of the pump pulse up to a duration of some picoseconds through a single mode optical fiber;
- modulation of the intensity distribution of the pump beam at focal plane, shaped as a doughnut through a spiral phase plate for the spontaneous fluorescence emission depletion.

For the beam conditioning optics it has been necessary to implement simultaneously two configurations, equipping the system with mechanical devices to quickly switch from one to the other. This is obtained by the introduction of four sledges in the pump beam pathway; they support some optical elements that have to be inserted in the case of STED nanoscopy and removed in the case of multicolor microscopy. In Figure 2.1 the multicolor configuration is presented (all the elements are present also in the STED configuration).

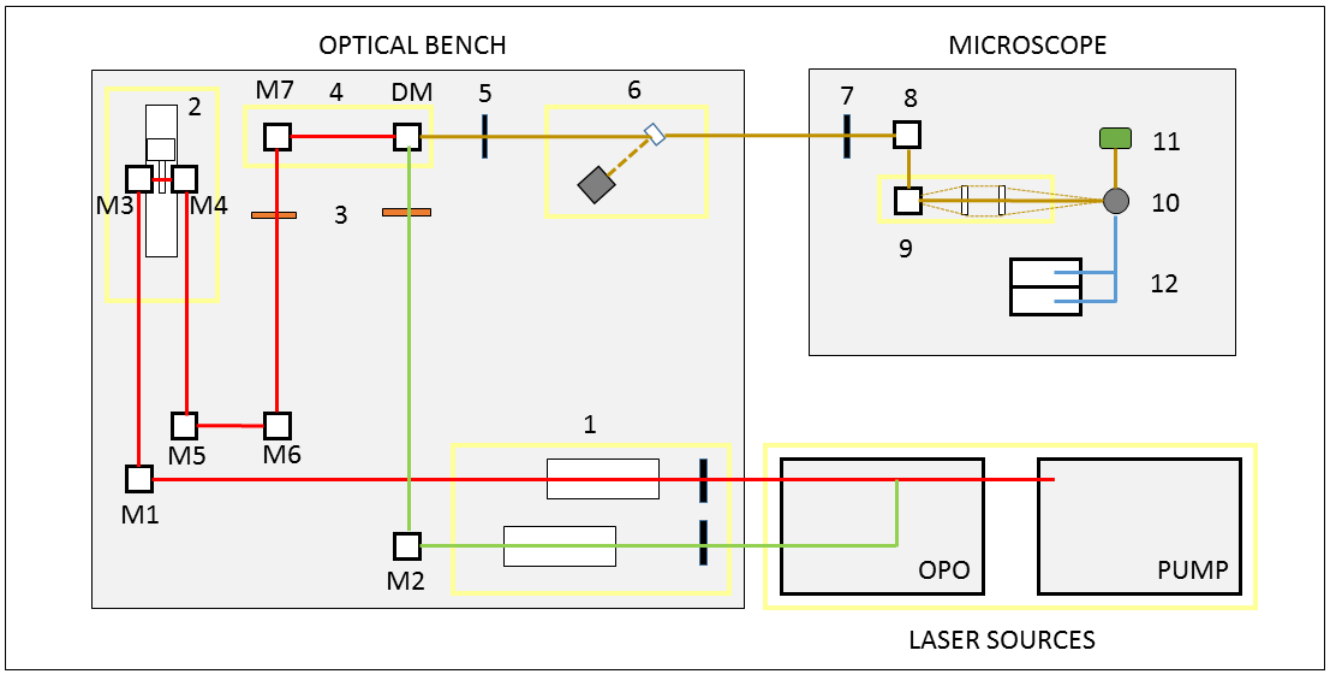

Figure 2.1 Multicolor microscopy setup configuration

Legend

OPTICAL BENCH

The mirrors are marked through the letter “M” and a growing number, with exception of the dichroic mirror, aimed at beams recombination, indicated with “DM”. The other elements are marked only by numbers.

1. Pockels cells: beams power modulation
2. Mobile delay line (DL1): temporal synchronization of the two pulses
3. Quarter-wave plates: circular polarization of light
4. Recombination mirrors (M7 and DM)
5. First pinhole (P1): first reference for the alignment
6. Photodetection system: supervision of the pulses at the oscilloscope
7. Second pinhole (P2): second reference for the alignment

MICROSCOPE

8. Periscope (two mirrors)
9. Scan head (two galvo/resonance mirrors)
10. Objective
11. Sample site
12. Photomultipliers (PMT)

In Figure 2.2 the STED configuration is shown: the four elements marked with the letters are mechanically removable from the pump laser path.

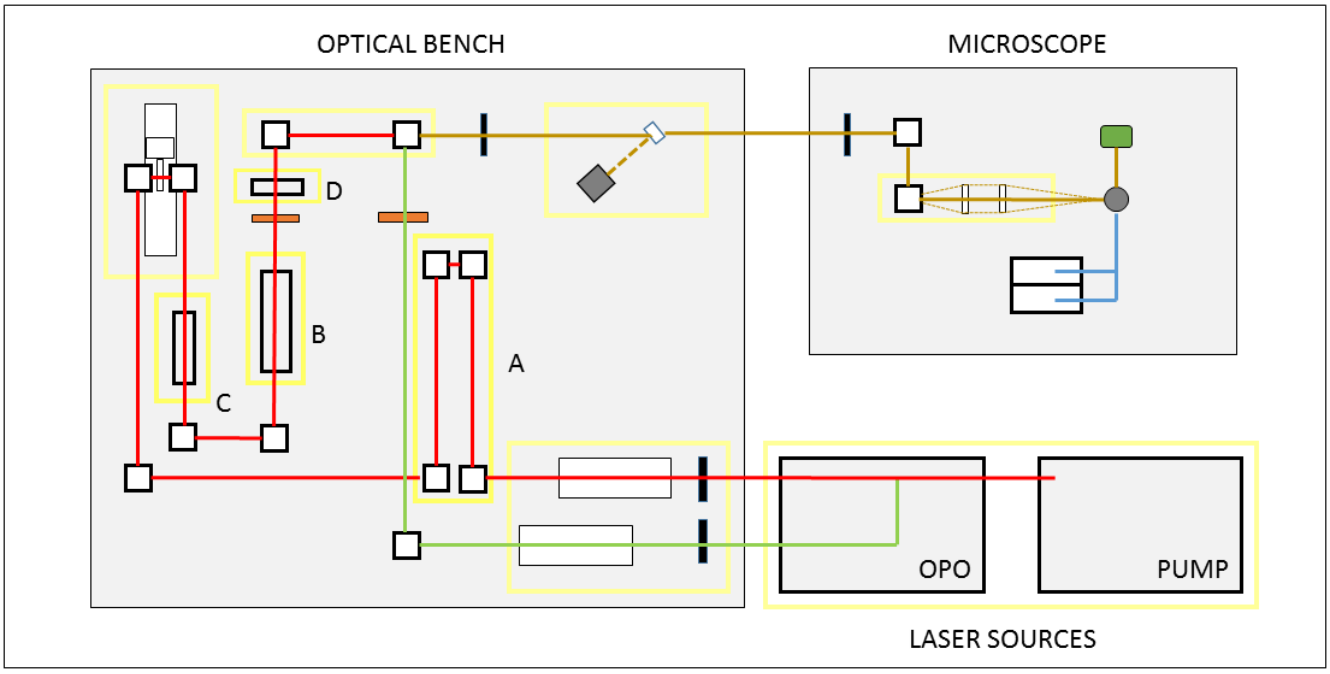

Figure 2.2 STED microscopy setup configuration

Legend

A. Fixed delay line (DL2): temporal synchronization of the two pulses
B. Optical fiber: temporal stretching of the pump pulse
C. Glass rod: protection for the single mode optical fiber
D. Spiral phase plate: modulation of the intensity distribution of the pump beam wavefront

2.1 LASER SOURCES

The pump laser source Chameleon Ultra II is able to furnish a beam power up to 4 W, dependent on the selected wavelength, with the maximum at 800 nm. As shown in Figure 2.3, the output beam is immediately guided into the entrance of the OPO. Inside this auxiliary source the pump beam is split in two: one part is directed unvaried to the first OPO exit, the other is effectively converted into higher wavelength light and sent to the second OPO exit; in such a way the two beams are constructed. They have an initial diameter about 1 mm, destined to become larger because of a small divergence of the collimated light, until about 4 mm the end of their paths.

The pump beam at the beginning of its path has a power between 360 mW and 610 mW, dependent on the selected wavelength, the OPO beam from 225 mW to 700 mW. Each exit of the laser sources is equipped with a shutter to block the beam without turning off the pump.

Figure 2.3 Laser sources: OPO on the left, pump on the right

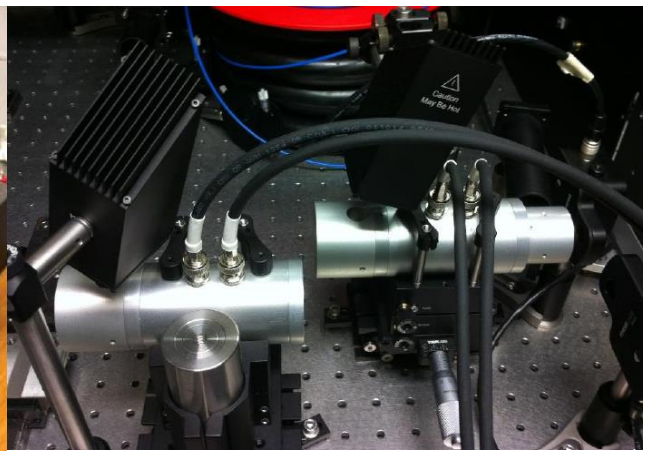

Figure 2.4 Pockels cells

2.2 BEAM CONDITIONING OPTICS

Pockels cells

The setup is equipped with a system for beams power modulation, in order to work with lower powers than those produced at the sources (especially during the optics alignment procedures). This system is composed of two Pockels cells placed in front of the laser sources exits (Figure 2.4). Each one is alimented by a power supply console.

The Pockels cell device exploits the linear electro-optic effect of a uniaxial crystal to modulate the intensity of the light passing through it (33). A crystal is defined optically uniaxial when there is only one direction through which the phase velocity is the same for both planes of polarization. In other words, there is only one direction, called optic axis and parallel to the crystallographic z-axis, with a different refractive index, the extraordinary index n_e. The other two orthogonal axes x and y are associated to the ordinary index n_o. A wave propagating along the optic axis sees the crystal as an isotropic mean, while a wave propagating orthogonally to the optic axis finds out the crystal anisotropy. The electro-optic effect is the change of the refractive indices caused by an external electric field. When the material refractive indices are voltage sensitive, the electric field can transform an isotropic material into an anisotropic one.

It is possible to express the ordinary refractive index as a function of the electric field E through a Taylor series (the equation is scalar for simplicity, but it should be in tensor form)

$$n(E) = n + a_1E + a_2E^2 + \dots$$

The contribution to index variation due to the linear term is known as Pockels effect, manifested only by noncentrosymmetric crystals (coefficient a_1 not null). Pockels effect can be described as a deformation of the index ellipsoid, corresponding to a variation of the indices values, which can be different for different directions. As a consequence, an isotropic material, whose index ellipsoid is a sphere, can become uniaxial or a uniaxial material can turn into a biaxial one (three different values for the principal refractive indices). Typical materials that exhibit linear electro-optic effect are uniaxial crystals like Potassium dihydrogen phosphate (KDP) or Ammonium dihydrogen phosphate (ADP). Since index variations correspond to light phase velocity changes, a uniaxial crystal presenting Pockels effect can be exploited as a dynamic phase retarder, in a device called Pockels cell. The instrument exists in the longitudinal or transverse configuration; in the former the external electric field is applied parallel to the optic axis, while in the latter it is applied in orthogonal direction.

In longitudinal Pockels effect the beam travels along the optic axis (z-axis). With no external electric field applied, the x and y refractive indices are equal, so the index ellipsoid projection on a plane perpendicular to the optic axis is a circle. In the ideal case the emergent ray is unchanged in amplitude and relative phase between the two polarization components along x and y directions, hence it will arise with the initial polarization form. This means that the crystal is not birefringent in the direction of the optic axis. However, in reality there are possible absorption or reflection amplitude losses and the available crystals are always slightly birefringent, but the effect in absence of external electric field is quite insignificant (34). When an electrical field is applied in parallel to the optic axis, the refractive indices in x and y directions change differently. As a consequence, the shape of the index ellipsoid changes: from a circle its projection becomes an ellipse with the induced axes x' and y' making a $45°$ angle with the x and y crystallographic axes, as shown in Figure 2.5. The lengths of the ellipse axes in the $x'$and y' directions are proportional to the reciprocals of refraction index associated to those directions. In such a way the crystal appears to be birefringent in the direction of the optic axis: the vibrations of light electric field do not have the same velocity along x' and y' directions anymore and a phase difference or retardation between these two polarization components now exists. Light rays propagating along the optic axis, polarized in the direction of induced axes x' and y', will have velocities which are functions of the electric field modified refractive indices. The consequence of these modified indices can be observed also propagating along the optic axis a linearly polarized beam in x or y direction; the output beam can be resolvable into two orthogonal components in x' and y' directions. At zero voltage, they are equal and

project a circle as perpendicular section of the index ellipsoid, while at non zero voltage one is elongated and one reduced, forming a projected ellipse. The degree of eccentricity is indicative of the phase difference between the two. If two orthogonal polarization components of light undergo to a relative phase shift, an elliptically polarized wave will be generated. For a given wavelength of light, the produced retardation between the two components is independent on crystal dimensions and it is directly proportional to the voltage applied to the crystal in parallel to the optic axis:

$$\delta = \frac{\eta_0^3 r\, v_z}{\lambda},$$

where

δ = number of retarded wavelengths

η_0 = ordinary refraction index of the crystal

r = electro-optic constant in μm/Volts

v_z = longitudinally applied voltage in Volts

λ = light wavelength in μm

By increasing or decreasing the applied voltage, the phase shift between the two components can be varied to produce a phase difference from 0° to any value up to the voltage breakdown limit of the crystal. Light with different wavelengths requires different voltage values to obtain the same retardation.

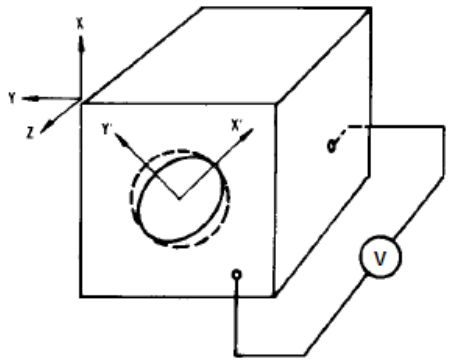

Figure 2.5 Change in shape of the index ellipsoid induced in a crystal by an external longitudinal electric field

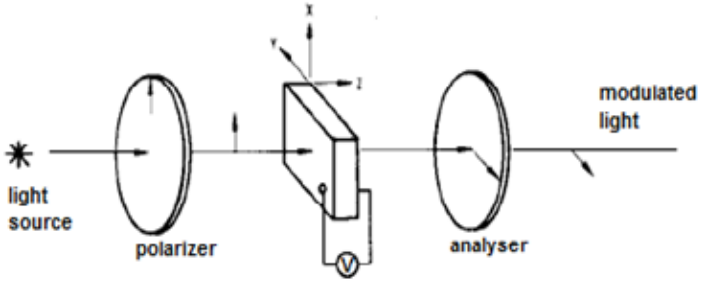

Figure 2.6 Configuration of an electro-optic modulator between crossed-polarizers

The transversal Pockels cell works in a similar way, but the geometry is different. Consider linearly polarized light which propagates through the crystal perpendicularly to the optic axis (it is polarized in the plane which contains the optic axis) in absence of external electric field, with the polarization direction forming an angle of 45° with respect to the crystal axis. The electric field wave has one component parallel to the optic axis (refractive index n_e) and one

perpendicular to it (refractive index n_o), with equal amplitudes. They propagate with different phase velocity, therefore they experience a growing phase shift. The output wave is the result of two waves polarized at 90° between them with different phase, namely an elliptically polarized wave. Hence, in the transverse geometry the crystal exhibits a natural birefringence also in absence of an external electric field.

The described phenomenon is used to modulate the light intensity. In fact, the simplest way to produce light intensity control is positioning an input polarizer before the crystal to produce linearly polarized light and an output polarizer, or analyzer, after the crystal. The polarization directions of the two polarizers can be either parallel or orthogonal (crossed polarizers, see Figure 2.6). In the longitudinal modulator, when no voltage is applied, in the first case the maximum transmission is obtained, instead in the second case the minimum transmission is found. Instead, the transverse modulator exhibits an arbitrary modulation operating point at zero applied voltage. To practically use the transversal modulator referring to the same transmission curve of the longitudinal one, is necessary to compensate the natural birefringence. In crossed polarizers configuration the correction is performed by means of a DC voltage offset which moves the crystal transmission curve from the arbitrary zero operating point to the condition of minimum transmission in correspondence to zero applied AC voltage (quiescent operation point). The graph in Figure 2.7 represents the process.

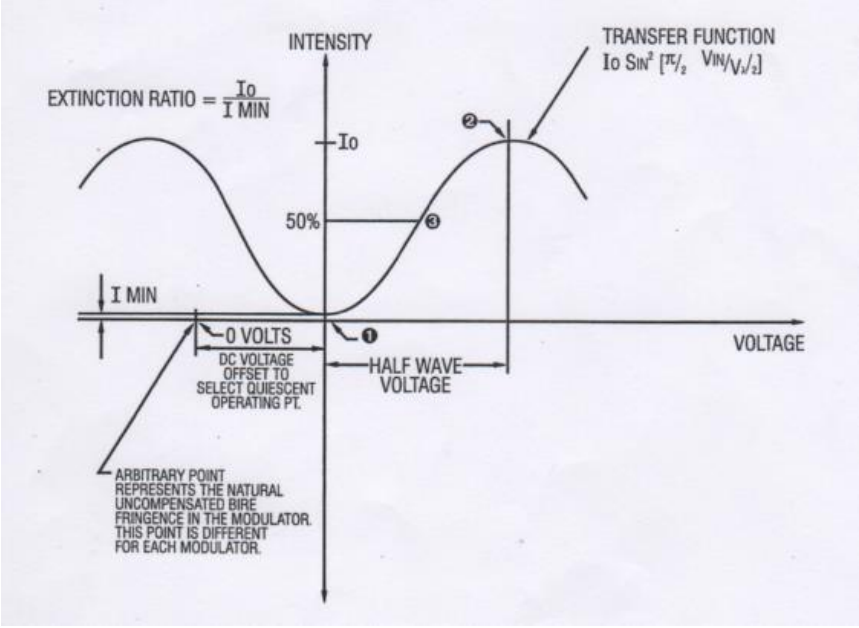

Figure 2.7 Setting of the quiescent operating point by applying DC offset voltage in the transversal modulator

Set this condition, the longitudinal and transversal modulators have the same intensity transmission curve as a function of the applied AC voltage.

The absolute value of the transmission minimum I_{min} is never really null and it is influenced by several factors, such as the uniformity of the applied electric field, the quality of polarizer and analyzer and the accuracy of their orientation, the alignment of the input beam with respect to the crystal optic axis, the incident beam divergence. The ratio between maximum and minimum output intensity is called extinction ratio or contrast ratio $ER = \frac{I_{max}}{I_{min}}$; it is controlled by the value of null transmission level I_{min} and it determinates the modulator performance: a poor null transmission value can be a serious limitation to the resulting modulation. The Pockels cell quality is affected also by contingent factors, such as thermal changes in the ambient, absorption of laser energy, electrical heating of crystal or electrodes. The Pockels cells in configuration of crossed polarizers usually provides better extinction ratios. In this configuration, when the AC voltage across the crystal is increased the transmitted light is also increased, until reaching a maximum, I_{max}; this condition coincides with a relative phase shift of 180° between the two components and a 90° rotation of the plane of polarization. Placing an output linear polarizer after the crystal, it will produce a beam of varying intensity dependent on the variable phase relation between polarization components. The output intensity I_{out} is related to the input intensity I_{in} and to the phase shift δ by the relation (2)

$$I_{out} = I_{in}\sin^2(\pi\delta) = I_{in}\sin^2\left(\pi\frac{\eta_0^3 r\, v_z}{\lambda}\right) = I_{in}\sin^2\left(\frac{\pi}{2}\frac{v_z}{V_{\lambda/2}}\right), \qquad (2)$$

where $V_{\lambda/2} = \frac{\lambda}{2\, r\, \eta_0^3}$ is the halfwave voltage, namely the voltage to apply in order to obtain a 180° shift. The relative transmission has a sine-squared relation to the applied voltage (Figure 2.8).

The Pockels cells used in the setup are electro-optic modulators (350-80LA for the pump beam and 360-80LA for the OPO beam, ConOptics Inc., Danbury, Connecticut, USA) in transverse field with a KDP crystal. The transversal geometry has the advantage of requiring approximately 100 Volts as opposed to the kilovolts of the longitudinal design.

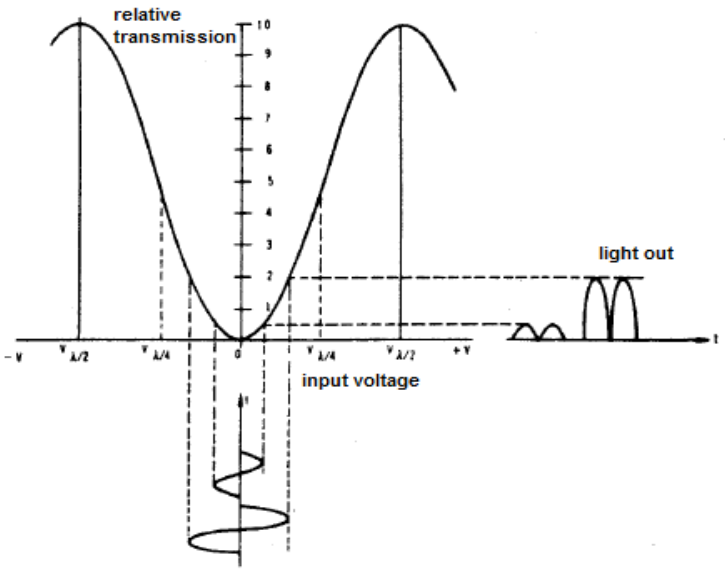

Figure 2.8 Transfer function of longitudinal electro-optic modulator between crossed polarizers

For the reasons discussed before, the power supply of Pockels cells is divided into a DC component and an AC component. The former adjusts the natural birefringence offset and is regulated manually acting on the controller of the power supply console. The latter requires the voltage effectively responsible for the light modulation and is set by means of the software *ThorImage*, where the user must specify the maximum AC voltage required by the Pockels cell $V_{AC,max}$ (better defined in section 3.1) and the desired percentage of beam power he wants to work with. *ThorImage* also controls the imaging acquisition parameters and the shutter set at the exit of the pump laser source.

Variable delay line

The two advanced microscopy techniques implemented in the setup require particular conditions of temporal synchronization between the two pulses. Since the OPO and the pump beam pathways are different, even if both pulses have 80 MHz frequency and are intrinsically synchronized, they will arrive delayed at the recombination dichroic mirror (DM in Figure 2.1) within their period of 12.5 ns. The necessity imposes the presence of a variable delay line. It consists of two mirrors mounted on a longitudinal rail in the pump beam path, which allows to modify the path length by manual control (Figure 2.9). The rail length is about 40 cm, so the total variation of path length is about 80 cm, that means the delay line is able to modify the pulse delay up to $t_{max} = \frac{0.8\ \mathrm{m}}{3 \cdot 10^8\ \mathrm{m/s}} = 2.7$ ns. The position of the variable delay line system correspondent to pulses synchronization condition will be different in the case of multicolor multiphoton microscopy or STED nanoscopy.

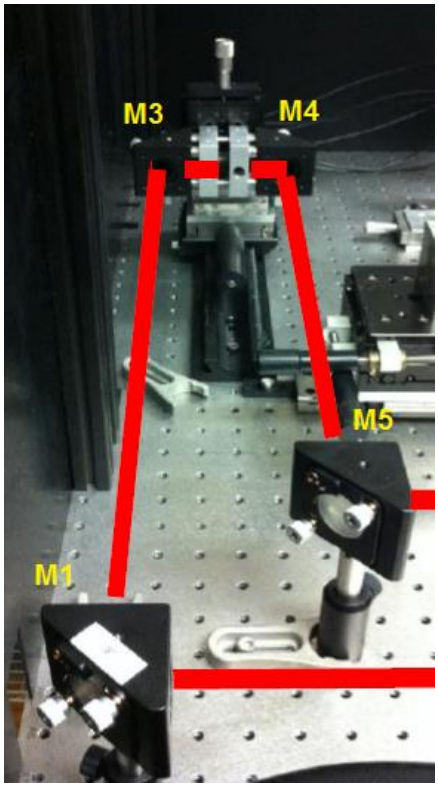

Figure 2.9 Variable delay line in the pump beam path

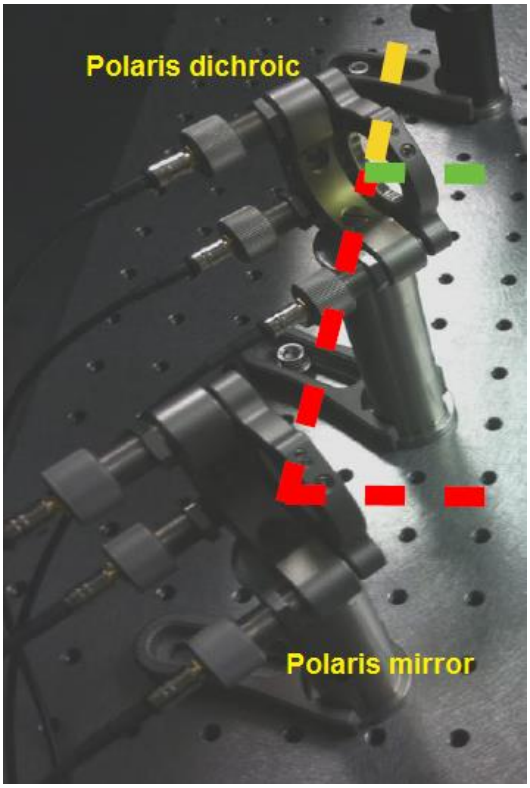

Figure 2.10 Recombination mirrors

Recombination mirrors

The spatial superposition of the two beams is crucial to obtain from both the best illumination of the back aperture of the microscope objective and consequently the overlap between the two beams focal spots. The beams must enter in the microscope body parallel to the optical bench and coaxial with high precision. To set these conditions, special kinematic mirror mounts with piezoelectric adjusters (POLARIS-K1PZ, Thorlabs) are used to hold a mirror (Polaris Mirror) and a dichroic mirror (Polaris Dichroic), shown in Figure 2.10. Polaris mirror guides the pump beam towards Polaris Dichroic, through which the recombination is effectively performed. The kinematic mirror mounts are equipped with 3-axes manual or piezo-electric control. The angular resolution for piezoelectric control is 0.5 μrad/0.1 V applied. The piezoelectric systems are alimented by two power supply consoles, one for each mirror, in which the three axes voltage values can be set manually or even from the user emplacement through the software *MDT693A Piezo Controller*.

Photodetection system

To analyze the temporal delay between the two pulses, a photodetection system is set in the last part of the light pathways, after beams recombination. It consists of a small mirror with low reflectivity (~ 0.5 %) which can be mechanically inserted and removed from the pathway, which guides a small percentage of power to a Free-Space InGaAs detector (DET08CL, rise time < 70 ps, operating wavelength range 800-1700 nm, Thorlabs). This last is connected to an oscilloscope (PicoScope 6400 C, 500 MHz bandwidth, Pico Technology Inc., St Neots, UK) through which the temporal profile of the pulses and their delay can be monitored.

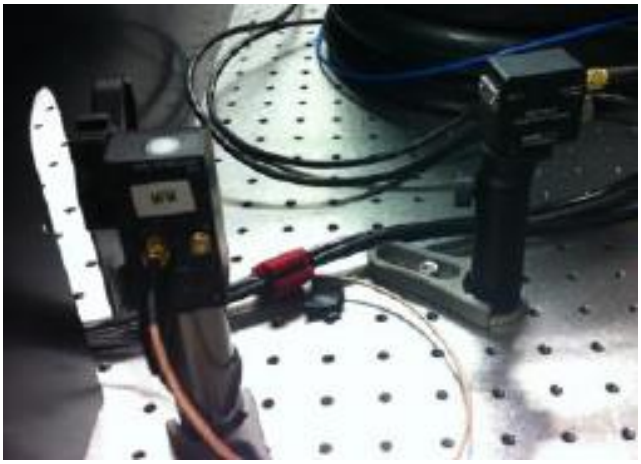

Figure 2.11 Photodetection system

Stretching line: optical fiber and glass rod

To perform STED nanoscopy, the pump beam must be stretched temporally up to a duration of several picoseconds. This condition is achieved by means of a polarization-maintaining single mode optical fiber (PM780-HP, NA 0.12, operating wavelength range 710 – 1100 nm, Thorlabs).

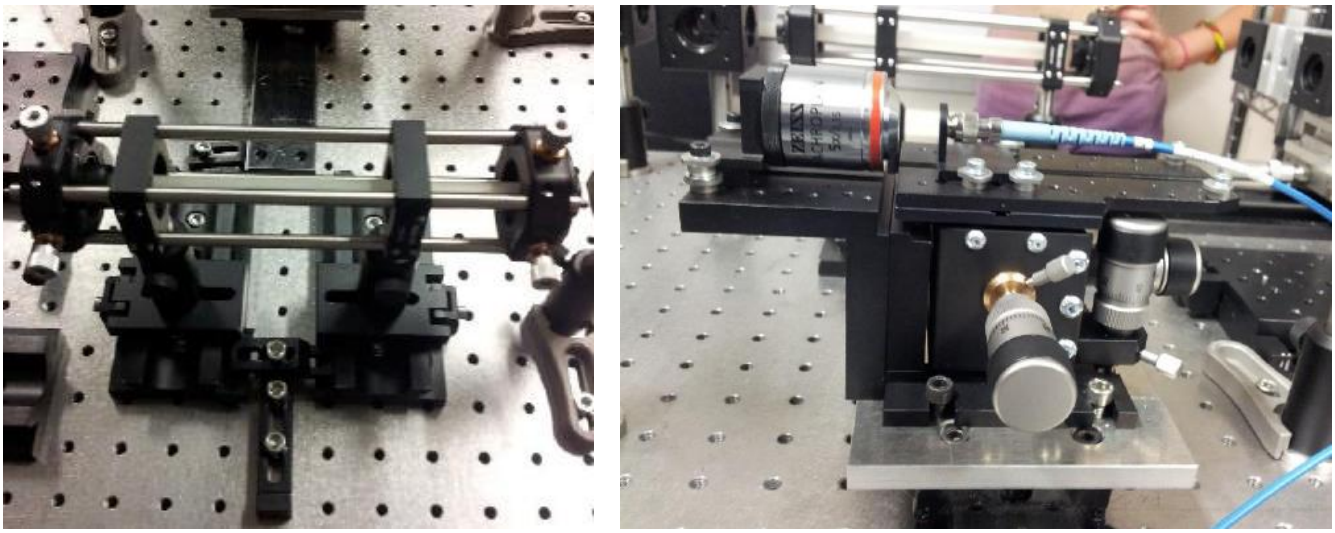

Figure 2.12 Temporal stretching line for the pump beam pulse
(a) Glass rod (b) Launch in fiber through ZEISS objective and 3-axes fiber launch

Before passing through the optical fiber, the beam crosses a simple rod of glass, inserted in the path thanks to a rail. It protects the fiber generating a first temporal stretch of the pulse from ~ 140 fs to ~ 1 ps, otherwise the fiber core would not endure the passage of such a short pulse without damages. The glass rod is ~ 20 cm long, its transversal surfaces are coated with an anti-reflection film, specific for the wavelength range 680 - 1100 nm. The optical fiber instead is 100 m long and it stretches the pulse from ~ 1 ps till ~ 10 ps. As its core diameter measures 4.6 µm, the beam needs to be accurately focused to be injected inside. For this purpose, the rail that enables to insert the fiber in the path holds a special alignment system, the fiber launch (MBT616D, Thorlabs). It is a compact flexure stage with differential micrometers, with coarse and fine adjustment range of 500 µm/revolution and 50 µm/revolution respectively. This resolution makes this stage ideal for optimizing the coupling efficiency in a fiber alignment because it allows a positioning precision with respect to the beam axis up to of 0.5 µm. The fiber launch holds the fiber entrance and exit, but also a focusing optical element, an objective or a lens, suitable to produce a focal spot with small diameter to inject the beam inside the core of the optic fiber. Switching the setup in STED configuration, both rails for the glass rod and for the fiber are manually inserted in the pump beam path.

Spiral phase plate

The wavefront modulation required by STED nanoscopy is realized by a polymeric spiral phase mask replicated on a glass substrate (VPP-1a, operating wavelength range 350 – 2000 nm, RPC Photonics, Rochester, New York, USA) placed after the exit of the optical fiber.

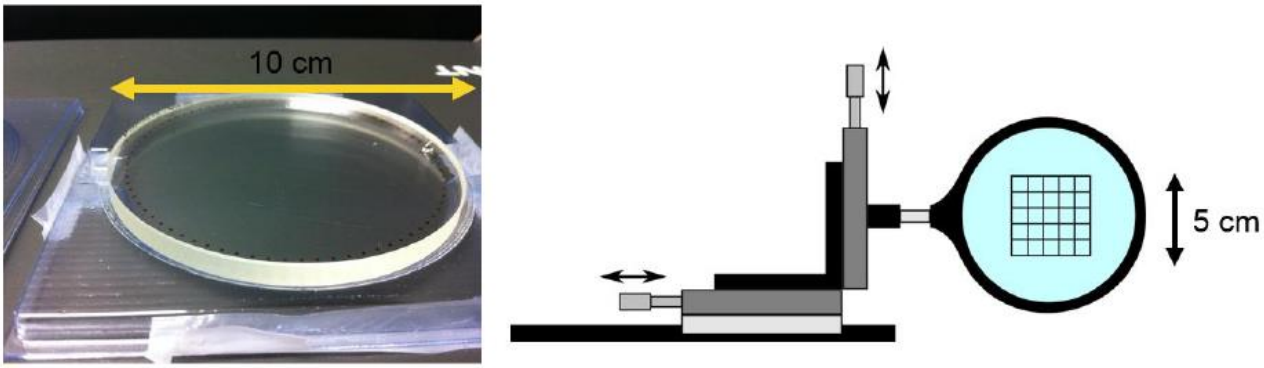

Figure 2.13 Spiral phase plate on the left, scheme of its mounting system on the right

Fixed delay line

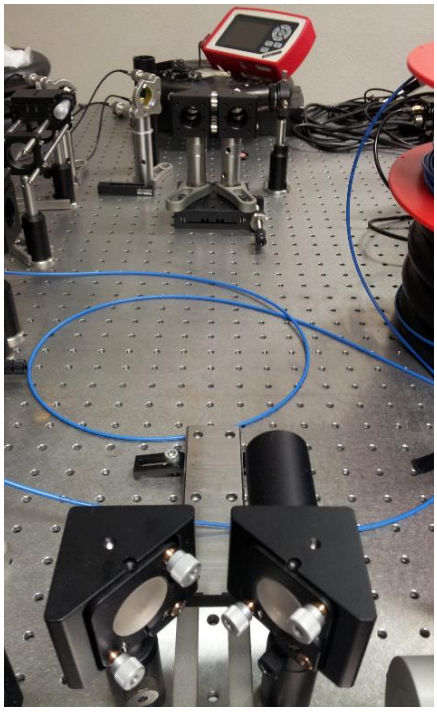

To perform STED nanoscopy the depletion beam must closely follow the excitation one (delay ~ 10 ps). At the oscilloscope (500 MHz bandwidth, rise time 70 ps) the two pulses are visualized overlapping. Since STED configuration includes more elements which introduce a higher delay with respect to the OPO beam, the condition of temporal synchronization is different from the one in multicolor multiphoton configuration. In particular, the pump beam needs to proceed along a fixed length delay line to be synchronized to the OPO pulse (as justified in Chapter 3, section 3.3). It is composed of four mirrors. Two mirrors have been inserted after the pump beam Pockels cell by means of another mobile sledge, while the other two face them at a distance aroud 65 cm on the optical bench (Figure 2.14). The first mirror deflects the light out from the normal travel and the last one allows it to return into the path and continue towards the variable delay line.

Figure 2.14 Fixed delay line

2.3 LASER SCANNING MULTIPHOTON CONFOCAL MICROSCOPE

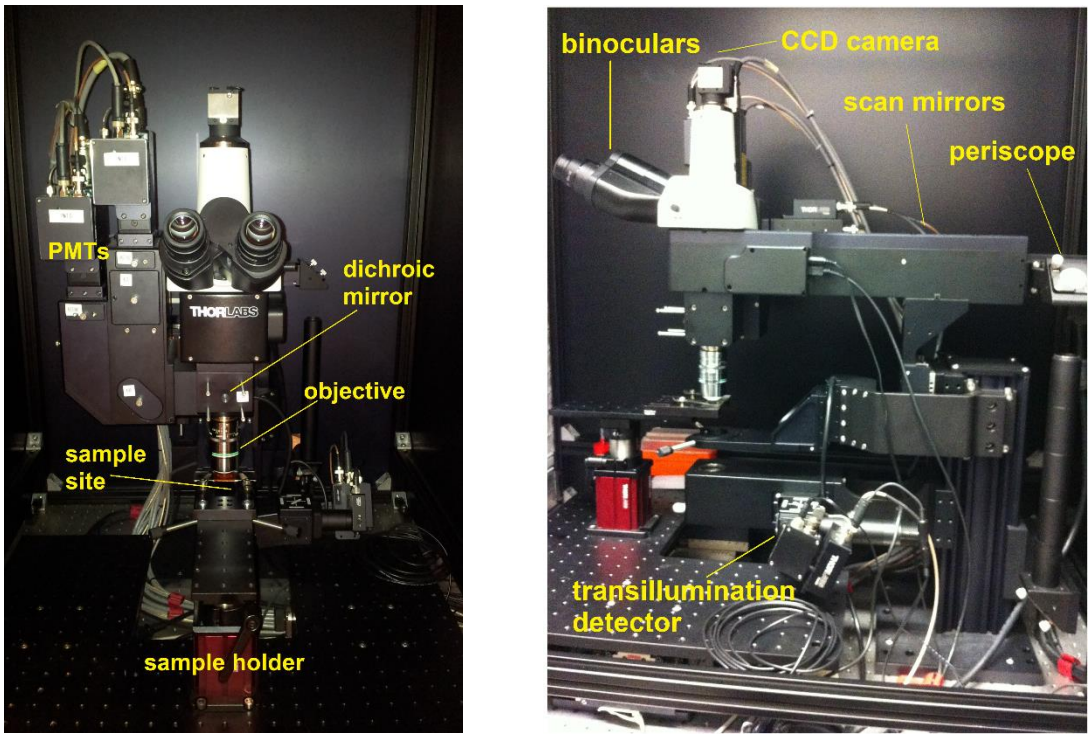

Figure 2.15 Bergamo II microscope: frotal view (left) and lateral view (right)

The laser scanning multiphoton confocal microscope included in the setup is a Bergamo II System B232, Thorlabs. The first element encountered by the light beams at the entrance of the microscope is the periscope. It is composed of two mirrors separated by a vertical path (Figure 2.16a); it guides the light towards the scan head of the system. The scan head is made up of two galvo/resonance scan mirrors able to raster the sample at 8 KHz rate (Figure 2.16b). The galvo mirrors realize the illumination of the objective back aperture; the beam is therefore focused at the focal plane on the sample placed below. The microscope is in epifluorescence configuration, namely the roles of objective and condenser is played by the only objective: it is crossed before by the illumination light going towards the sample, after by the emission light coming from the sample. The two are physically separated through a longpass 705 nm dichroic mirror, which transmits the illumination light, while reflects the emission light towards the detection module (Figure 2.17a). The detection module is composed of four photomultipliers (4x GaAsP PMT) associated to the following band-pass filters

- Channel A: [UV] (395 $\pm$ 25) nm
- Channel B: [Blue] (460 $\pm$ 50) nm

- Channel C: [Green] (525 $\pm$ 40) nm
- Channel D: [Red] (625 $\pm$ 90) nm

for the detection of a broad range of wavelengths. The emission light is directed towards the correct detection channel by means of three dichroic mirrors which reflect light at

- 425 nm (Ch. A and B);
- 495 nm (Ch. B and C);
- 565 nm (Ch. C and D).

Figure 2.16 Microscope illumination path (before the objective)

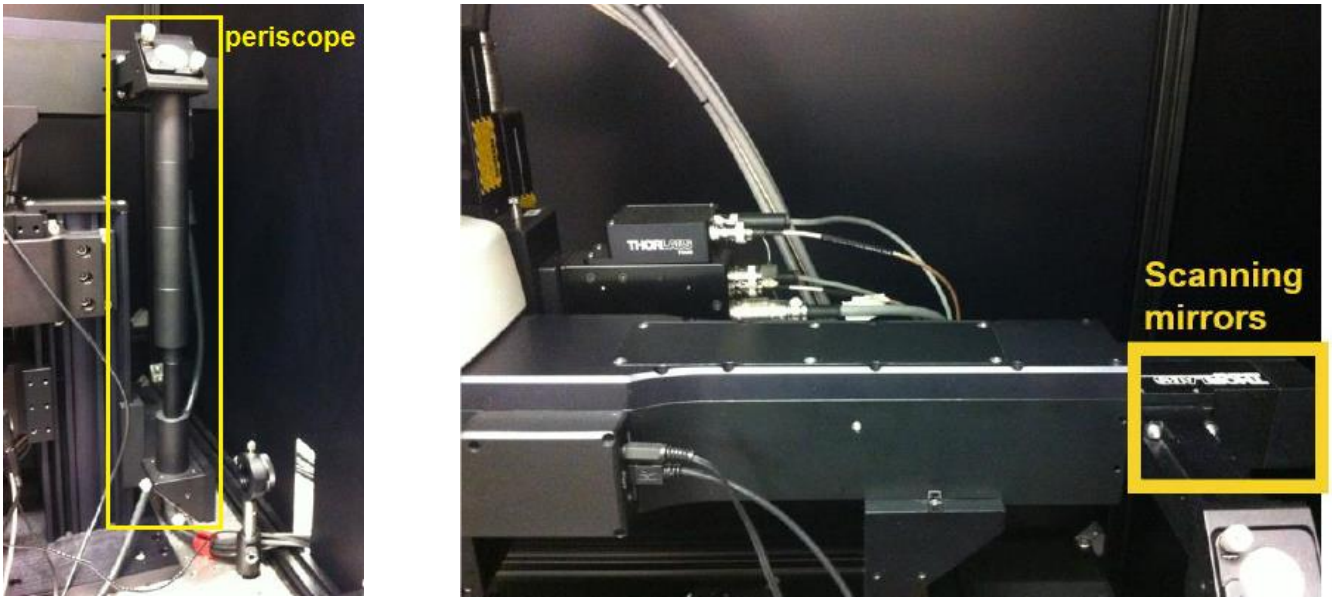

(a) Periscope

(b) Scan head

The microscope also allows imaging in transmitted light. In this case, the light transmitted by the sample is collected by the condenser placed below the sample site and sent to an InGaAs detector (DET08CL, operating wavelength range 800-1800 nm) visible in Figure 2.17b. The light can reach the detector only if a preceding mirror placed inside a mounting cube is removed. On the contrary, when the mirror is inserted it allows the illumination of the sample by a LED source; this last is necessary to find the coarse focus condition of the specimen before starting an experiment, observing it directly through the provided binoculars.

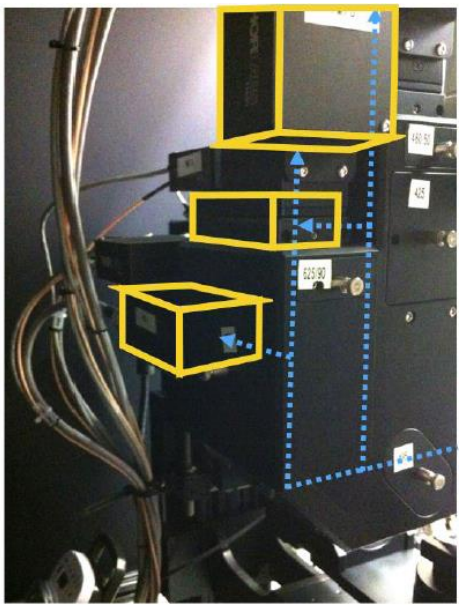

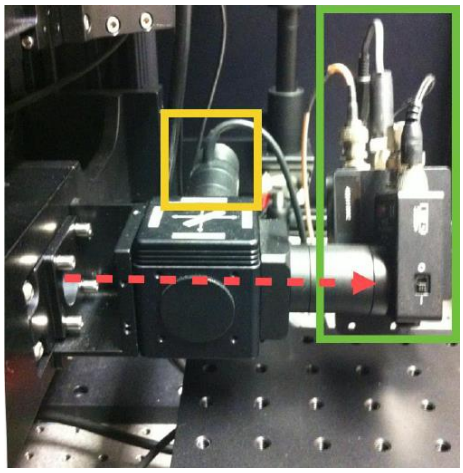

Figure 2.17 Detection module.
(a) The fourth PMT is hidden by the module. The blue dotted lines show the light path reaching each PMT.

(b)Transillumination detector (green box) and LED source (yellow box). The red dotted line shows the transmitted light path when the mirror in the cube is removed.

2.4 CALIBRATION SAMPLES

Quantum Dots

Quantum dots (QD) are semiconductor nanoparticles with high photostability and broad emission spectrum, from the visible to the mid infrared region, depending on their size and composition (35). The QD samples we used were fabricated at the Department of Industrial Engineering of the University of Padua. They consist of nanoparticles produced in non-polar solvents and thereafter transferred into sol-gel matrices. A ZnO-SiO_2 hybrid sol-gel glass films was doped with PbS quantum dots. Both the absorption and the emission properties of the semiconductor nanocrystals are only slightly affected by the incorporation into the sol–gel matrix. The glass film containing the QDs is simply laid on a glass slide and set in the sample site for the observation at the microscope. These samples are fundamental to characterize the microscope and objectives performances, in particular in terms of resolution and achromaticity, as well as to check the beams alignment.

FluoCells

FluoCells prepared slide #3 (Thermo Fisher Scientific Inc., USA) is a fixed biologic specimen containing a 16 µm cryostat section of mouse kidney stained with three different fluorophores, whose spectra are shown in the Figure below.

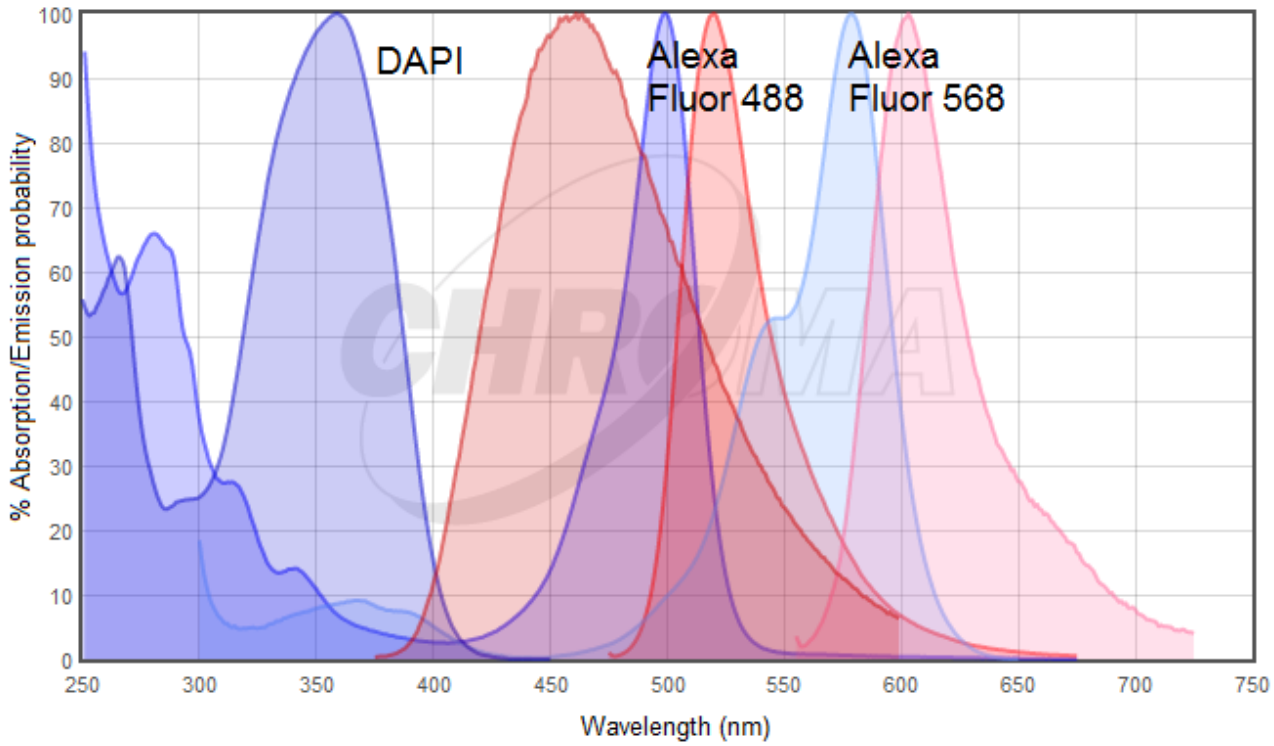

Figure 2.18 DAPI, Alexa Fluor 488 and Alexa Fluor 568 fluorescence spectra (1P excitation and emission)[2]

This auxiliary sample was used to quantify the fluorescence signal increment obtained thanks to the synchronization of the acquisition with respect to the excitation pulse.

KDP powder

A fine powder of Potassium dihydrogen phosphate (KDP, J. T. Backer, Center Valley, PA, U.S.A.) was spread on a slide, within a barrier made of vaseline, then the slide was sealed by a coverslip for imaging under the microscope. This specimen is useful for the observation of parametric processes (SHG, SFG).

Alexa Fluor samples

Some drops of Alexa Fluor 594, 568 and 556 fluorophores were placed between a glass slide and a coverslip, with an aqueous mounting solution in order to reduce photobleaching. Each sample is finally sealed with varnish.

[2] From https://www.chroma.com/spectra-viewer/fluorochromes

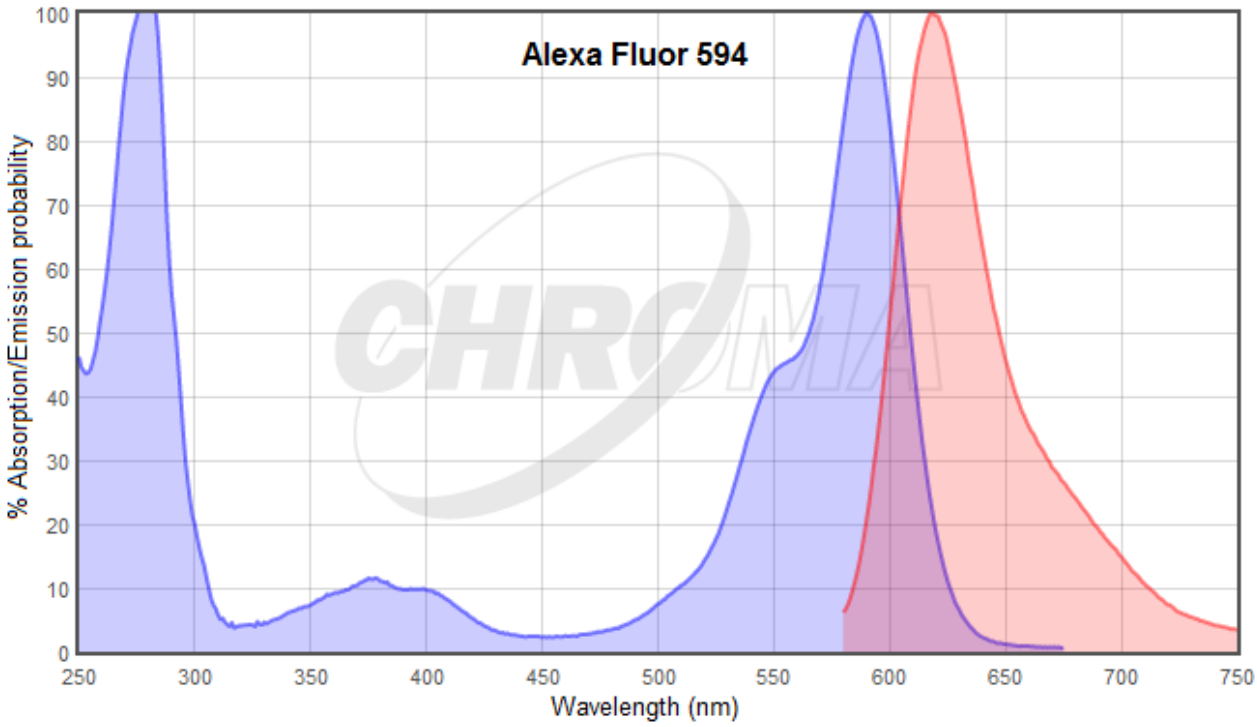

Figure 2.19 Alexa Fluor 594 fluorescence spectra (1P excitation and emission)[3]

[3] From https://www.chroma.com/spectra-viewer/fluorochromes

3 METHODS

This chapter presents the procedures for the calibration and characterization of the instrument, as well as the methods used to set the basic spatial and temporal working conditions required by the advanced microscopy techniques. Furthermore, some choices of optical elements rather than others for the setup are discussed according to the features required.

3.1 PROCEDURE FOR THE OPTIMIZATION OF POCKELS CELL TRANSMITTANCE

All the beams power measurements are performed by means of the power meter, a thermal power sensor (S305C, Thorlabs).

Procedure for the Pockels cells alignment

To avoid light losses it is necessary to finely align entrance and exit of the Pockels cell with respect to the incoming laser beam axis.

The steps of the alignment procedure are:

- switch off the Pockels cell;
- position the power meter in front of the Pockels cell exit;
- maximize light passage by power meter reading while moving the device in x and y directions and rotating it around its axis;
- switch on the Pockels cell;
- determinate the values of the cell DC power supply that correspond to maximum ($\mathrm{P_{max}}$) and minimum ($\mathrm{P_{min}}$) light transmission. Compute the extinction ratio, defined as $\mathrm{ER} = \frac{\mathrm{P_{max}}}{\mathrm{P_{min}}}$;
- set the power supply controller to the value $\mathrm{V_{min,DC}}$ corresponding to $\mathrm{P_{min}}$;
- slightly rotate the screw which controls yaw (Figure 3.1) in the cell 6-degrees-of-freedom support (x-y-z-pitch-yaw-roll). After every movement compute ER as described above. The movement is accepted if it increases or keeps $\mathrm{P_{max}}$ constant and decreases $\mathrm{P_{min}}$;
- repeat the last step acting on the pitch control;
- in the final configuration, $\mathrm{V_{min,DC}}$ corresponds to the optimal value of minimum transmission and ER is maximized.

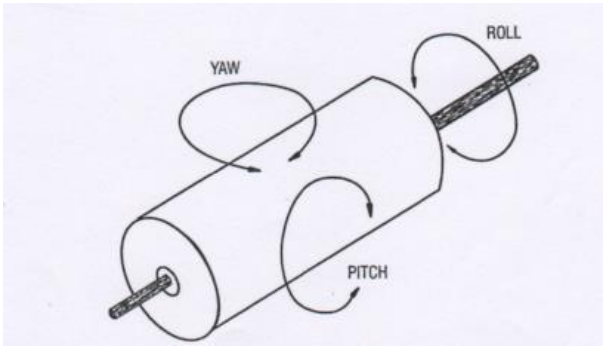

Figure 3.1 Three degrees of freedom of the Pockels cell support

Procedure for the optimization of Pockels cell transmittance

The Pockels cell introduces an intensity modulation dependent on the laser beam wavelength, therefore the values of DC and AC power supply requested for maximum and minimum transmission change according to the selected wavelength. Before working with the microscope, it is necessary to find out the required DC and AC supply voltages as a function of wavelength. The operative procedure is described below.

DC VOLTAGE

- Select the desired wavelength;
- position the power meter in front of the Pockels cell exit;
- verify that the power supply controller output is set on "unipolar positive";
- identify through power meter reading the DC voltage value $V_{min,DC}$ corresponding to the condition of minimum transmission, acting on the power supply controller; maintain the power supply controller set on $V_{min,DC}$ during the following AC voltage calibration.

AC VOLTAGE

- Apply a supplementary AC voltage by means of the apposite software *NI PCI e-6363 Measurement and Automation*. Vary the applied voltage until the value $V_{max,AC}$ that maximizes the transmission is determined through power meter reading;
- $V_{max,AC}$ obtained for a certain wavelength and $V_{min,AC} = 0$ V for all must be set on *ThorImage* software to work with that specific wavelength;
- repeat the entire procedure for other wavelengths.

Arranging the obtained values of $V_{min,DC}$ and $V_{max,AC}$ as a function of wavelength, DC and AC supply calibration curves are produced for each Pockels cell. Before starting any experiment,

the user has to make reference to these curves and set the values of Pockels cells supply required for the desired wavelengths.

3.2 PROCEDURE FOR THE ALIGNMENT OF THE MULTIPHOTON BEAMS

The procedure basically consists in the careful positioning of the mirrors required for beam stirring on the optical bench. The pump and OPO beams start their travel from two ports on the OPO, where they exit parallel to each other and at the same height over the optical bench. Thereafter, the beams encounter different optical elements before being recombined. The recombined beams must enter the microscope periscope at the same point and with the same angle so that the objective back aperture can be equally illuminated by both. In addition, under suitable achromaticity conditions, the two beams should be focused by the objective onto the same spot.

To meet the above requirements, each mirror is initially positioned roughly at 45° with respect to the beam optic axis. Then, the mirrors are finely oriented by means of two screws which permit to adjust the direction cosines of the outgoing beam. The process requires a system of fixed reference points chosen among the optical elements available on the bench. It is mandatory to center both beams perfectly in each of those elements and to ensure that movement of the variable delay line does not introduce any shift or bending of the beam optic axes. The standard procedure for centering the beam at a reference point consists on acting on two preceding optical elements in an iterative way. The alignment procedure is simplified in the first part by the use of fluorescent test targets which can be mounted on the optical elements entrance or exit. The targets permit to visualize the beam entry point and to correct it if required. The second step is to replace the fluorescent target with a variable diaphragm, which can be reduced to a pinhole. The power meter is placed behind the pinhole and the measured power must be maximized by stirring around the incoming beam. With reference to Figure 2.1 (Chapter 2) the reference points we selected are:

for the pump beam

- M3, at the entrance of the variable delay line;
- M5, immediately after the variable delay line and the glass rod in STED configuration;

for both beams

- the two pinholes placed after the recombination mirrors (P1) and before the periscope (P2).

Alignment of the variable delay line

1) The alignment of the pump beam to the center of M3 (Figure 2.1) requires placing a test target on M3. The steps followed are:

   - place DL1 as close as possible to M1;
   - shift DL1 in x and y directions by means of the suitable positioning screws to center the beam in M3;
   - place DL1 as far as possible from M1;
   - center the beam in M3 target by means of M1 screws;
   - repeat iteratively the previous four actions until the screws sensibility limit is reached.

1) The alignment of the pump beam to the center of M5 (Figure 2.1) requires placing a test target on M5. The steps are:
   - place DL1 as close as possible to M5;
   - center the beam in M5 target by means of M3 screws;
   - place DL1 as far as possible from M5;
   - center the beam in M5 target by means of M4 screws;
   - repeat iteratively the previous four actions until the screws sensibility limit is reached.

For a very fine orientation adjustment, the points 1 and 2 can be repeated substituting the target with a pinhole and placing the power meter immediately after the reference mirror (M3 or M5).

Alignment of the recombination mirrors

For the pump beam, the manipulation is performed on M6 and M7. It requires placing a test target on P1 and one on P2. The steps are:

- center the beam in P1 target by means of M6 screws;
- center the beam in P2 target by means of M7 screws;
- repeat iteratively the previous two actions until the screws sensibility limit is reached;
- repeat the previous three points using the power meter sensor behind the pinholes, without the targets.

For the OPO beam the procedure is exactly the same, with M2 instead of M6 and DM instead of M7.

Alignment of the optical fiber

When the optical bench is switched from multicolor multiphoton configuration to STED configuration, a realignment of the fiber launch (which holds the focusing element and the fiber entrance and exit) is required. Since the fiber core diameter is really small, it can be necessary to proceed by steps and to align the fiber launch progressively with the help of auxiliary multimode optic fibers with decreasing diameters. The fibers available in the laboratory have core diameters of 400, 105 and 50 μm. The steps of the procedure are:

- place the thermal sensor at the exit of the mounted fiber;
- locate and maximize the output signal by moving the x, y, z screws of the fiber launch;
- swipe to a fiber with a smaller core diameter and repeat the maximization;
- insert the single mode optic fiber and optimize the final beam-fiber coupling as the last step.

Alignment of the periscope

- Remove the protective Aluminum cylinders from the vertical path between the two periscope mirrors and mount a test target on the upper one;
- center the beam in the upper mirror target by regulating the screws of the lower mirror;
- the alignment can be checked observing directly the beam projected on a fluorescent target placed in the sample site, without the objective; it can be corrected slightly moving the two mirrors screws.

The real end of the alignment procedure of all the setup is performed before starting the experiment. Over time some small optic elements drifts or some vibrations can deteriorate the quality of the objective back aperture illumination and the two beams coaxiality. The user has the possibility to correct the alignment without modifying anything in the setup manually, but exploiting the piezoelectric systems available in the recombination mirrors holders. In fact, by applying separately in x, y or z axes an appropriate voltage (between 0 and 150 Volts) to M7 or to DM piezo controllers via software (*MDT693A Piezo Controller*), the pump or the OPO beam respectively moves. The operation is concluded when, observing a sample at minimum magnification (0.6x), the pupil appears entirely and uniformly filled. Alternatively, the correction can be applied observing QDs (see section 2.4) on a slide at maximum magnification (32x). The QDs size under the optical resolution limit makes them behave as point sources. A single quantum dot is selected and imaged by both beams; acting on piezoelectric voltages, the perfect alignment is achieved when the two images overlap in (x, y) plane. The procedure is illustrated in Figure 3.2: the QD is imaged through the pump beam and centered in a ROI; the

illumination is switched into the OPO beam, visualizing the same ROI. The OPO beam alignment is corrected by mean of piezoelectric control until the two QD images overlap.

Figure 3.2 Alignment correction through piezoelectric control at 32x magnification

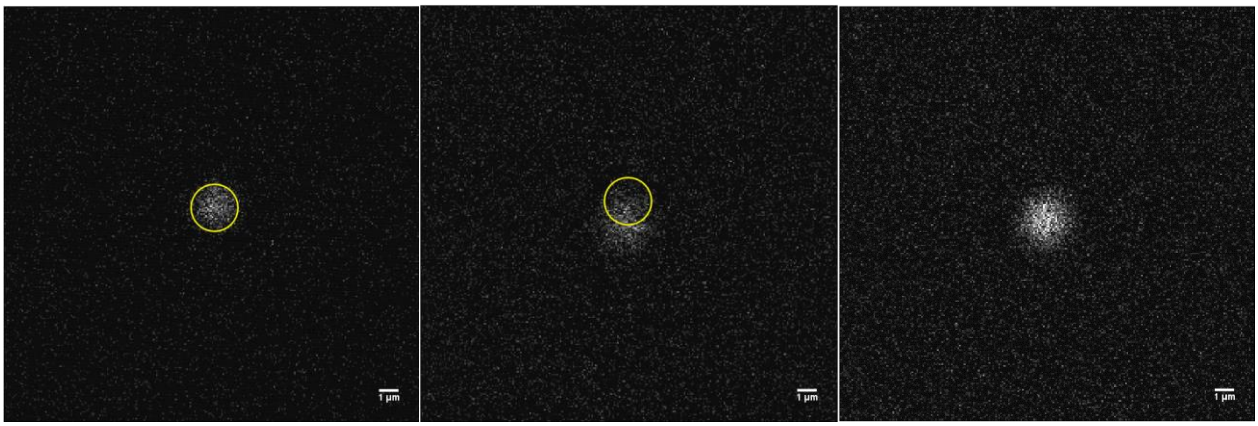

(a) pump beam (b) OPO beam before correction (c) both beams after correction

3.3 PROCEDURE FOR THE TEMPORAL SYNCHRONIZATION OF THE PULSES

Multicolor multiphoton configuration

The synchronization of the two pulses is fundamental to perform both two-beam multicolor multiphoton imaging and STED nanoscopy. In case of multicolor multiphoton imaging in fact, the relative delay τ must be small enough to permit a good efficiency in the emission of the third signal. As we saw in section 1.3.3, the intensity of the third fluorescence signal decreases exponentially with τ^2. In order to get as much information as possible about the sample from multicolor multiphoton imaging, we can fix the maximum borne loss due to temporal mismatch between pump and OPO pulses at 1 %.

$$\frac{I_{\lambda_3}}{I_0} = \exp\left(-\frac{\tau^2}{2\sigma^2}\right) = 0.99,$$

where $I_0$is the theoretical emitted intensity if the pulses were perfectly synchronized. The $1/e^2$ width (2σ) of the temporal intensity intercorrelation function between two Gaussian pulses with durations $\tau_{Ti:s} \sim 140$ fs and $\tau_{OPO} \sim 200$ fs is

$$2\sigma = 2\sqrt{{\sigma_{Ti:S}}^2 + {\sigma_{OPO}}^2} \sim 244 \text{ fs},$$

from which

$$\sigma = \frac{\tau_{pulse}}{\sqrt{2}} \sim 122 \text{ fs}$$

therefore the maximum acceptable delay is

$$\tau = \sqrt{-2\sigma^2 \ln\left(\frac{I_{\lambda_3}}{I_0}\right)} \sim 17 \text{ fs} \sim \tau_{pulse}/10.$$

In such an interval of time the light travels for

$$\Delta x = c\tau = 3 \cdot 10^8 \text{ m/s} \cdot 17 \cdot 10^{-15} \text{s} = 5.1 \text{ μm}.$$

This suggests that the sensibility needed to regulate the temporal synchronization condition by means of the movement of the mobile delay line is 1 μm. This limit is not reachable simply manually, but the help of a graduated micrometric head is required.

The first step to set the temporal multicolor multiphoton condition is the overlapping of the two pulses at the oscilloscope, moving simply by hands the delay line. The oscilloscope available in the laboratory has a rise time of 70 ps: a femtosecond pulse will be shaped as a bell large 140 ps. The coarse positioning at the oscilloscope at maximum allows a precision of

$$\Delta X = 3 \cdot 10^8 \frac{\text{m}}{\text{s}} \cdot 140 \cdot 10^{-12} \text{s} = 42 \text{ mm},$$

among which the zero delay condition between the two is included. The second step is using the micrometric head for a fine position adjustment. Since the movement of the variable delay line for a distance Δx produces a double variation of the light path $2\Delta x$ (it is composed of two mirrors), the total travel of the micrometric head must be at least 21 mm.

The choice relapsed into the DM17-25 differential micrometer (Thorlabs), with the following features:

- 25 mm coarse travel;
- 1 mm fine travel;
- 10 μm coarse graduation;
- 1 μm fine graduation.

The small mobile mirror with low reflectivity has been inserted in the path in order to analyze the temporal profile of the beams through the fast photodetector described in section 2.2. Both beams were present at the same time, so that three signals were simultaneously visualized at the oscilloscope: the two beams pulses detected in the last region of their paths and the pump pulse extracted directly from the source output. This last is used as trigger for the oscilloscope and as reference for the visualization. The coarse temporal synchronization is an iterative process: the temporal delay of the pump pulse compared with the OPO pulse is measured first,

then the path length variation (a reduction or an extension according to the need) to produce through the delay line movement is computed $\Delta x_{DL} = -\frac{c\Delta t}{2}$, with $\Delta t = t_{pump} - t_{OPO}$. After the delay line movement is accomplished manually, the synchronization condition must be checked again because the oscilloscope precision is in the order of tens of ps, spatially correspondent to a light travel of 3 mm, furthermore the manual positioning is affected by a similar error. Once the temporal delay between the pulses cannot be shortened anymore by means of this procedure, the coarse temporal alignment is concluded. The Figure 3.3 shows the final coarse temporal alignment condition set at the oscilloscope as starting point for finer synchronization. The pulses are overlapping and the measurement result is comparable to the instrument precision.

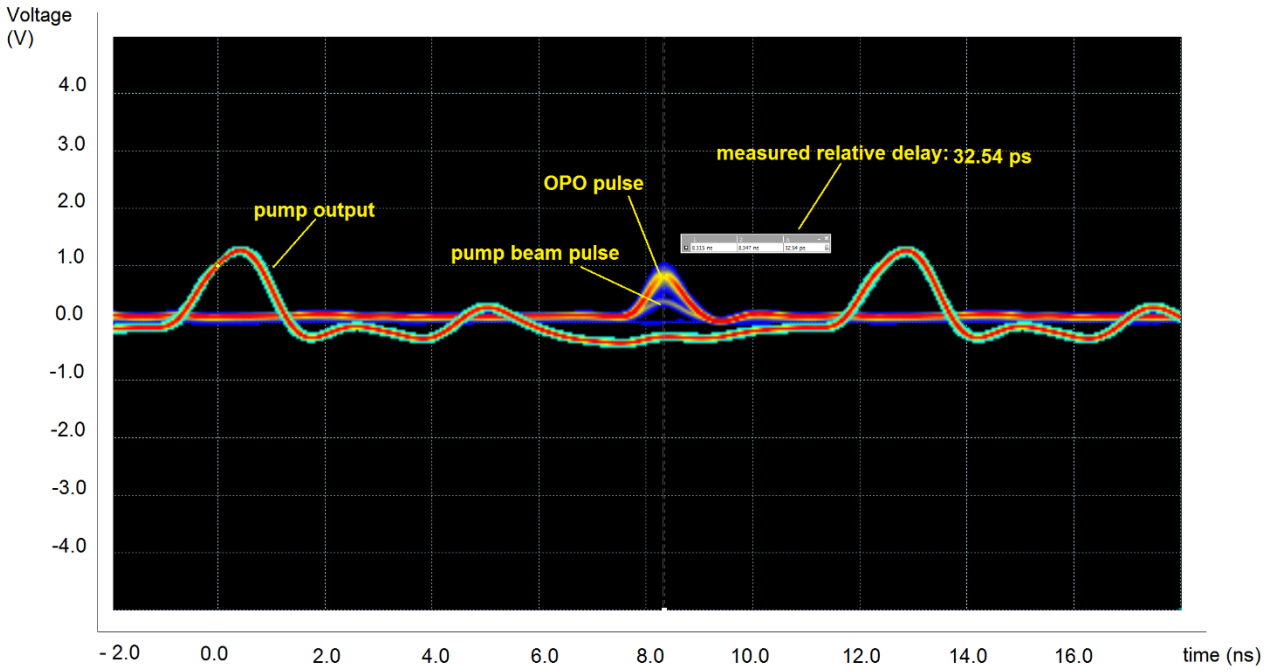

Figure 3.3 Coarse temporal synchronization of the pulses for multicolor multiphoton configuration

The oscilloscope is no more useful to find the correct fine position of the mobile delay line; the temporal synchronization must be improved observing at the microscope an auxiliary non fluorescent specimen, such as KDP powder on a slide, and maximizing the signal obtained from the sum frequency generation phenomenon (explained in section 1.3.2).

STED configuration

The procedure is the one previously described for multicolor configuration. The first measurement in this case gave a temporal delay between the pump and the OPO pulse around $\Delta t \cong -5$ ns, equivalent to a position correction

$$\Delta x_{DL} = -\frac{c\Delta t}{2} \cong 1.5 \text{ m}.$$

The correction is clearly out of the variable delay line range, which provides a maximum path variation of around 80 cm. Since there is no possibility to anticipate the OPO pulse reducing its travel on the optical bench, the only way to make the pulses coincide is retarding the pump pulse of the appropriate interval of time, by increasing its travel distance. The solution has been the introduction of the second delay line described in section 2.2 in the pump beam path. As a result of this improvement in the setup, the movement of DL1 now is sufficient to set also the STED configuration temporal synchronization condition.

3.4 LASER LAUNCH INTO SINGLE MODE OPTICAL FIBER FOR STED NANOSCOPY

To perform STED nanoscopy strict conditions must be set. As seen in section 1.4 for what concern temporal conditions, the pump pulse must closely follow the excitation pulse and be large enough to allow higher vibrational states in the lower energy level, S_0^{vib}, to relax to the ground state S_0. Since the characteristic vibrational relaxation time of fluorophores is $\tau_{vib} \leq 1$ ps, pump pulse duration has to be in the order of several picoseconds. The Ti:Sapphire laser pulses are $\sim$ 140 fs long, therefore in the pump beam pathway an optical fiber is included to extend temporally the pulse and reach the order of picoseconds.

The chosen fiber is a polarization-maintaining single mode optical fiber (PM780-HP, Thorlabs), with following specifications:

- 100 m length;
- 4.6 µm core diameter;
- 0.12 numerical aperture (NA);
- 770 - 1100 nm operating wavelength range;
- $\leq$ 4 dB/Km attenuation at wavelength 850 nm.

The beam launch in the fiber is a critical step for success of the imaging setup, because power drops at the fiber entrance are usually significant; at the fiber exit, the beam energy must be

sufficient to deplete fluorophore spontaneous emission at sample, therefore losses must be reduced as much as possible. For this purpose, the beam is focalized before the fiber and adapted to it. In particular, there are two parameters to be matched between the beam and the fiber: the numerical aperture NA and the spot diameter. This matching imposes inflexible conditions for the focal length f of the lens used to inject the light in the fiber. In fact, to minimize the energy loss caused by attenuation inside the fiber, the first condition is

$$\mathrm{NA_{fiber}} \sim \mathrm{NA_{beam}} \sim 0.12.$$

Under hypothesis of small angles, sine can be approximated with tangent, therefore

$$\mathrm{NA_{beam}} = \mathrm{n} \sin \mu \sim \tan \mu = \frac{\mathrm{D_{beam}}}{2\,\mathrm{f}}$$

with $\mathrm{n} \sim 1$ refraction index of the air, μ half aperture angle of the focal light cone and $\mathrm{D_{beam}}$ beam diameter.
With regard to the spot diameter, for Gaussian beams it is given by

$$\mathrm{d_{spot}} = \frac{2\lambda}{\pi\,\mathrm{NA_{beam}}}$$

consequently the second condition turns out to be

$$\mathrm{d_{spot}} = \frac{2\lambda}{\pi\,\mathrm{NA_{beam}}} \sim \mathrm{d_{fiber}} = 4.6\ \mu\mathrm{m}$$

Replacing in the previous expression the approximated $\mathrm{NA_{beam}}$ formula we obtain, solving for f

$$\mathrm{f} \sim \frac{\mathrm{D_{beam}} \pi\, \mathrm{d_{fiber}}}{4\,\lambda} \cong 3.61\ \frac{\mathrm{D_{beam}}}{\lambda}\ \mu\mathrm{m}$$

with $\mathrm{D_{beam}}$ and λ measured with the same unit.

In order to make the choice of the lens with the correct focal length, we need to measure the value of $\mathrm{D_{beam}}$. The measurement of the beam diameter in x and y directions is performed through the Shack-Hartmann wavefront sensor, after the mirror M6 in the region where the beam must be injected in the fiber. The average estimate between x and y direction is

$$\mathrm{D_{beam}} = 2.5\ \pm 0.2\ \mathrm{mm},$$

hence

$f \sim 12$ mm.

Two solutions with the lower possible focal length f were tested for beam injection in the fiber:

- an achromatic doublet, ACA254-030-B, $f = 30$ mm (Thorlabs);
- an objective, N-ACHROPLAN 5x, NA = 0.13, $f =$mm (ZEISS).

3.5 BEAM WAVEFRONT ANALYSIS

The measurement of shape, curvature and diameter of the beam wavefront is performed by way of a Shack-Hartmann sensor (WF150-5C, Thorlabs). The Shack-Hartmann (S-H) sensor is a fast CCD camera placed at the focal plane of a two-dimensional lenslet array. As we can see in Figure 3.4, the lenslet array divides the incoming wavefront into an array of smaller beams: if the wavefront is uniform and planar, each lenslet forms a spot along its optical axis and a regularly spaced grid of spots is created at the detector plane. Instead a distorted wavefront causes some lenslets to focus with the spot displaced from the optical axis. Therefore, the pattern becomes irregular, some spots are regularly spaced and some others are displaced or missing. The shape of a generic wavefront is computed through an algorithm starting from the displacements of spots positions compared with the ones in the plane wavefront pattern. This kind of wavefront sensor is used to characterize the performance of optical systems or in adaptive optics.

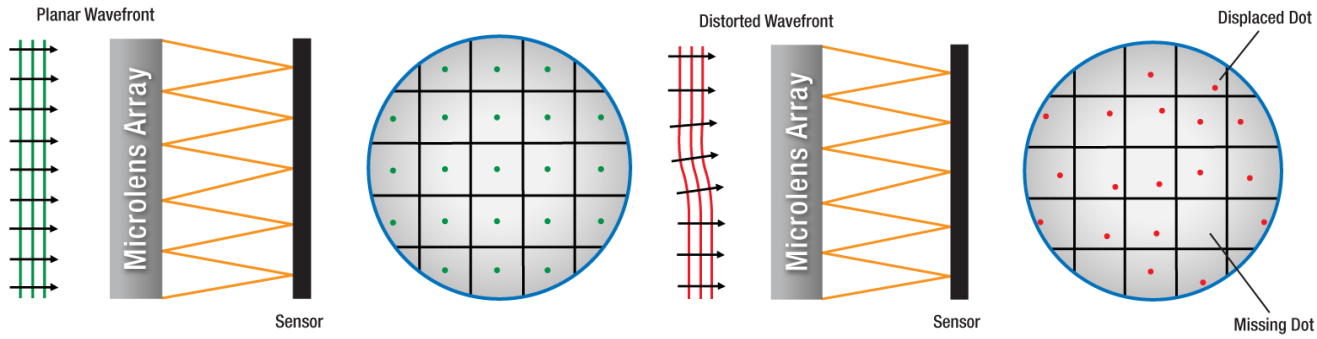

Figure 3.4 Working principle of the Shack-Hartmann sensor[4]

The Figure 3.5 is a detail of a wavefront incident on a single microlens. For a wavefront which is distorted in the region of the microlens, the spot position is deviated in the x and y direction with respect to the position taken by the planar wavefront spot. Every displaced spot lies away

[4] From https://www.thorlabs.de/newgrouppage9.cfm?objectgroup_id=2946

from the optical axis z of its associated microlens by an angle α, which is the same as the angle between the distorted wavefront and the planar wavefront.

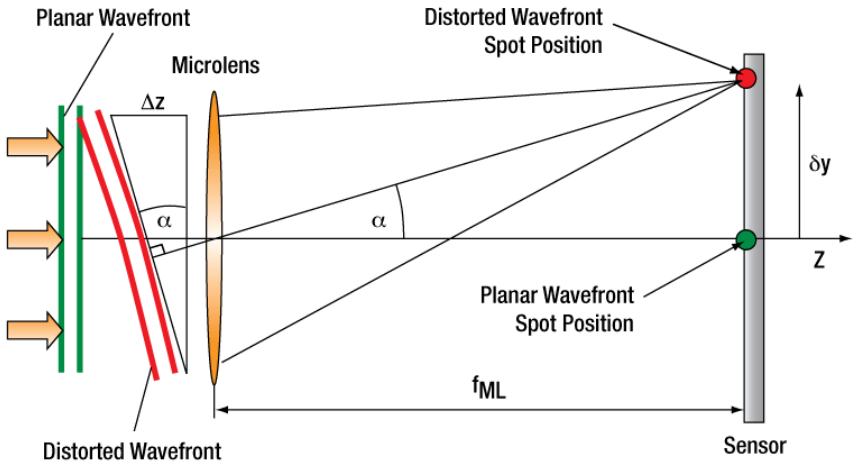

Figure 3.5 Spot displacement caused by wavefront distortion in the Shack-Hartmann sensor[5]

The instrument sensitivity is given by α_{min}, the minimum detectable wavefront slope that can be measured, which is a function of the minimum detectable spot displacement δy_{min}. In the small angle approximation in fact $\alpha_{min} = \frac{\delta y_{min}}{f_{ML}}$, where f_{ML} is the focal length of the microlens. The minimum detectable spot displacement δy_{min} depends on the pixel size of the detector, the accuracy of the centroid algorithm, and the signal to noise ratio of the sensor. The S-H wavefront sensor is capable of providing information about the intensity profile as well as the calculated wavefront. In fact, each spot is analyzed for location, but also for intensity. Using this method, Shack-Hartmann wavefront sensors can dynamically measure the wavefronts of laser sources or characterize the wavefront distortion caused by optical components.

The instrument available in the laboratory is composed of a CCD camera with 15 Hz frame rate and a lenslet array with a pitch of 150 μm and focal length 3.7 mm. The operating wavelength range is 300-1100 nm. The minimum detectable spot displacement δy_{min}. is $\lambda/_{50}$ (root mean square of the centroid), hence $\alpha_{min} \sim 5$ μrad. The sensor is very sensitive and can endure only low powers, in the order of some mW, without saturating. Thus, a birefringent polarizer designed for high power laser light (GL10, Thorlabs) is placed in the path during the measurements; thanks to a rotating support it is able to cut off most of the beam power. The configuration is shown in Figure 3.6.

[5] From https://www.thorlabs.de/newgrouppage9.cfm?objectgroup_id=2946

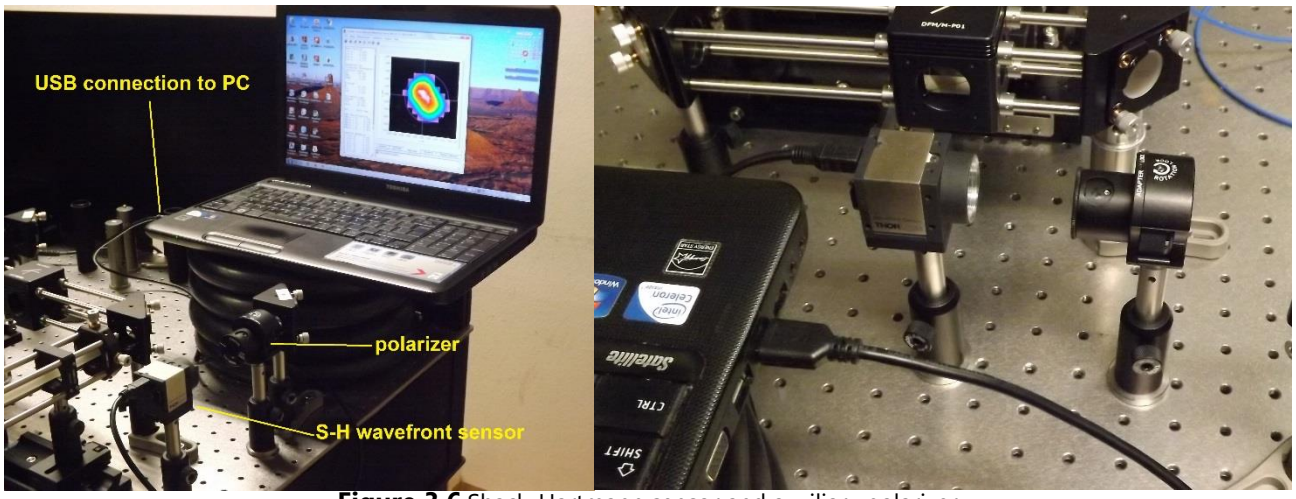

Figure 3.6 Shack-Hartmann sensor and auxiliary polarizer

3.6 EXTERNAL TRIGGERING OF THE ACQUISITION

The acquisition is managed by the user through the software *ThorImage* that controls the acquisition board (ATS9440, 14 bit, 4 channels, AlazarTech, Inc.). It normally works with a real-time sampling rate of 125 MHz, but it is provided with an external trigger input with software-selectable rate. Since the sources produce pulses at a rate of 80 MHz, the best sampling condition is achieved setting the board external trigger at 80 MHz rate. The external trigger signal is constructed extracting the SYNC-OUT signal from the pump and sending it to the circuit represented in Figure 3.7, realized by technicians of LaFSI laboratory, department of Physics and Astronomy Galileo Galilei, University of Padua. The SYNC_OUT signal is a square wave, while the acquisition board needs as input a sinusoidal wave. The phase retarder circuit is basically a double resonant circuit: it must extract the fundamental sinusoidal component from the square wave with a narrow frequency band and retard or anticipate it through a variable capacity. The simple resonant circuit produces a very narrow band selection, with a rapid rise and slope, presenting the risk of information losses. The best choice is to couple two simple resonant circuits with roughly the same resonance frequency (same components), to sufficiently enlarge the pass band. Each resonant circuit contains a coil split in two by the input signal connection; this makes them equivalent to an autotransformer: the output signal is proportional to the turns ratio, at present equal to 8 (4 turns/0.5 turns). The entire double resonant circuit will return a final output signal proportional to the square of this ratio, namely the gain factor is 64. The output signal phase can be changed modifying the variable capacity C_2 through a screw.

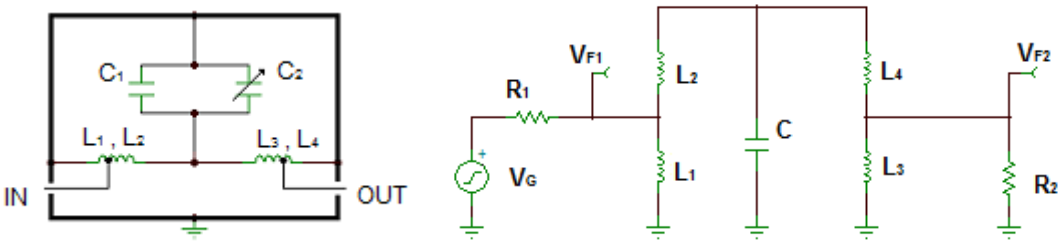

Figure 3.7 Schemes of the phase retarder circuit.

(a) Real compact configuration

(b) Extended scheme. C (from 37 pF to 87 pF) is the equivalent capacity of C_1 and C_2 parallel.

4 RESULTS

4.1 OPTIMIZATION OF POCKELS CELL TRANSMITTANCE VS WAVELENGTH

The alignment and the optimization of Pockels cell transmittance are performed for both devices, the one for the pump beam and the one for the OPO beam, following the procedures described in section 3.1. For the cell that controls the pump beam, the DC power bias $V_{DC,min}$ remains constant at (-108 $\pm$ 1) V over the entire range of wavelengths (700-900 nm), whereas $V_{AC,max}$ exhibits a linear trend (Figure 4.1):

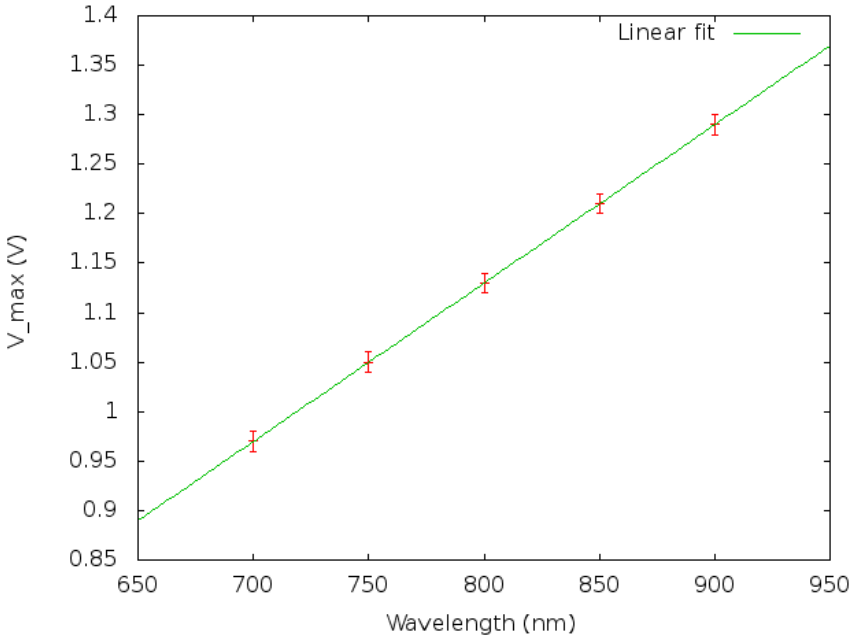

Figure 4.1 Linear regression for the maximum value of AC voltage applied to the pump Pockels cell

The resulting parameters of linear regression y = ax + b are:

a = (1.60 $\pm$ 0.02) mV/nm
b = (- 0.150 $\pm$ 0.003) V

For the cell that controls the OPO beam, DC power bias $V_{min,DC}$ increases with parabolic trend (Figure 4.2) $y = ax^2 + bx + c$ for growing wavelength (from 1200 to 1500 nm):

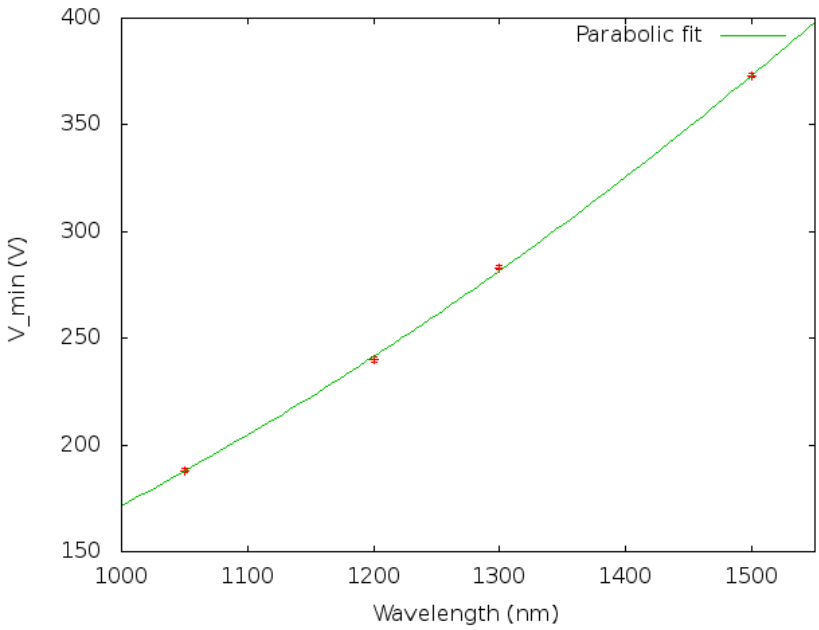

Figure 4.2 Parabolic regression for the minimum value of DC voltage applied to the OPO Pockels cell

a = (0.00018 $\pm$ 0.00004) V/nm^2
b = (- 0.0 $\pm$ 0.1) V/nm
c = (38 $\pm$ 66) V

Also $V_{max,AC}$ curve is a parabola:

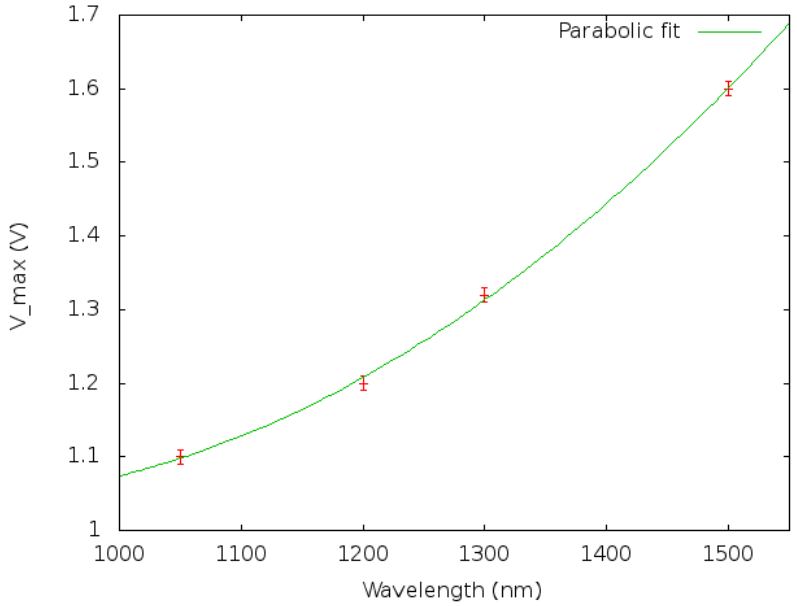

Figure 4.3 Parabolic regression for the maximum value of AC voltage applied to the OPO Pockels cell

$a = (1.3 \pm 0.2) \cdot 10^{-6}\ V/nm^2$
$b = (-0.0022 \pm 0.0006)\ V/nm$
$c = (2.0 \pm 0.4)\ V$

The previous curves are fundamental for every future use of the setup: before starting an experiment at certain wavelengths, the user must set the right DC and AC alimentation values, respectively on the Pockels cells supply consoles and on *ThorImage* software.

The maximum transmission of the Pockels cell is obtained when $V_{DC,min}$ and $V_{AC,max}$ are the supply values and the power modulation control of the beam is set on 100% in *ThorImage* software. Both Pockels cells transmittance was estimated at different values of beam wavelenght in the optimal conditions described above; the beam power was measured by means of the power meter before and after the device, for each wavelength. The transmittance is defined as the ratio between the output and the input power. The produced graphs are shown in Figure 4.4.

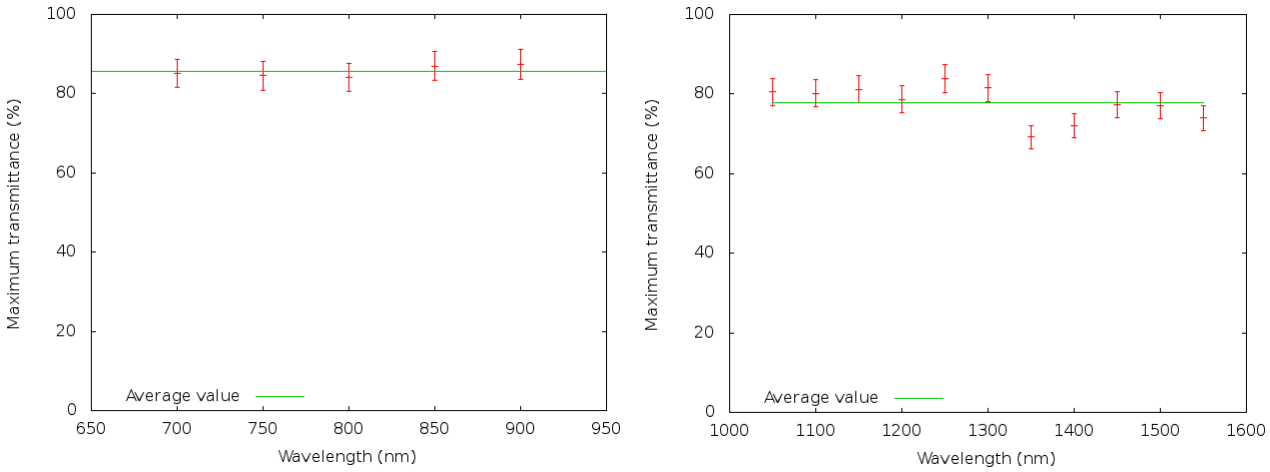

Figure 4.4 Percentage transmittance of Pockels cells for pump beam (left) and OPO beam (right)

The average values of maximum transmittance over the entire wavelength range are

Pump beam Pockels cell	OPO beam Pockels cell
86 ± 1 %	78 ± 4 %

4.2 PUMP BEAM ANALYSIS

The pump beam wavefront was monitored through Shack-Hartmann sensor along all its pathway on the optical bench (~ 3.5 m) to ensure there were no shape deformation. In fact, the pump beam encounters in its travel many optical elements that could introduce wavefront distortions, which must be carefully avoided in order to guarantee good wavefront modulation by the phase mask for STED nanoscopy. The position within the beam path is measured as the distance at which the S-H sensor is placed from the Pockels cell exit. In the first measurements some shape deformations were pointed out, as can be seen in Figure 4.5a. The wavefront never looked radially symmetric and the deformation became more and more serious while distancing from the Pockels cell. Therefore, the reason was identified in the Pockels cell alignment, which was repeated again. After this intervention the problem was solved, as shown in Figure 4.5b.

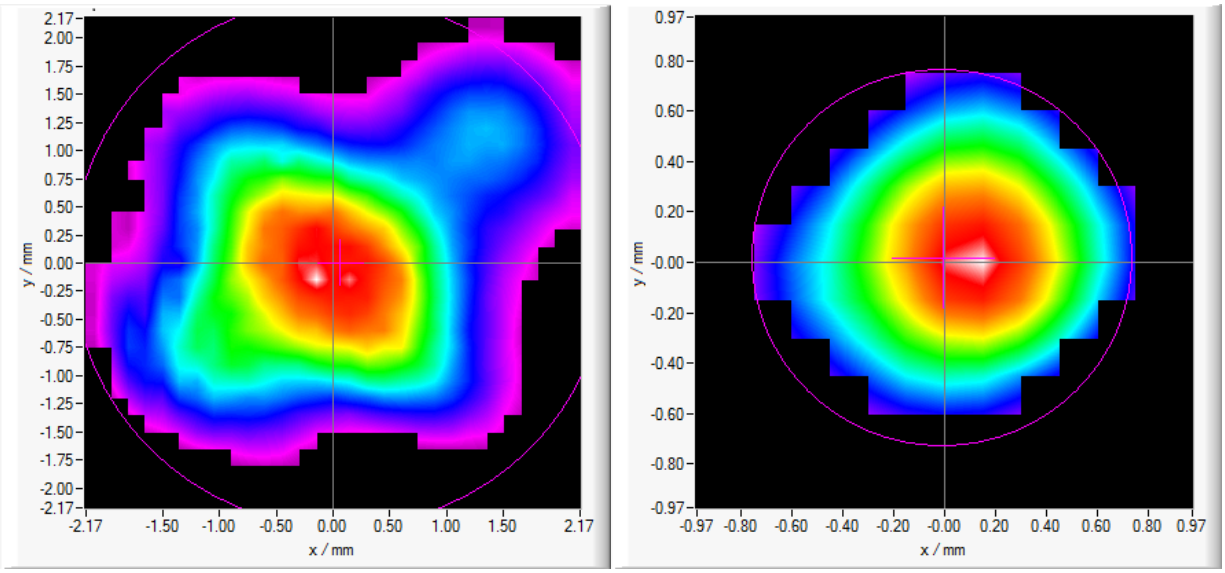

Figure 4.5 Pump beam wavefront measurements with S-H at distance 105.5 cm (after variable delay line)
(a) before Pockels cell realignment (b) after Pockes cell realignment

Shack-Hartmann sensor provides the instantaneous measurement of beam diameter in x and y directions. The detector was placed ta some distances along the beam path and for each of them, repeated measurements of x and y beam diameters were performed. The values obtained for x and y directions were averaged to get a beam diameter estimation at different positions. The beam width $w(z)$ (radius) of the Gaussian beam is a function of the distance z along the beam optic axis according to the expression

$$w(z) = w_0\sqrt{1+\left(\frac{z}{z_R}\right)^2},$$

where w_0, called "waist radius", is the minimum value of the beam radius and z_R, named "Rayleigh range", equal to the distance along the z axis from waist position at which $w(z) = \sqrt{2}w_0$ (see Saleh and Teich (36)). On this basis, the average diameter values were squared, plotted in a graph and fitted by the curve $f(z) = a + b(z-c)^2$ (Figure 4.6). In this way the following correspondence is established:

$$w_0 = \frac{\sqrt{a}}{2}, \qquad z_R = \frac{2w_0}{\sqrt{b}}.$$

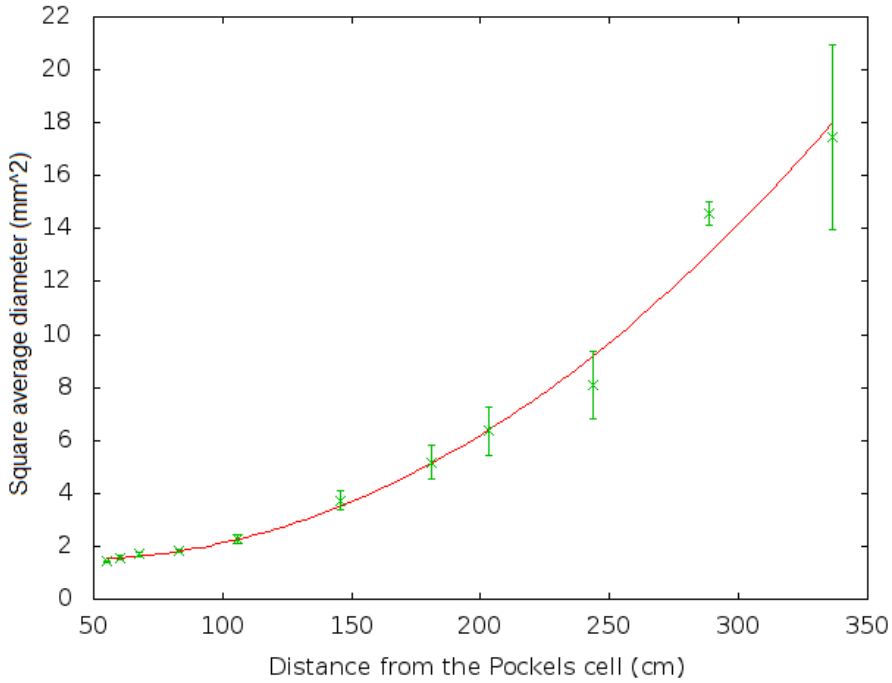

Figure 4.6 Square average pump beam diameter as a function of distance along the optic axis

The resulting parameters are:

a = (1.5 ± 0.5) mm^2
b = (1.9 ± 0.3) mm^2
c = (43 ± 229 cm

Consequently, the parameters which characterize the pump Gaussian beam are computed

$$w_0 = 0.61 \pm 0.09 \text{ mm}$$

$$z_R = 89 \pm 13 \text{ cm}$$

4.3 SYNCHRONIZATION OF THE ACQUISITION

An important goal in the setup optimization is the maximization of the acquired fluorescence signal. Since the sources produce pulses at a rate of 80 MHz, the best sampling condition is achieved setting the board external trigger at 80 MHz rate. In this way sample excitation and acquisition occur at the same frequency. Since the fluorescence emission has a decreasing exponential trend as a function of time, the optimal situation would be triggering the acquisition in correspondence to the emission maximum, as represented in Figure 4.7. Since the absorption and emission times are fluorophore-dependent, the fluorescence signal maximization through optimal triggering can be realized one fluorophore at a time. The synchronization of the acquisition is a technical strategy that allows the optimization of imaging result, especially when the excitation or emission conditions of a specific fluorophore are disadvantageous.

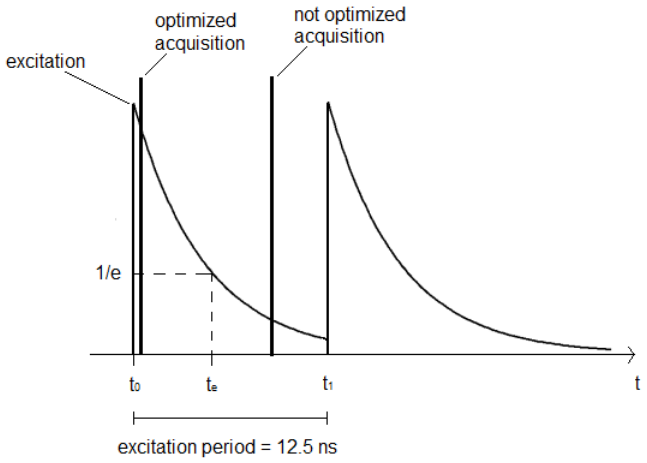

Figure 4.7 Scheme of the synchronization between signal emission and acquisition

The emission starting instant is *a priori* unknown; it is only possible to monitor the pump signal at the oscilloscope from the SYNC-OUT output. Nevertheless, the pulse produced in the pump source travels along all the path on the optical bench, then is focused through the objective on the specimen and finally it excites the fluorophores. The time of excitation (very fast, in the order of 10^{-15} s) and consequent spontaneous fluorescence emission (characteristic time 10^{-9} s) is different from what we are able to measure directly. The only way to identify the excitation instant is introducing a delay in the pump output signal through the circuit described in section 3.4, then sending it to the acquisition board in external trigger and consequently measuring the variation of the acquired signal.

The acquisition synchronization experiment is performed monitoring the fluorescence signal of a fixed sample, some mouse kidney cells on a slide (Fluocells, see section 2.4). Only one fluorophore excitation is sufficient to analyze the fluorescence signal maximization. Fluocells are illuminated by the OPO beam at wavelenght of 1100 nm, to produce 2PE of Alexa Fluor 568. The detection is in channel D (red). The sample and the excited fluorophore have been chosen in particular for the lifetime. In fact, the pulses period is 12.5 ns because the generation frequency is 80 MHz, thus the range of possible phase shift between the pump signal and the external trigger signal lays between 0 and 12.5 ns. In this period the fluorescence variation must be significant, namely the lifetime must be at least shorter than 12.5 ns. The delay between the retarded external trigger signal and the pump SYNC_OUT signal is measured at the oscilloscope to evaluate the introduced phase shift. The double resonant circuit output is connected also to the acquisition board to trigger effectively the sampling, as shown in Figure 4.8. The variable capacity is able to introduce a delay between pump and external trigger signals with a maximum excursion of about 4 ns in a certain configuration of cables. Hence, more cables configurations are required to explore all the 12.5 ns period, considering that a 1 m cable introduces a delay of 5 ns in the signal phase.

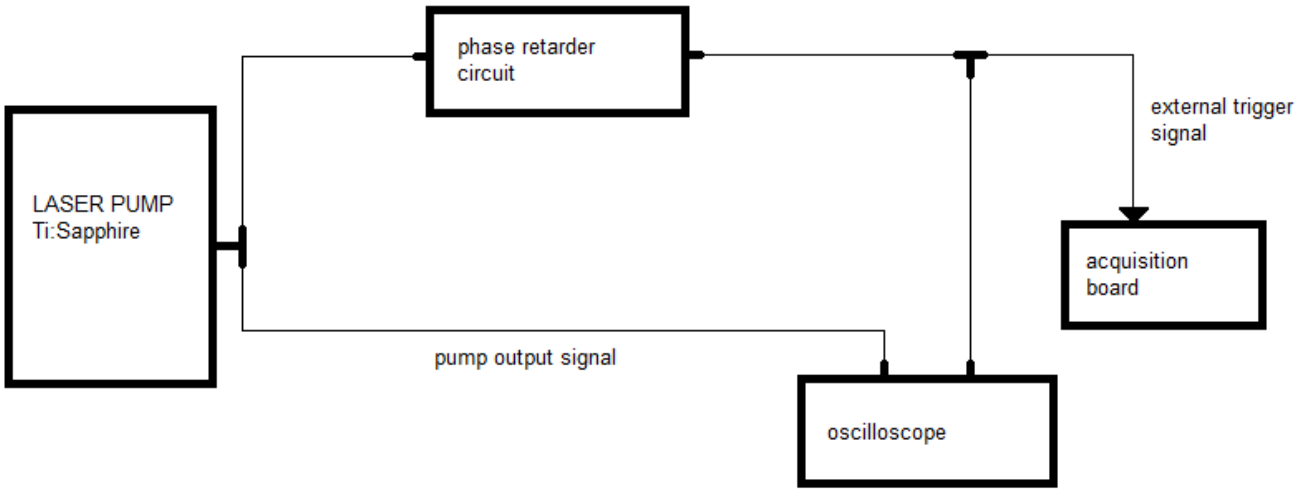

Figure 4.8 Cable configuration for the measurement of the introduced phase shit

For every measurement the signals delay configuration is set acting on the circuit variable capacity by means of the screw and a region of the specimen is fixed and focused for the observation. Primarily, a first image with the board set in internal trigger (125 MHz) is acquired as a reference. Thereafter, the sampling trigger is converted into external and one image is captured every 90 seconds during an interval of thirty minutes. Every image is acquired in gray scale, 16 bit, with the same magnification, as an average of 30 frames in order to minimize the

background signal. At the same time, the delay is monitored at the oscilloscope to characterize the circuit stability in time in that specific configuration and check the absence of a phase drift. The procedure is repeated for each signals delay configuration; every time the observed specimen region is changed to avoid signal losses caused by fluorophore bleaching. This is allowed because the meaningful data obtained thanks to this procedure are the ratios between external and internal trigger signals and not the absolute values. In this way the measurements can be divided into more measuring sessions.

The fluorescence signals analysis is performed through the software *ImageJ*, through which the average gray value within a selected region of interest (ROI) of an image can be measured. The values of internal trigger and external trigger signals are measured with exactly the same ROI, as shown in Figure 4.10. The external trigger image used for this analysis is the first acquired in the time series, so that the two compared images were captured one immediately after the other. This choice permits to avoid the introduction of random errors due to unintentional defocus of the specimen, system mechanical drifts or sources power fluctuations, which would alter the experimental imaging conditions between the two measurements. The delay is estimated as the average of repeated measurements at the oscilloscope (Figure 4.9). As an example, in Figure 4.10 we display two images of the specimen acquired in internal and external trigger in the delay configuration $\Delta t_{\mathrm{pulses}} = (0.654 \pm 0.006)$ ns. The background subtraction was performed by subtracting from fluorescence signals the average background value measured *a posteriori* in *ImageJ* thanks to other ROIs.

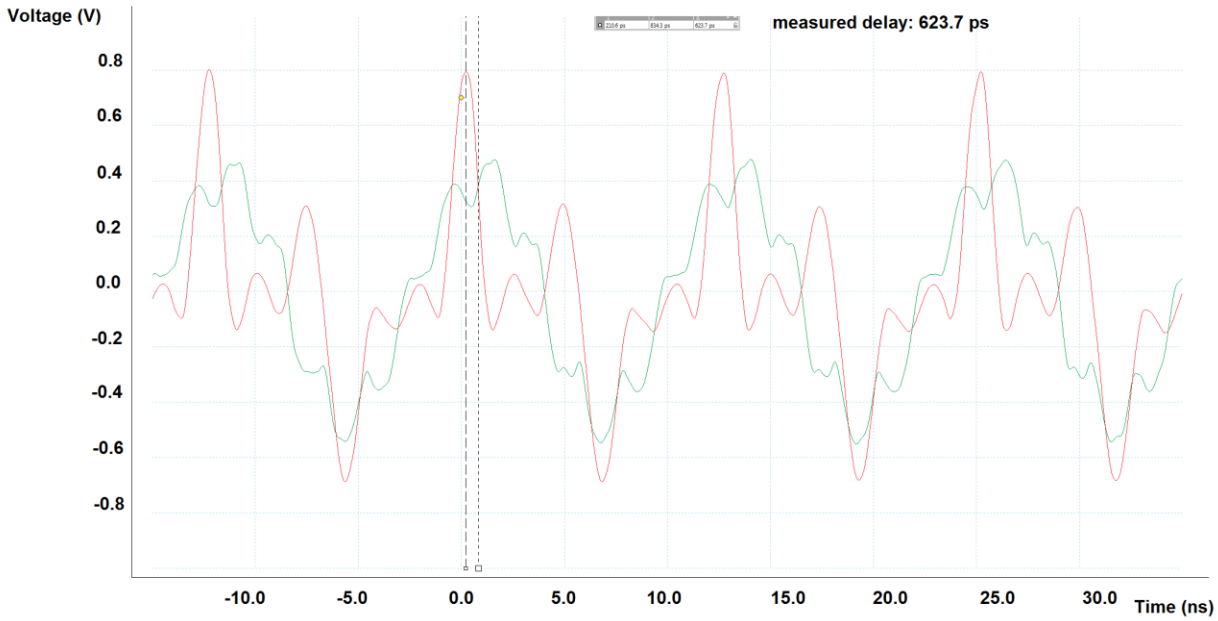

Figure 4.9 Measurement of the delay between pump (red) and external trigger (green) signals at the oscilloscope

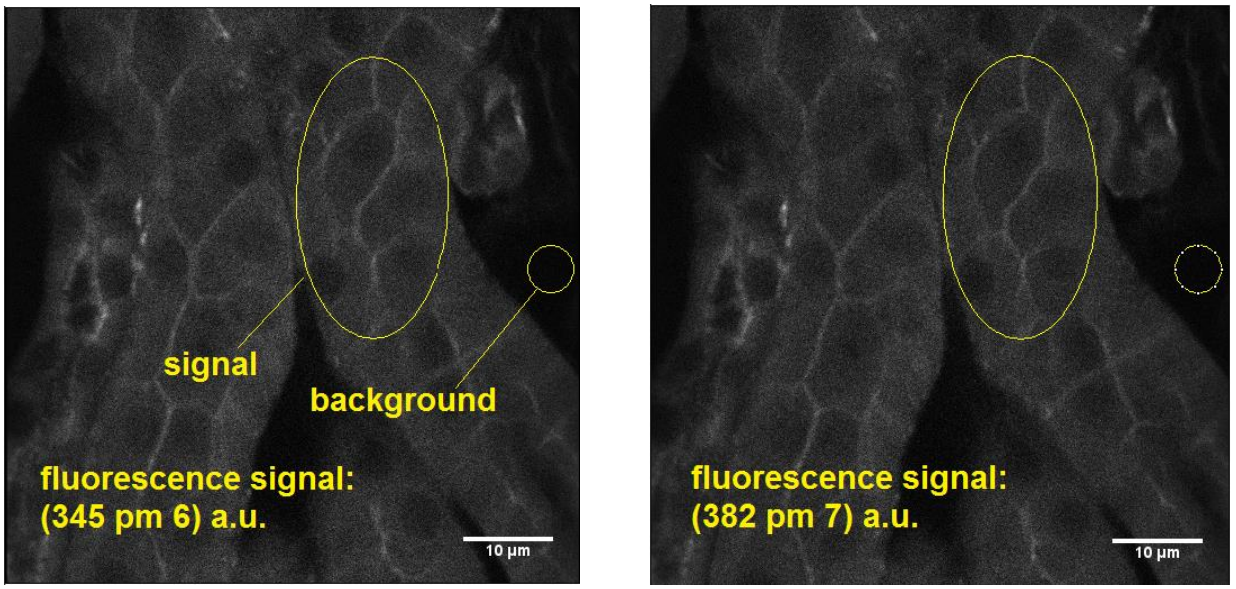

Figure 4.10 Fluocells fluorescence signal at 0.6 ns delay configuration
(a) Internal trigger image (b) external trigger image

The ratios between external and internal trigger fluorescence signals can be plotted in a graph as a function of delay. These experimental data were divided into increasing and the decreasing subsets, which were fitted with two exponential functions. The results are shown in Figure 4.11.

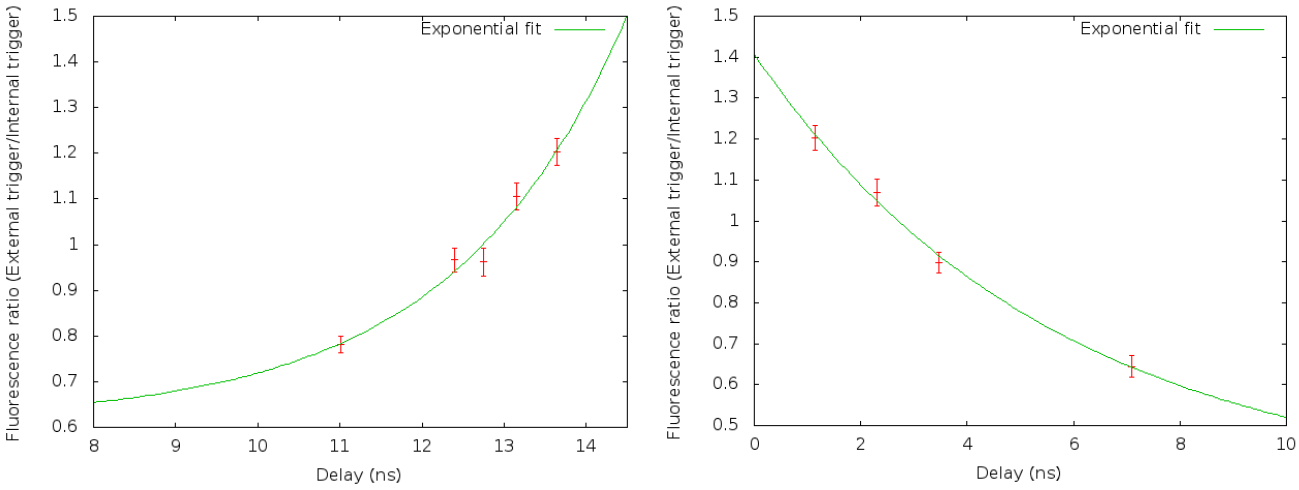

Figure 4.11 Increasing and decreasing data subsets

The fitting parameters are:

$f(x) = a + be^{cx}$
$a = 0.7 \pm 0.2$
$b = (0.3 \pm 1.2) \cdot 10^{-3}$
$c = 0.6 \pm 0.3\ ns^{-1}$

$g(x) = d + fe^{-gx}$
$a = -0.3 \pm 0.2$
$b = 1.1 \pm 0.2$
$c = 0.18 \pm 0.08\ ns^{-1}$

The increasing exponential function is shifted for 12.5 ns on the x axis to find out the intersection point which corresponds to maximum fluorescence signal acquisition of Alexa Fluor 568 emission. The curves intersection is shown in Figure 4.12. The intersection point is found computationally; the x coordinate represents the delay between pump output signal and external trigger signal that permits maximum signal acquisition, the y coordinate (averaged between the results of the two curves) is the signal enhancement gained with optimization of the acquisition.

$$x_{int} = (1.0 \pm 0.2)\ ns$$

$$y_{int}^{average} = 1.20 \pm 0.03$$

Therefore, if the optimal delay condition is set during external trigger sampling of Alexa Fluor 568 fluorescence emission, the percentage increment of signal $f_{ext}^{optimal}$ compared with the internal trigger signal f_{int} is

$$\frac{f_{ext}^{optimal} - f_{int}}{f_{int}} = (20 \pm 3)\ \%$$

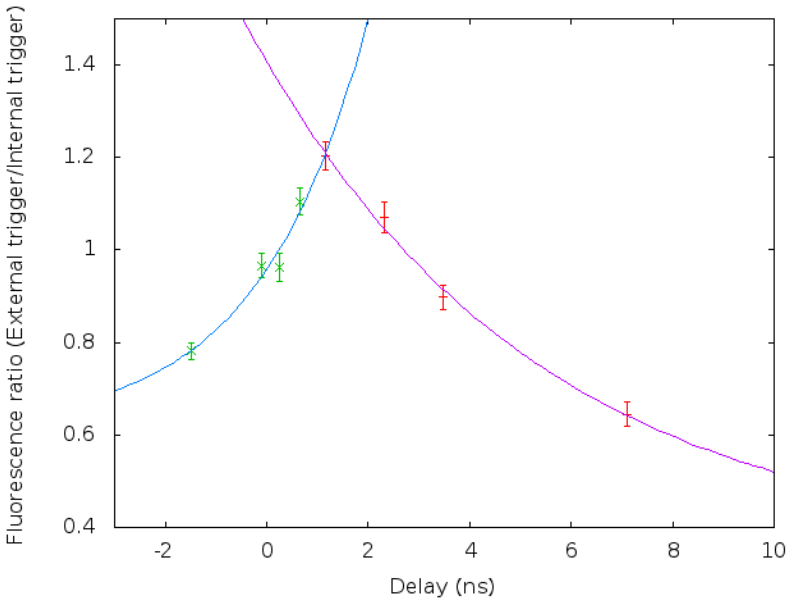

Figure 4.12 Research of the maximum acquisition delay for Alexa Fluor 568 emission

The optimal delay condition is *a priori* different for each fluorophore because each one has a characteristic absorption and emission time. The present study demonstrates that the synchronization of the acquisition yields to a significant fluorescence signal increase. The same experiment can be repeated for the most frequently used fluorophores in order to construct a lookup table of the delay configurations that enhance the acquired signal of a certain fluorophore, so that the user can refer to it before starting an experiment.

Characterization of the phase retarder circuit

The stability of the retarding circuit used to introduce the phase shift in the external trigger signal is analyzed. The goal is determining whether there is a phase drift or not and, if it is present, how much it affects the signal acquisition level. For all delay configurations, the values of delay and fluorescence signal were monitored in time for half an hour at least. Both delay and fluorescence signal are ideally supposed to be constant (even if fluorophore bleaching is expected), so the average values are computed. The residuals of the two data samples from the average values are plotted in percentage to be compared over time, in order to point out a possible correlation of fluorescence signal fluctuations to retarder circuit instability. For every

condition of phase delay, there are delay fluctuations around the average value, but they are much smaller than fluorescence signal variations during all the measurement time. In fact, while the standard deviation of delay sample is in the order of some percentage point, the standard deviation of fluorescence signal data is one order of magnitude greater. As an example, we exhibit the results for the delay configuration $\Delta t_{pulses} = (5.09 \pm 0.01)$ ns in Figure 4.13.

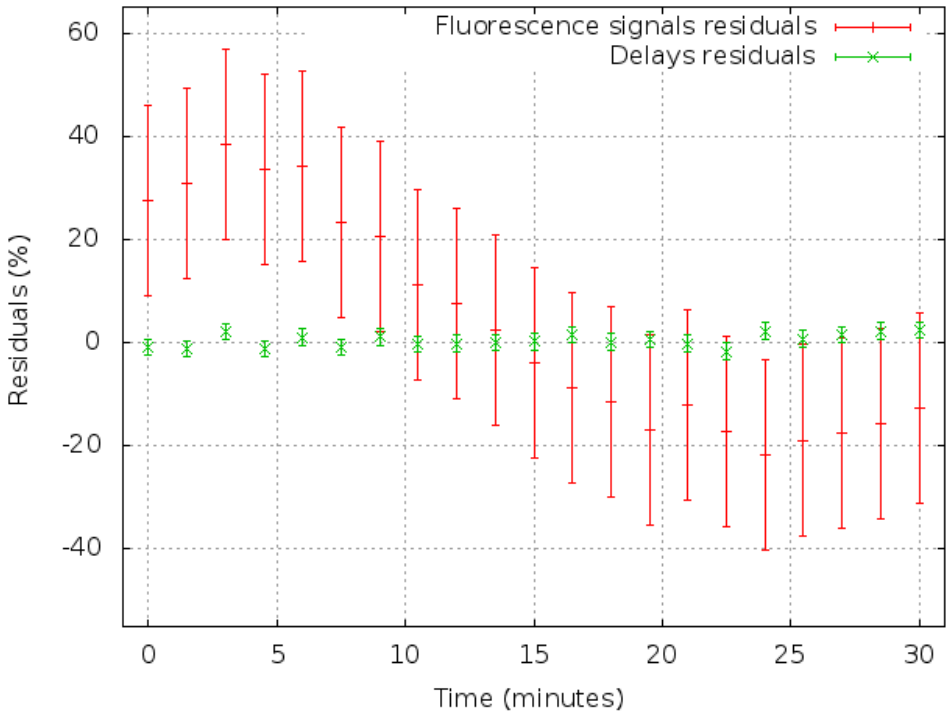

Figure 4.13 Percentage residuals around the average value of delay and fluorescence signal in time, Δt_{pulses} = 5.09 ns

Table 1

	Delay	Fluorescence signal
Average value	5.09 ± 0.01	326 ± 11
Standard deviation of the sample	0.082 ~ 1.6 %	60 ~ 18 %

Clearly delay fluctuations cannot explain the trend of fluorescence signal. This last is more reasonably due to fluorophore bleaching added to a probable focal plane mechanical instability. The measurements demonstrate that the device is robust, it does not present any drift in time, but only casual fluctuations which do not affect fluorescence signal acquisition.

4.4 CHARACTERIZATION OF TWO MULTIPHOTON MICROSCOPY OBJECTIVES

Two-beam multicolor multiphoton imaging technique, as well as STED nanoscopy, requires the use of objectives with high performance, especially in terms of achromaticity (correction of chromatic aberrations), great resolution, high transmittance, deep focusing, high signal-to-noise ratio. Two different objectives supposed to satisfy those requests have been tested in the laboratory, to find out which one presents the best features for our purpose. They are

- XL Plan N 25x, Olympus (25x, NA 1.05, water immersion),
- Apo LWD 25x, Nikon (25x, NA 1.1, water immersion).

The same tests are performed on both objectives, with the aim to compare them. They are described in the following list.

Achromaticity test

A fundamental requirement of both multicolor multiphoton microscopy and STED nanoscopy is the spatial overlap between the two beams 3D-PSF created by the objective on the sample. Consequently, the used objective must be highly corrected for chromatic aberrations.

The achromaticity test consists on recording some z-stacks of a single QD at maximum magnification (32x). A z-stack is a series of images collected at different planes, equally spaced in the z-direction with a fixed pitch. The movement of the microscope head along its axis and the acquisition are automatized. The aim is measuring the focus movement in the axial direction as a function of wavelength. It is not possible to get this information by repeating more consecutive z-stacks of the same QD and with the same starting and stopping positions, in fact it would takes much time during which a mechanical drift of the microscope head could occur. Furthermore, the measurements would be affected by an accumulated error derived from a mechanical imperfection on the head z-positioning at very small steps (usually from 200 nm to 500 nm to analyze a QD). Since for our purpose the maximum acceptable distance between the foci at different wavelengths is lower than 1 µm, very tiny mistakes can compromise the measure and affect the valuation of the objective achromaticity. The solution is to excite the sample alternately at two wavelengths at every z-plane and only after move to the next step. In this way two QD images series are produced with a single z-stack. All the images are acquired as an average of 30 frames to reduce background signal. Plotting the intensity z-profile of the two series with *ImageJ* sofware, the quantum dot axial PSF shape is measured. The meaningful information is given by the distance between the maximum of the two curves, namely the

distance between the foci of the same object imaged at different wavelengths. The smaller the distance Δz between the two, the better the chromatic aberration correction.

As an example, the z-profiles stemming from the z-stack for wavelengths couple 800 - 1200 nm is shown in Figure 4.14; data are fitted with Gaussian functions. In the Table 3 the measured differences between OPO beam focus and pump beam focus are displayed for each wavelengths couple and for both objectives. The smallest axial separation is highlighted for each wavelengths couple.

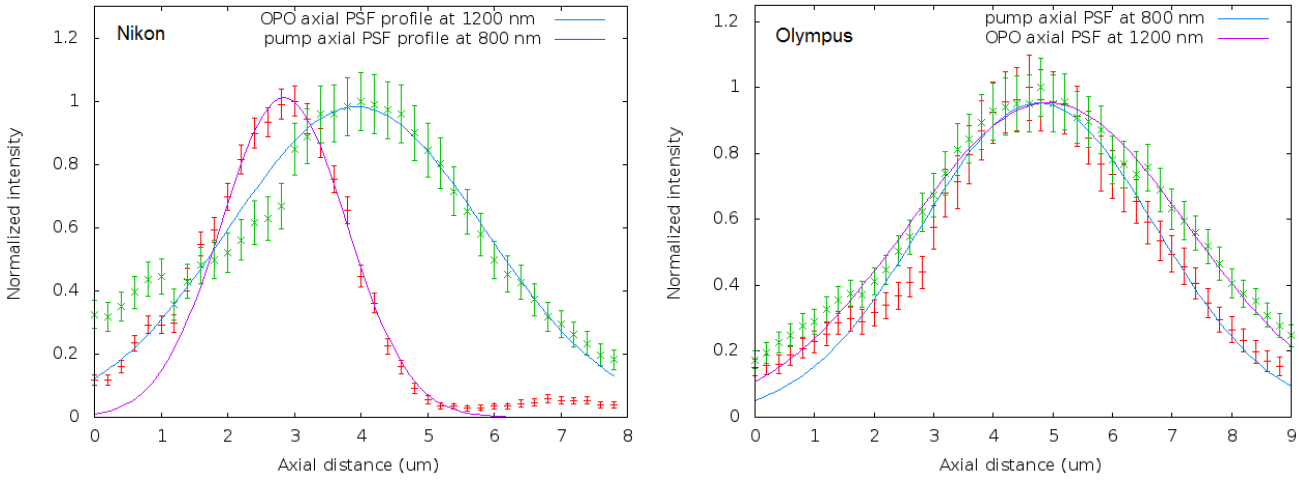

Figure 4.14 Axial distance between OPO and pump beam foci for Nikon (Left) and Olympus (Right) objectives

Table 2

Wavelengths couple	Difference with Nikon objective (μm)	Difference with Olympus objective (μm)
750 nm - 1075 nm	-1.0 ± 0.2	**0.3 ± 0.1**
800 nm – 1000 nm	-0.4 ± 0.2	**0.00 ± 0.02**
800 nm – 1075 nm	-0.6 ± 0.1	**0.2 ± 0.1**
800 nm – 1100 nm	-0.1 ± 0.2	**0.05 ± 0.07**
800 nm – 1200 nm	1.3 ± 0.2	**0.45 ± 0.09**
850 nm – 1100 nm	0.7 ± 0.1	**0.11 ± 0.05**

If we take the position of the focus at 800 nm as reference point (origin of the z-axis), it is possible to construct a graph that shows the variation of the axial position of focus as a function of wavelength. In fact, the distance between the focus at 750 or 850 nm and the origin is inferred knowing the distance of that focus and of the origin from another reference wavelength focus (for example 1000 nm, knowing the differences 750 nm – 1000 nm and 800 nm – 1000 nm). The result is illustrated in Figure 4.15 for both objectives.

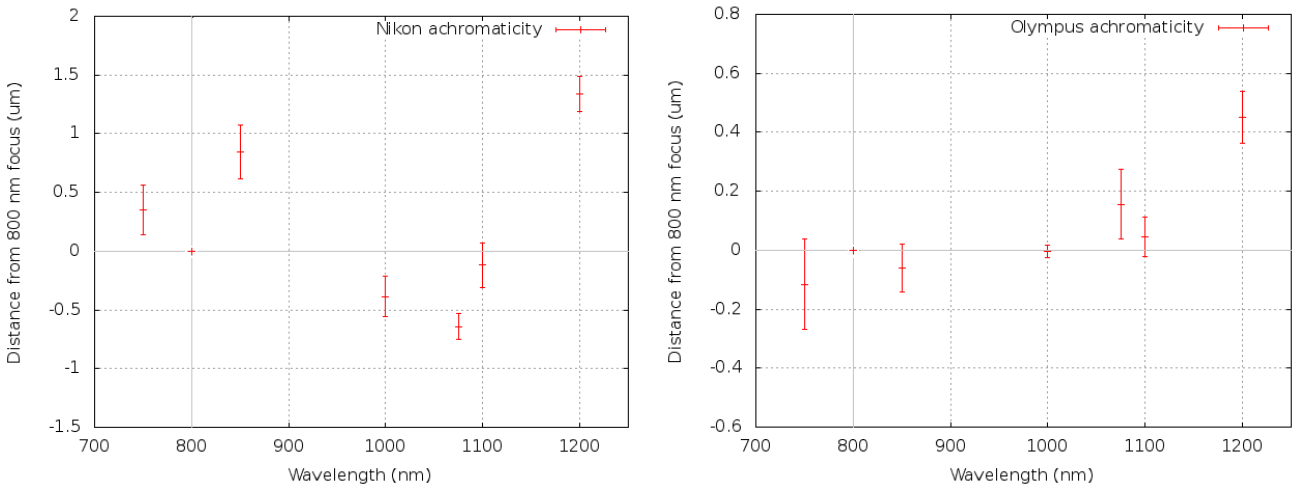

Figure 4.15 Valuation of Nikon (Left) and Olympus (Right) achromaticity

Furthermore, the width σ of z-intensity profile is an estimation of the axial PSF extent. In Figure 4.16 a comparison between the axial widths σ of the two objective PSF at different wavelengths is carried out.

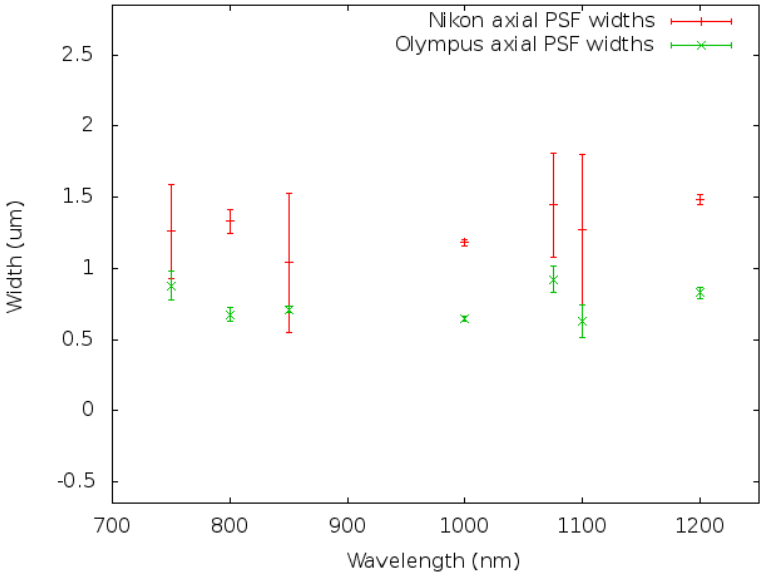

Figure 4.16 Axial width of the two objectives PSF

The axial PSF appears to be wider for the Nikon objective at every tested wavelength.

Lateral PSF size estimate

As concerns the lateral resolution of the microscope, it depends on the lateral extent of the PSF in focal plane of the objective. In terms of resolution, it is advantageous to choice the objective which leads to the smaller PSF extent. The measurement can be done on the objective PSF formed observing a single QD, which behave as a point source.

The image presenting the maximum intensity PSF (at the focal plane) of the z-stacks performed in achromaticity tests is extracted. For each of them, four intensity profiles along four different directions (vertical, horizontal and the two diagonals) of the quantum dot lateral PSF are plotted through the software *ImageJ*, thanks to four linear ROIs, as shown in Figure 4.17a. The four curves obtained in such a way are averaged. This final average profile is fitted with a Gaussian function to extract its width σ (as an example see Figure 4.19). The FWHM (FWHM = $2\sigma\sqrt{2\ln(2)}$) of the average profile corresponds to the average diameter of the objective lateral PSF at the focal plane.

Figure 4.17 PSF at the focal plane of Nikon objective

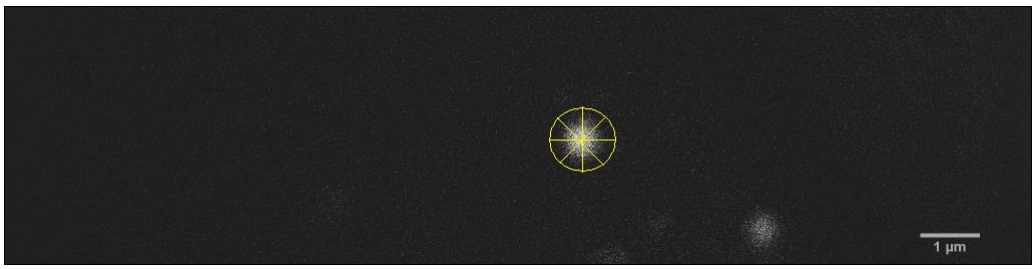

(a) pump beam illumination at wavelength 800 nm

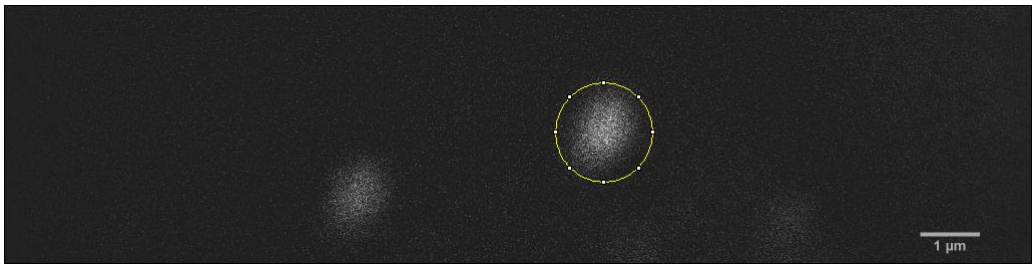

(b) OPO beam illumination at wavelength 1200 nm

Figure 4.18 PSF at the focal plane of Olympus objective

(a) pump beam illumination at wavelength 800 nm

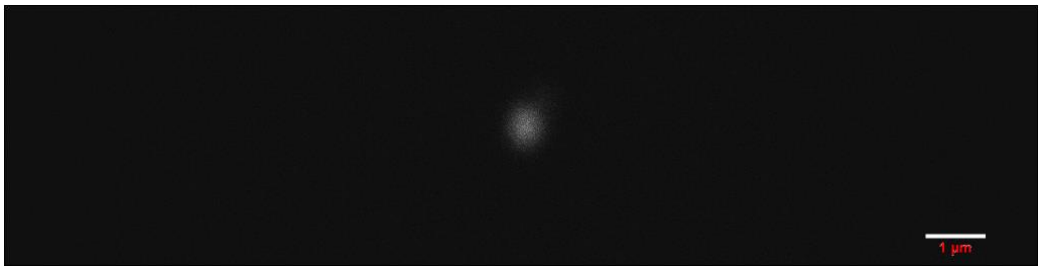

(b) OPO beam illumination at wavelength 1200 nm

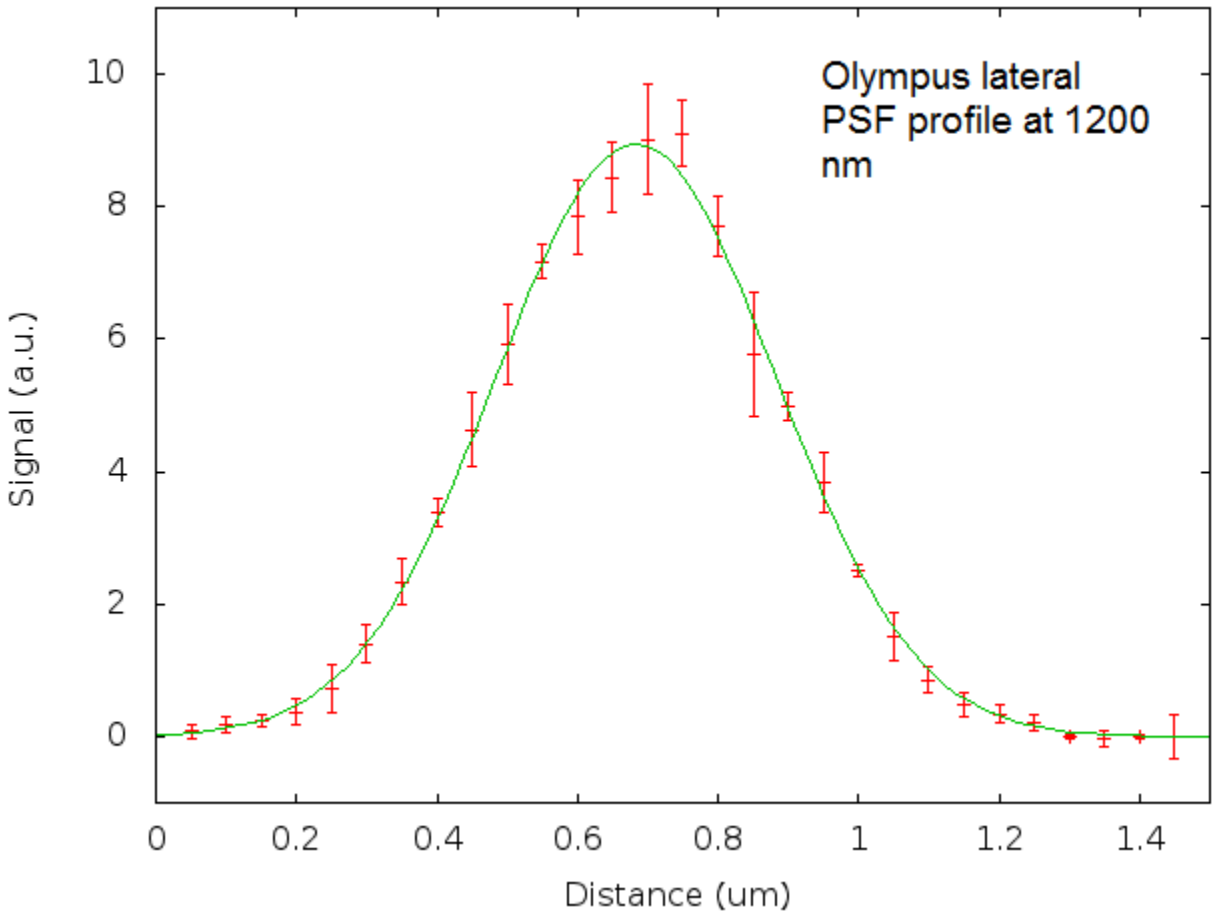

Figure 4.19 Gaussian fit of the average profile of Olympus lateral PSF at wavelength 800 nm

The analysis provides the results

Table 3

Wavelength (nm)	Nikon objective FWHM (μm)	Olympus objective FWHM (μm)
800	0.44 ± 0.03	0.44 ± 0.04
1200	0.8 ± 0.1	0.46 ± 0.05

Transmittance measurement

The imaging of thick biological specimen needs high powers at the focal plane; the beam during its travel on the optical bench wastes much power, therefore it is advantageous to avoid other losses at the objective as much as possible. The test is not a real objective transmittance

measurement, because in this case the beam power should be measured before the back aperture of the objective and at the focal plane. Instead, the incoming beam power can be measured only before the entrance in the periscope and below the focal plane because of the geometry of the thermal sensor aperture (recessed and tight in comparison to the objective head). However, it is possible to perform the same measurements for both objectives at the same experimental conditions, keeping in both cases the objective head at contact with the edges of the sensor aperture to be sure not to lose power outside. The results do not have meaning as absolute values, but can be compared to each other. In Figure 4.20 we display the relative difference between the objectives transmittance $\frac{T_{Nikon}-T_{Olympus}}{T_{Nikon}}$ as a function of wavelength. The wavelength ranges where one objective transmittance is higher than the other are highlighted.

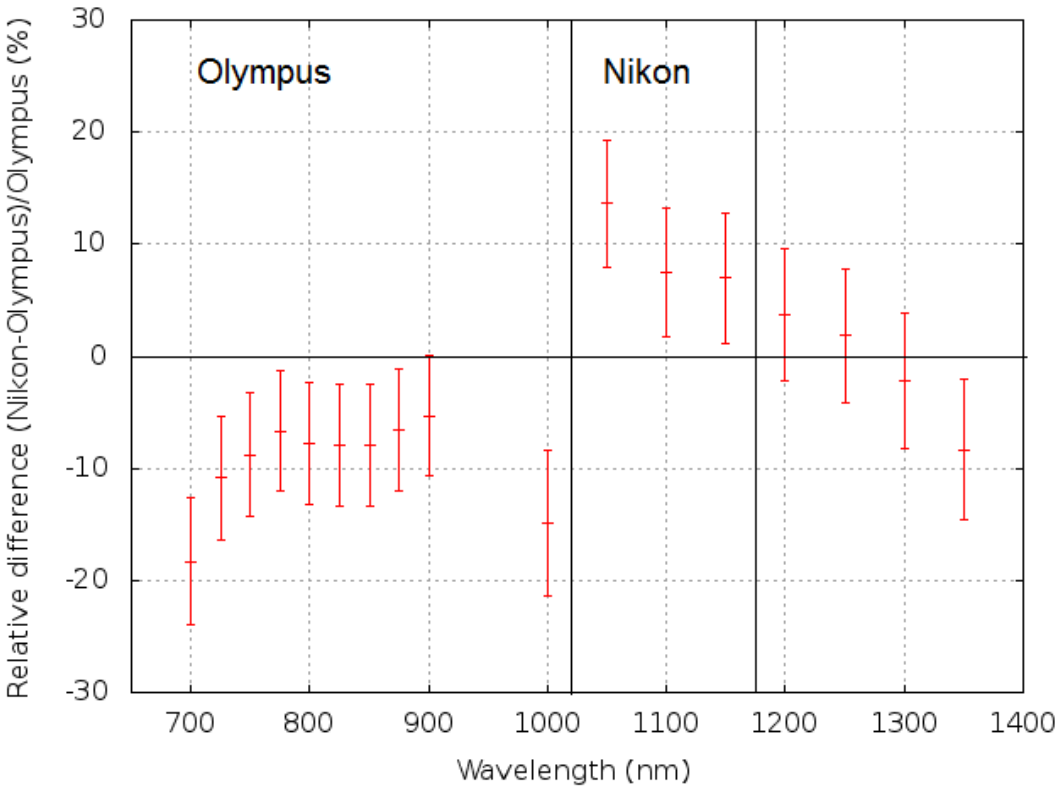

Figure 4.20 Relative difference between Nikon and Olympus transmittances

The results provide information about how good is one objective transmittance compare to the other. Olympus transmittance is about 10 % superior to the Nikon one in the range 700 – 1000 nm, while Nikon transmittance is about 9 % higher in the range 1025 – 1200 nm. At higher wavelengths the two are comparable.

4.5 TWO-BEAM MULTICOLOR MULTIPHOTON TEST

The test of the setup capability to perform two-beam multicolor imaging is carried out on a simple non fluorescent specimen to avoid the problems related to the biological samples (staining, fluorophore bleaching, imaging deeply…). It consists on a KDP powder prepared on a glass slide for the imaging under the microscope (see section 2.4). The illumination by OPO and pump beams produces second harmonic generation signals for both excitation wavelengths; if the two PSF are overlapped at submicrometric precision and a sufficient temporal synchronization between the pulses is achieved, the two beams undergo to a mixing parametric process called sum-frequency generation, described in section 1.3.2. It raises with an intermediate wavelenght luminous emission. Since higher harmonic generation phenomena are not isotropic, but the light is emitted in the forward direction, the detected signal by a microscope in epi-fluorescence configuration is composed only by back scattered photons, with low detection efficiency, therefore the acquisition requires high PMT gains or high excitation powers.

First test

Starting from the coarse temporal alignment of the beams set at the oscilloscope as described in section 4.3, the position of the variable delay line is slightly changed acting on the coarse ferrule of the micrometric head, observing simultaneously the sample with acquisition in live modality. In the Tables 5 and 6 the illumination and detection settings are displayed.

Table 4 Illumination parameters

Beam	Wavelength	Pockels cell value
Pump beam	λ_1 = 880 nm	15 %
OPO beam	λ_2 = 1350 nm	27 %

Table 5 Detection parameters (all PMTs are acquiring simultaneously)

Signal	PMT Channel	PMT gain
Blue (SHG)	B	1
Red (SHG)	D	10
Green (SFG)	C	60

When both beams are incoming on the sample, SFG signal is expected to be detected on channel C (green), because $\lambda_{\mathrm{SFG}} = \frac{\lambda_1 \lambda_2}{\lambda_1 + \lambda_2} \sim 530$ nm. When the SFG green signal starts to be visible, it must be maximized through the coarse and fine ferrules of the differential micrometer. In the figures below the raising of SFG phenomenon is evident. Every image is acquired simultaneously by three PMTs, in blue, red and green channels, while the difference is the illumination condition. The first (Figure 4.21a) was captured with the only incoming OPO beam, which generates SHG of KDP crystals at a wavelength $\sim$ 675 nm (channel D, red). The second (Figure 4.21b) is acquired during pump beam illumination, which produces SHG at $\sim$ 440 nm (channel B, blue). Finally, the third (Figure 4.21c) exhibits SFG signal in channel C while both beams are incoming.

Figure 4.21 Two-beams multicolor imaging of KPD powder

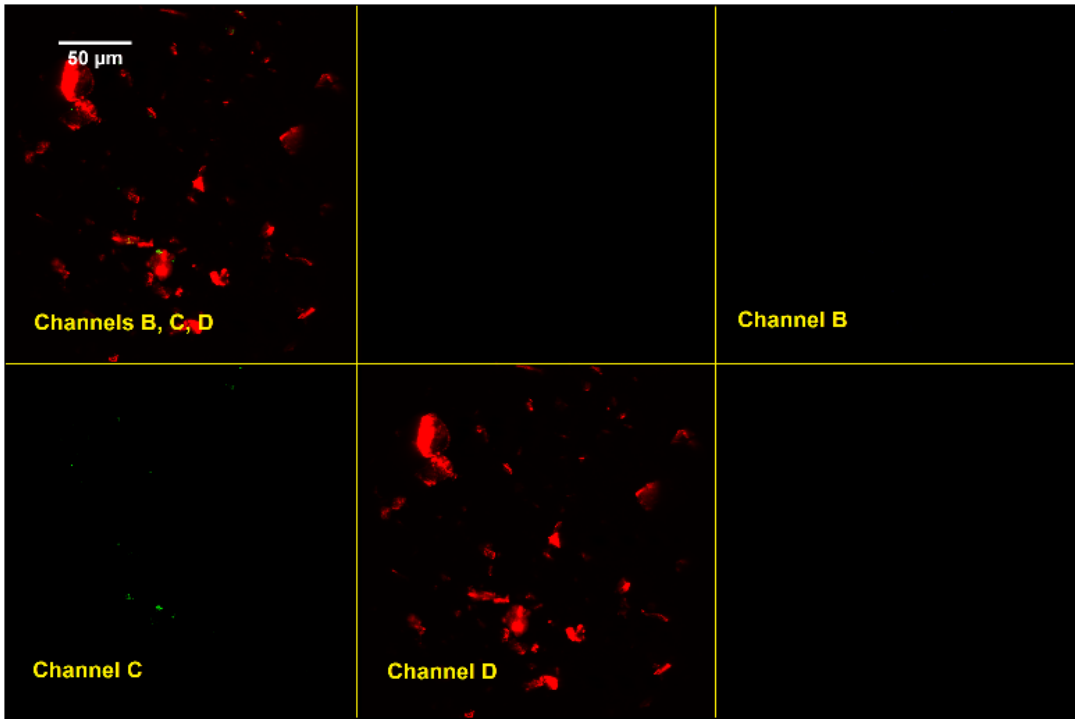

(a) OPO beam illumination at wavelength 1350 nm

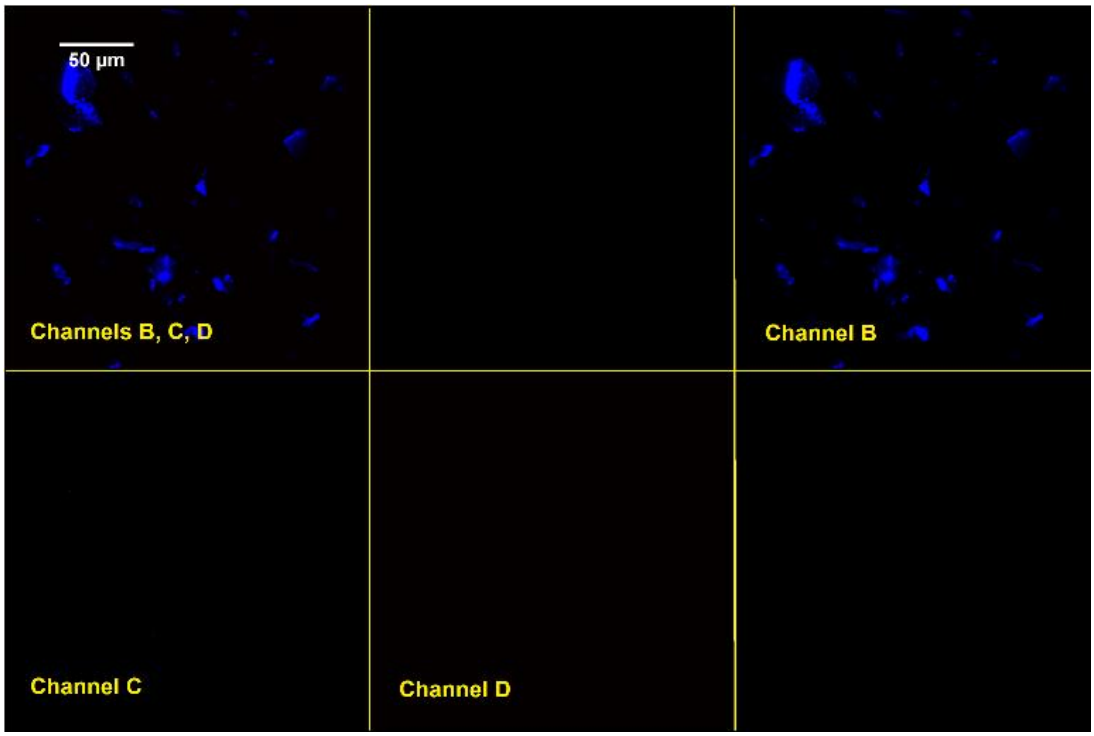

(b) pump beam illumination at wavelength 880 nm

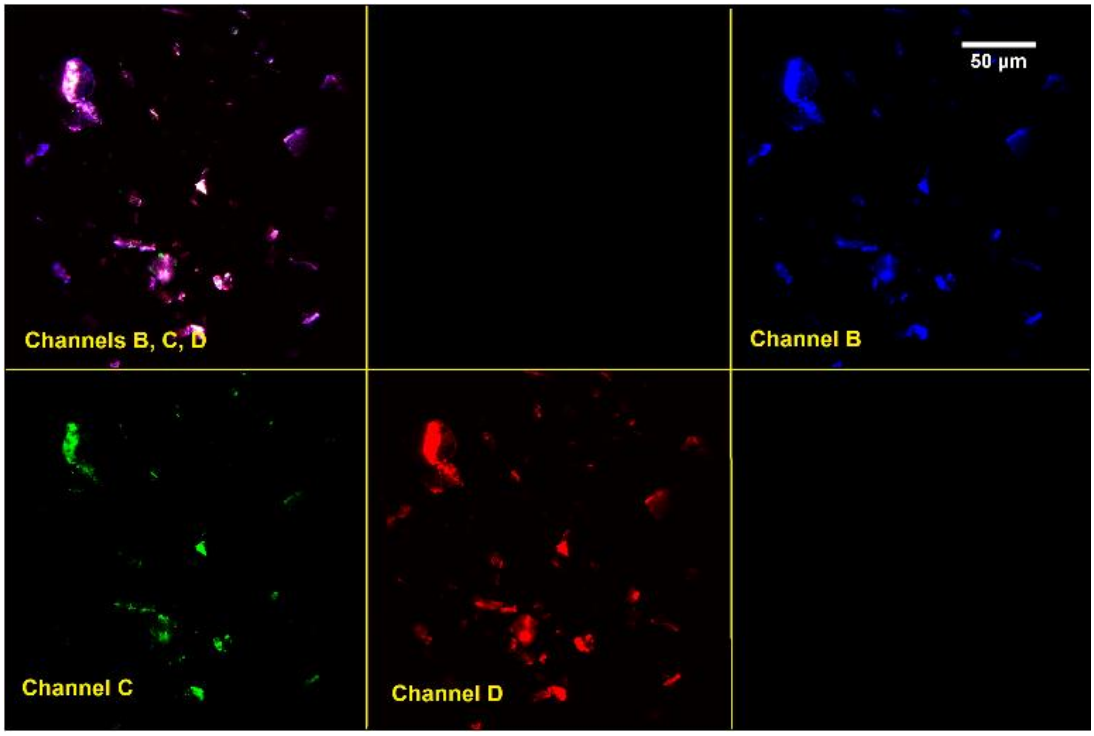

(c) both beams illumination

We can be sure that channel C signal corresponds to SFG phenomenon because it disappears when one of the beams is blocked. In fact, in Figures 4.22a and 4.22b there is no green signal in channel C, apart from low and localized background signal caused probably by luminescence of some dirt on the slide.

Second test

After the first result, the test was repeated with the same experimental conditions to better characterize the control on SFG phenomenon by varying the temporal superposition of the two pulses. The first time it is performed with the Nikon objective, the second time with the Olympus objective. Primarily, the best temporal synchronization condition is identified by moving the variable delay line and simultaneously monitoring the signal in channel C (a ROI is superimposed on the image with acquisition in live modality). The maximum signal position found in such a way for Nikon objective is set as the origin of the positions axis; with respect to it, one image is acquired moving the variable delay line back and forward with a 10 µm pitch (1 nick in the coarse graduation). The same zero position is maintained also for the second test with Olympus objective. All the images are acquired as an average of 20 frames to minimize

the background signal. The measurement of SFG signal is performed through ImageJ equally for all the images. A threshold is set in order to cut off the much frequent less luminous pixels belonging to the PMT background. Thereafter, the ROI 1 (Figure 4.22) is picked and the average value of the signal in the selected pixels is computed. Another background subtraction is performed by means of the ROI 2 placed in a dark region.

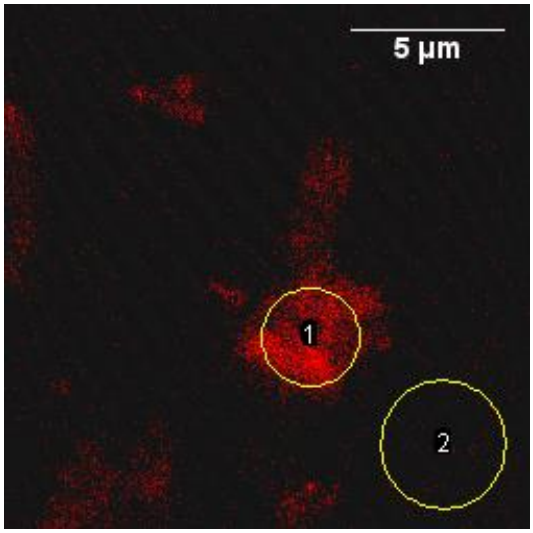

Figure 4.22 ROIs for the measurement of SFG signal over threshold

In Figure 4.23 a comparison between the images obtained with Nikon objective in conditions of synchronized beams and not synchronized beams is proposed. Two graphs of SFG signal as a function of the distance from the zero position are produced, one for Nikon and one for Olympus, and displayed in Figure 4.24. The data were fitted with Gaussian functions.

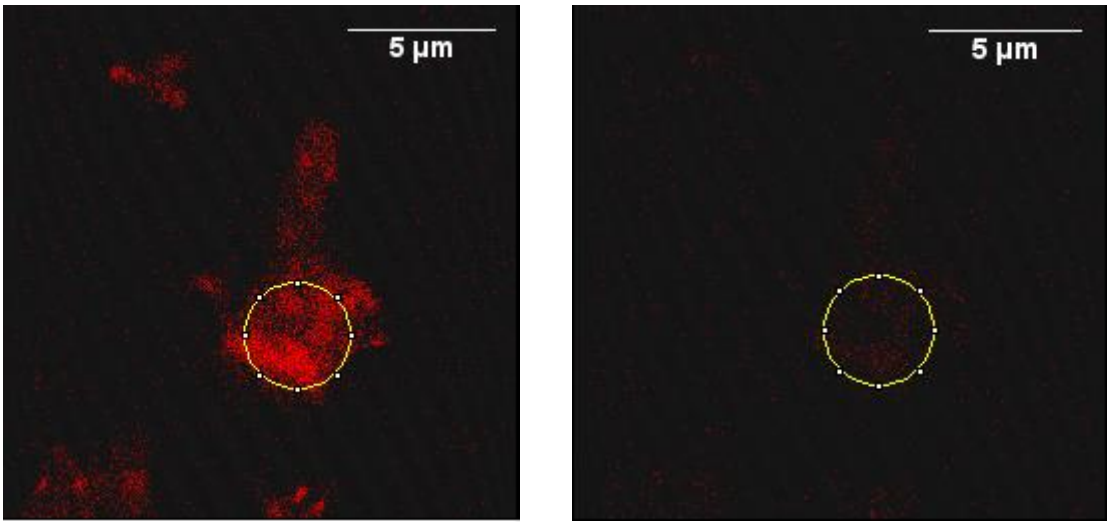

Figure 4.23 SFG signal from KDP powder with synchronized (0 µm) and not synchronized (-30 µm) pulses

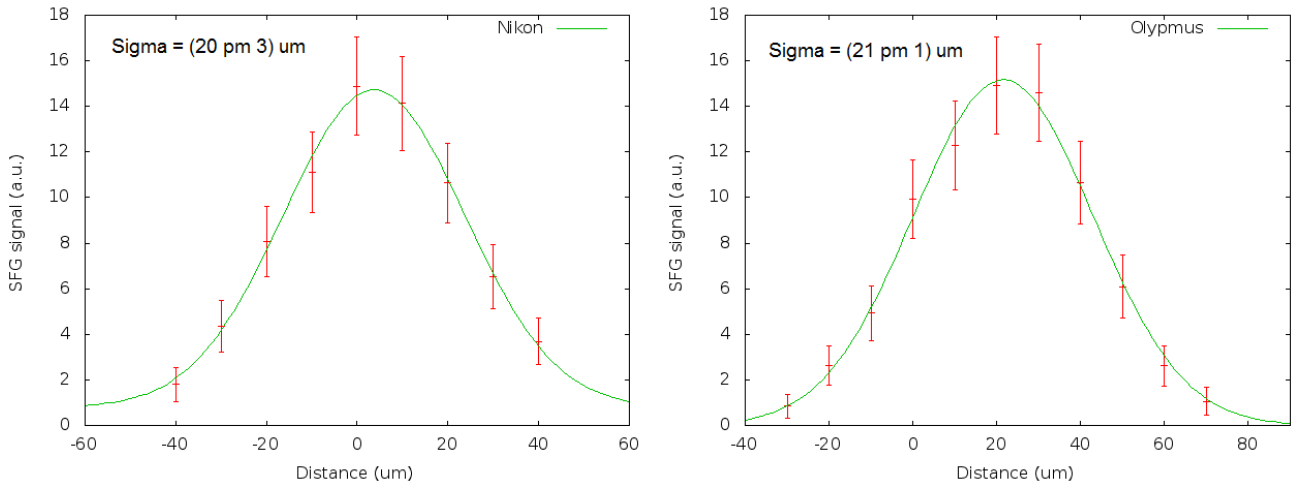

Figure 4.24 SFG signal as a function of variable delay line position for Nikon (Left) and Olympus (Right)

The estimation of $1/e^2$ width (namely 2σ) of the temporal intercorrelation function between the two pulses is for the two objectives:

Table 6

	Nikon	Olympus	Weighted average
Spatial width	40 ± 7 µm	43 ± 2 µm	43 ± 2 µm
Temporal width	133 ± 23 fs	143 ± 8 fs	142 ± 8 fs

Preliminary tests on fluorescent samples

The experiment is repeated with the fluorescent sample described in section 2.4. Similarly to what was done in the previous tests, some images were captured in channel C varying the variable delay line position with a pitch of 10 μm, with both beams illumination. The emission of two-color two-photon excited fluorophore is plotted in the graph displayed in Figure 4.25, after background subtraction. The curve represents the cross-correlation function between the two pulse trains as a function of space instead of time delay (related by light speed *c*).

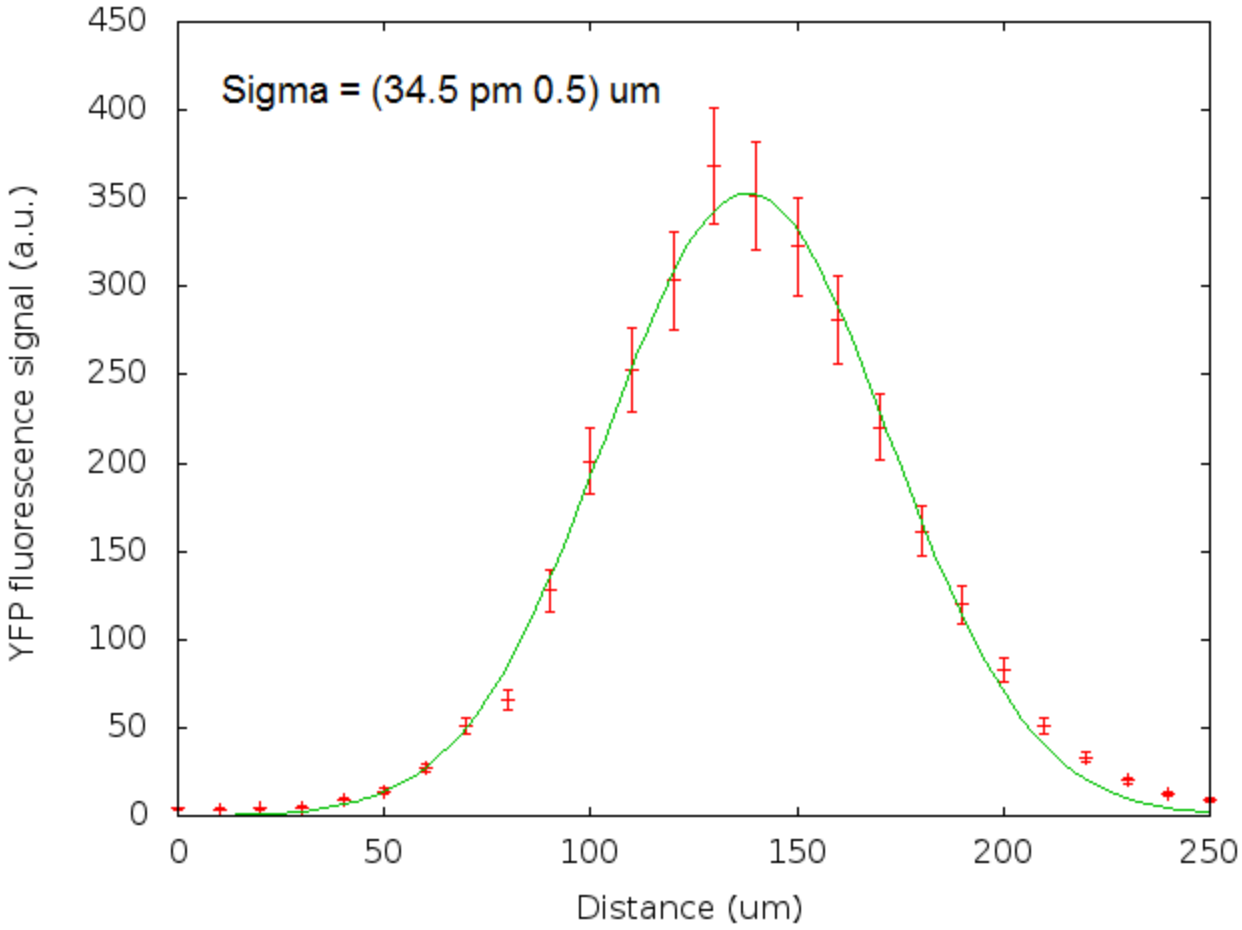

Figure 4.25 Fluorescence signal as a function of variable delay line position

The Gaussian fit $f(x) = ae^{-\frac{(x-b)^2}{2(\sigma_{int})^2}}$ provides the value of the curve width σ_{int} = (34.5 ± 0.5) μm. Hence, the estimation of the $1/e^2$ width of the temporal cross-correlation function between the two pulses (namely $2\sigma_{int}$) from the fluorescence curve is:

Spatial width	(69 ± 1) μm
Temporal width	(230 ± 4) fs

Since $\sigma_{int} = \sqrt{\sigma_{OPO}^2 + \sigma_{Ti:S}^2}$, the expected value for $2\sigma_{int}$ is $\sim \sqrt{140^2 + 200^2} = 244$ fs. The experimental result appears underestimated around 6 %, but we must consider that Coherent declares the typical values for the pulses $1/e^2$ width (140 fs for the pump and 200 fs for the OPO) without specifying uncertainties.

4.6 EFFICIENCY OF LASER LAUNCH INTO SINGLE MODE OPTICAL FIBER FOR STED NANOSCOPY

Beam injection was carefully performed by way of procedures described in section 3.2 for both cases. Once the beam-fiber coupling has been maximized as much as possible through the fiber launch alignment, the final efficiency is estimated. The powers in input to the fiber and at its exit are measured through the power meter while varying the beam power modulation (setting different percentage values on software *ThorImage*, section Power Control). Both for doublet and for ZEISS objective a graph input power/output power is plotted; the fiber coupling efficiency is extracted as the linear coefficient computed through data linear interpolation $f(x) = a + bx$ (Figure 4.26).

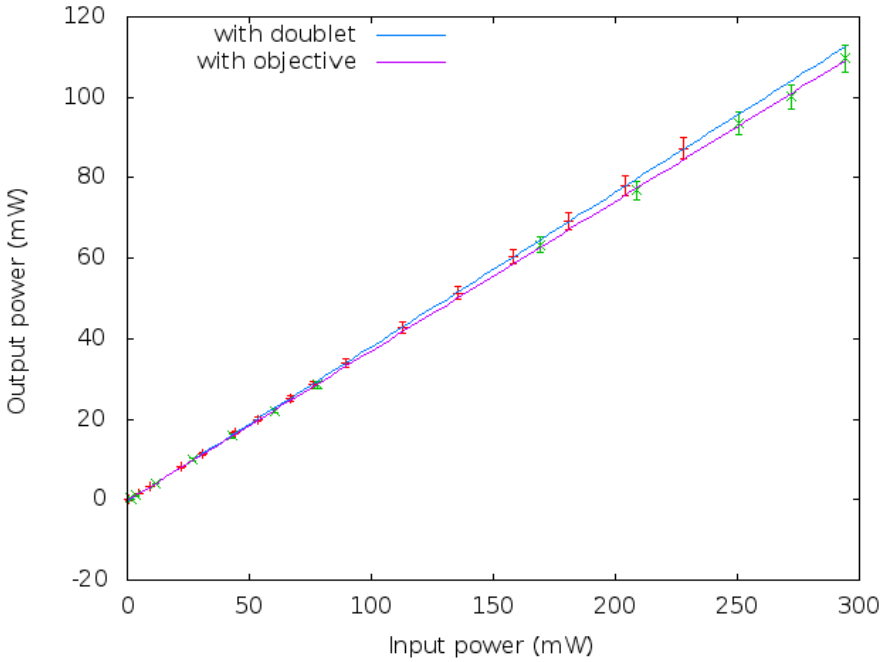

Figure 4.26 Fiber coupling efficiency

The parameter b corresponds to the fiber coupling percentage efficiency:

Doublet	Objective
0.3841 ± 0.0005	0.372 ± 0.001
(38.41 ± 0.05) %	(37.2 ± 0.1) %

The fiber coupling efficiency with the doublet results superior to the one with the objective of about 3 %.

4.7 MODULATION OF PUMP BEAM WAVEFRONT FOR STED NANOSCOPY

The modulation of pump beam wavefront is performed by a spiral phase mask placed after the exit of the optic fiber. The mask is mounted on a x-y stage for fine alignment of its center with the beam optic axis. The quality of the alignment is directly monitored by observing the beam wavefront at Shack-Hartmann sensor, after the passage through the phase plate and through a slightly converging telescope. The correct mask positioning yields to a wavefront shaped as a doughnut: in Figure 4.27 S-H output after optimization of the mask position is shown.

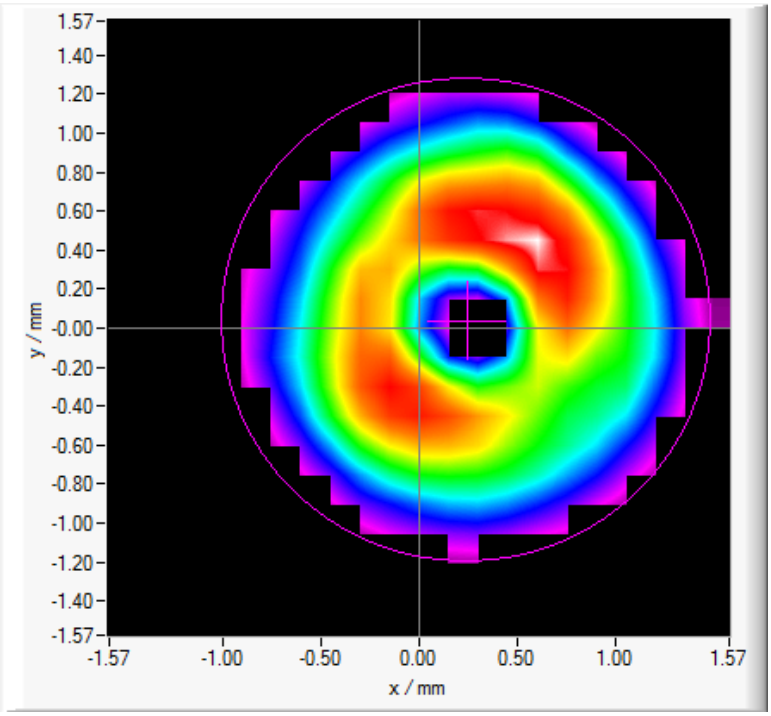

Figure 4.27 Doughnut-shaped pump beam wavefront

The entire beam diameter must enter in the objective back aperture to be focalized in the doughnut on the specimen. Since the mirrors in the microscope scan head quite expand the beam diameter, a telescope has been necessary to reduce it. The telescope was composed of two aspheric plano-convex doublets with focal lengths f_1 = 10 cm, f_2 = 3 cm. When the lenses are disposed as shown in Figure 4.28, the effect is a beam diameter reduction of a factor f_2/ f_1.

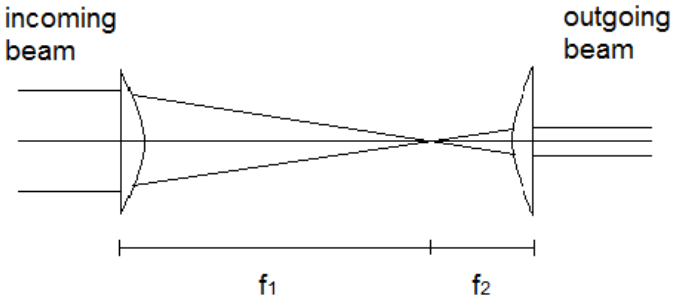

Figure 4.28 Configuration of the telescope for the beam diameter reduction

Thanks to this expedient, the beam was introduced into the objective and we were able to see a doughnut-shaped PSF observing a single quantum dot (Figure 4.29).

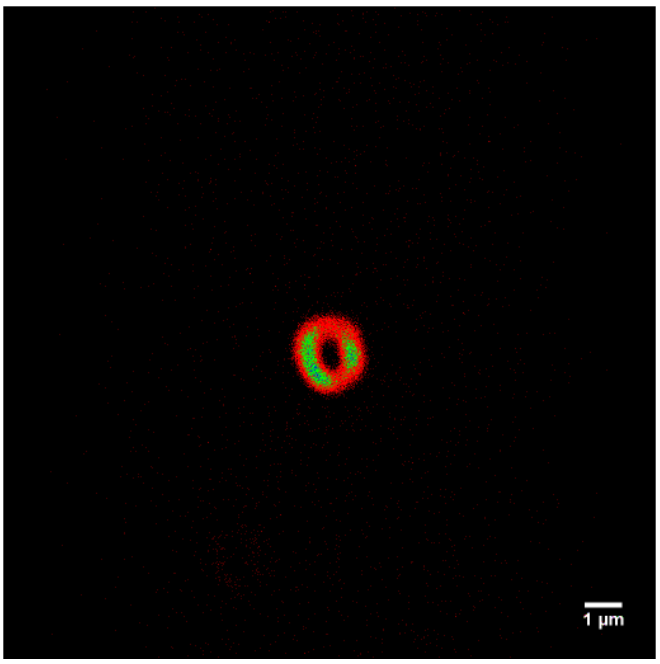

Figure 4.29 Doughnut-shaped PSF

4.8 DEPLETION TEST

The stimulated emission depletion effect is observed on Alexa Fluor 594 sample, described in section 2.4. The alignment of the optical fiber with respect to the pump beam optic axis was quite good at the moment of the test, in fact the beam-fiber coupling efficiency was around 30%. This condition allowed the beam power after the exit of the fiber to achieve the value of 78 ± 2 mW at 90% of maximum power provided by the Pockels cell. The objective available in the laboratory for this test was Nikon objective. The more efficient depletion effect is carried out when the depletion wavelength belongs to the tail of the fluorophore emission spectra; observing the emission spectra of Alexa Fluor 594 (Figure 2.20) a good choice can be 750 nm, while two-photon excitation is provided by the OPO beam at 1200 nm. In Nikon objective the axial distance between the foci at 750 nm and 1200 nm wavelengths is 1.0 ± 0.3 μm, according to the measurements of focal positions along the z-axis (Figure 4.15). To correct the objective chromatic aberration the telescope described in the previous section is exploited: by slightly increasing the distance between the two lenses with respect to the configuration depicted in Figure 4.31, a variable convergence is applied to the pump beam after the fiber exit. The distance between the doublets which makes the OPO and pump beams PSF overlap in axial direction is set moving one of the lenses through a micrometer head and simultaneously observing a single QD. As concerns temporal conditions, starting from the coarse synchronization condition set at the oscilloscope, the two pulses must have a delay inferior to one hundred of picoseconds between each other. To finely achieve this condition the oscilloscope is no more useful, therefore SFG process observed on KDP crystal is exploited to investigate the temporal difference between the pulses. The procedure is analogous to the one described in section 4.5 for the research of the maximum SFG signal, but now the setup is set in STED configuration (Figure 2.2). Once identified the position of the variable delay line correspondent to pulses synchronization (maximum SFG signal) the experiment can start. Two images were acquired for each investigated position of the variable delay line, the first with only OPO beam illumination and the second with both beams illumination. To prove the presence of depletion produced by the incoming pump beam of spontaneous fluorescence excited by OPO beam, the fluorescence signal in the second image f_{depl} must be lower than the one measured in the first image, f_{exc}. The measurements are performed through the software *ImageJ*. In Figure 4.30 the values of the ratios $\frac{f_{depl}}{f_{exc}}$ are plotted as a function of the pulses delay, considering that $\Delta t = \frac{2\Delta x}{c}$, where Δx represents the variable delay line position.

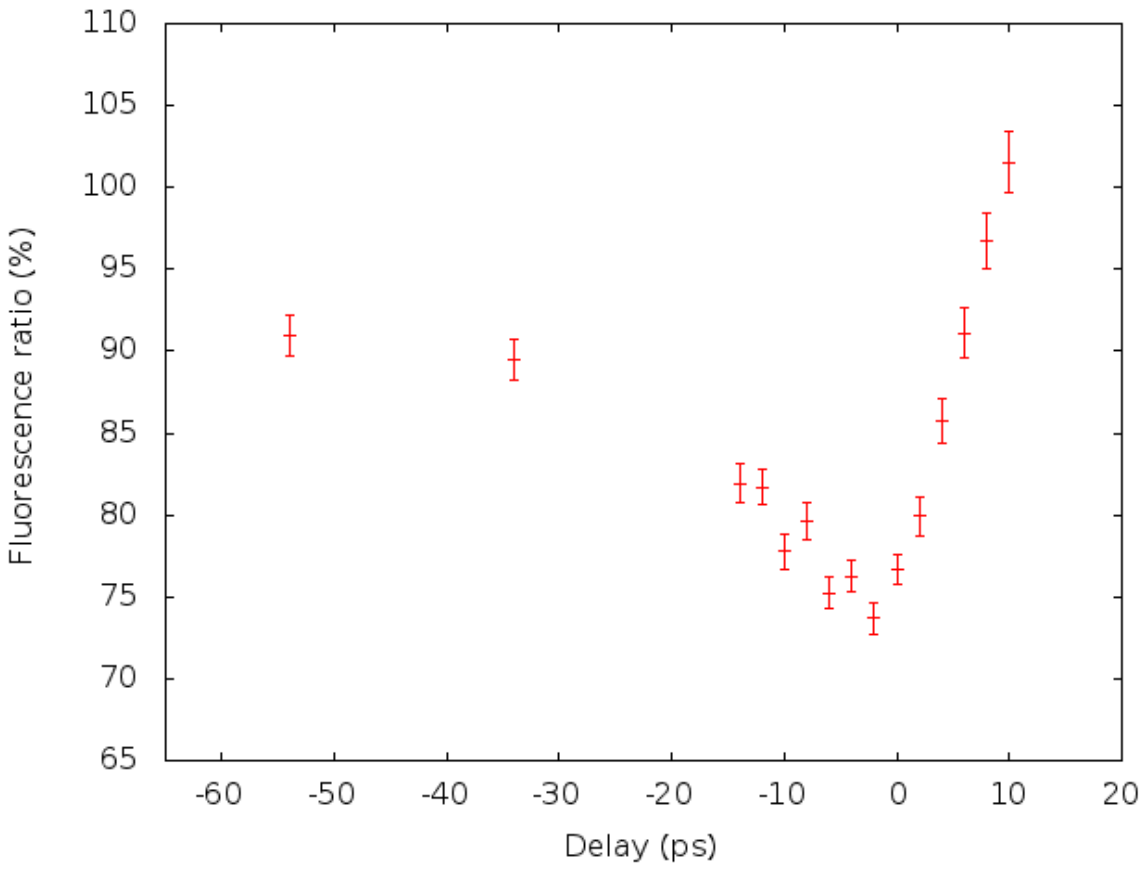

Figure 4.30 Depletion efficiency as a function of the delay between the pulses

After positioning the variable delay line in correspondence to the maximum depletion efficiency, a streaming is recorded: the OPO beam is always incident in the sample, while the pump beam is started and stopped continuously. The fluorescence signal trend is affected by time-dependent fluorophore bleaching, as can be seen in Figure 4.31. The correction that must be applied to emission intensity over time can be computed thanks to an exponential fit of data acquired with OPO illumination only.

The parameters of the fit $f(x) = a + be^{-\frac{x}{c}}$ are:

a = (386 $\pm$ 4) a.u.
b = (1490 $\pm$ 5) a.u.
c = (18.1 $\pm$ 0.2) s^{-1}

c is an estimation of the characteristic time of Alexa Fluor 594 bleaching. Knowing the time-dependent law that exponentially reduces fluorescence emission without the depletion effect,

data can be compensated by a normalization with the curve $f(x)$. The result is displayed in Figure 4.32.

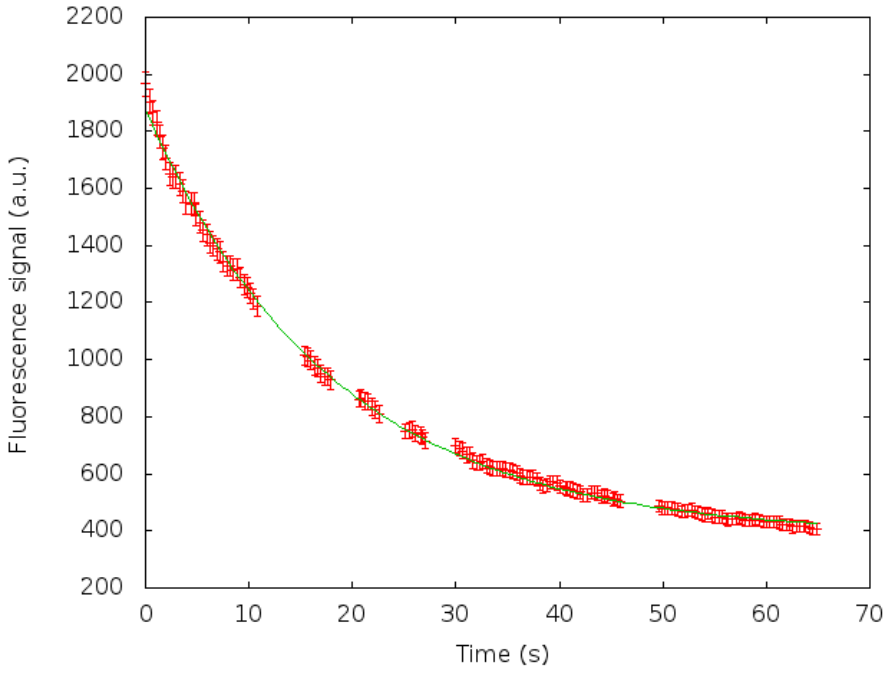

Figure 4.31 Bleaching of Alexa Fluor 594

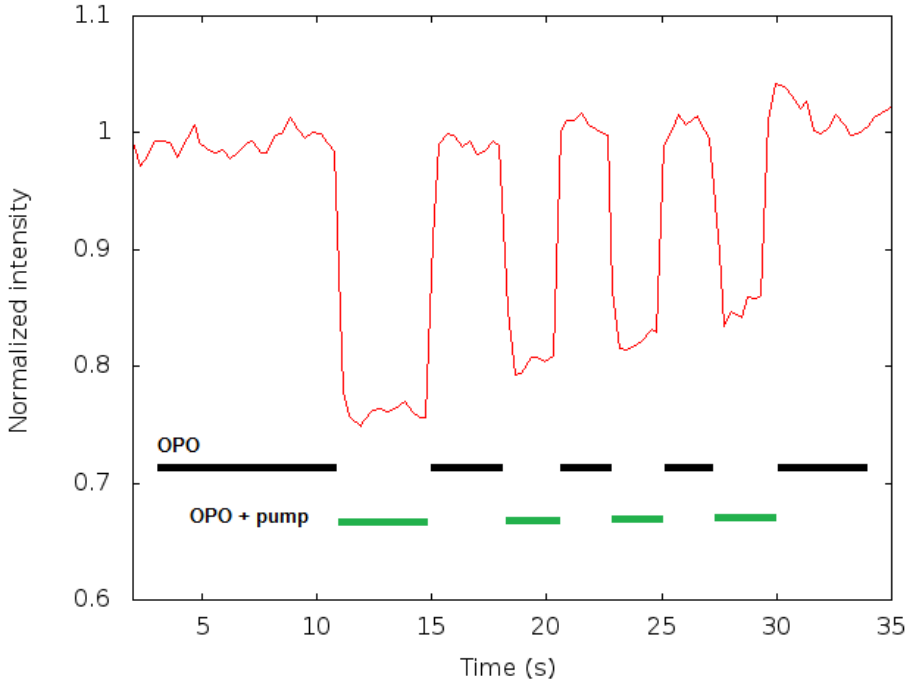

Figure 4.32 Streaming of Alexa Fluor fluorescence emission with occasional pump beam induced depletion

The graphs presented demonstrate that the imaging setup has been set in conditions of performing STED nanoscopy. It is proper to note that the present configuration do not actually provides a good depletion efficiency, in fact the maximum obtained fluorescence reduction is (26 $\pm$ 5) %.

5 DISCUSSION AND FUTURE PERSPECTIVES

In the present work, an optical imaging setup suitable for multiphoton microscopy in living models has been optimized to perform advanced imaging techniques, i.e., multicolor multiphoton and STED. The setup is composed of a laser scanning multiphoton microscope (Thorlabs) equipped with two synchronized high power femtosecond laser sources (Coherent), namely a mode-locked Ti:Sapphire laser that is used to pump an optical parametric oscillator (OPO). The basic imaging configuration is the classical two-photon excitation (2PE), which can be performed simultaneously by the two laser sources. The advantage of using 2PE in biomedical research relies on the use of higher wavelengths compared to single-photon excitation. Photons with higher wavelengths, typically in the near-infrared range (760 nm -1300 nm), cause less photodamage in biological specimen and are less exposed to scattering, yielding to a deeper penetration in biological tissues. Furthermore, providing temporal and spatial overlapping between the two laser pulses in the focal plane generates nonlinear processes in the fluorescent sample. We can refer to these processes (sum frequency generation, multicolor two-photon excitation) as "two-beam" processes, because they are produced by the combination of the two provided excitation wavelengths. Of course they add up to other nonlinear processes generated by single beam illumination ("single-beam" processes, as two-photon excitation or higher harmonic generation). The optimization of performances of the imaging apparatus is aimed to reach the capability of producing a selection of optical processes as wide as possible, in order to image the highest number of features in biological samples. An imaging setup with those capabilities can pave the way for further studies in the biomedical field, in particular in the imaging of tumor microenvironment in live animals. The resolution of multiphoton scanning microscopy is typically 30% poorer than single-photon confocal scanning microscopy, therefore an additional improvement of the apparatus performance is the integration of multiphoton microscopy with stimulated emission depletion (STED) nanoscopy. This recent sub-diffraction resolution imaging technique will provide confinement of the two-photon excitation point spread function (PSF) in a volume of few tens nanometers, the actual inferior optical resolution limit.

The setup optimization started from the correct installation of the beams power modulation system. Power modulation is realized by means of electro-optic devices, the Pockels cells, which require different voltages for DC and AC supply according to the beams wavelength selected at source. DC voltage sets the starting operating point of the device, while AC voltage is effectively responsible for the output power variation. The output power is expected to range from a minimum value P_{min} (always higher than zero) to the maximum value P_{max} (always lower than the source output). The optimization of Pockels cells transmittance consists in finding the

supply values which maximize the output power range, namely the difference between P_{min} and P_{max}. The result of the optimization procedure has been the construction of a look-up table containing the DC and AC values that must be set before the beginning of each experiment depending on used wavelengths, in order to obtain the best device transmittance at 100% of power.

Since multiphoton microscopy technique requires a precise spatial and temporal overlap of the two laser trains, a great attention was put in the beams alignment procedures. The two beams travel along different paths on the optical bench enclosed by the setup, but must enter in the microscope perfectly coaxial to be focused in the same spatial region in the specimen. This condition is reached by manipulating manually the beams conditioning optics, with the support of fluorescent test targets to visualize the beam and a power thermal sensor. The path length of one beam can be varied through the movement of two mirrors placed on a rail, with a precision of 1 μm. This is a fundamental tool which allows to synchronize one pulse with respect to the other. A first temporal alignment is performed detecting the pulses temporal profile through a fast detector and observing the output at the oscilloscope. In particular the beams alignment procedure must be repeated over time to keep the alignment quality, which deteriorates because of drift and vibrations.

The fluorescence signal acquisition constitutes another field in which the imaging setup can be optimized. The pump source Ti:Sapphire provides impulses at 80 MHz repetition rate, while the acquisition board sampling is carried out in internal trigger at 125 MHz frequency. The board is equipped also with an external trigger input with software-selectable level, thus the optimized condition for fluorescence signals acquisition is synchronization between the sampling at 80 MHz rate and the fluorophore maximum emission (immediately after excitation). The external trigger signal at 80 MHz repetition rate can be extracted directly from the pump source output. The synchronization condition was identified thanks to measurements of fluorescence signal from the fluorophore Alexa Fluor 568 in a fixed biological sample, by varying the phase of the signal sent to the external trigger input of the acquisition board. The phase retardation is performed through a retarder circuit with a variable capacity. Since the lifetime is characteristic of each fluorophore, one can expect to find different phase shifts that yield to the synchronization condition for different fluorophore; however, the result of synchronization experiment for Alexa Fluor 568 demonstrate that optimization of the acquisition produces an enhancement of the detected fluorescence signal around 20%.

The objective used on the microscope must be suitable for advanced multiphoton applications as two-color two-photon microscopy and STED nanoscopy. Two multiphoton objectives, Nikon and Olympus, were tested on the laboratory to determinate the one that best meets our requirements. The tests was aimed primarily to identify which objective exhibits the best

correction of chromatic aberrations because we need good spatial overlap between the focal spots of the two beams in the sample, both in multicolor multiphoton microscopy and STED nanoscopy. The measurement was performed through some z-stacks of a single quantum dot, namely series of images captured in the same field of view at different z-planes inside the specimen separated by an axial regular pitch. At every step the quantum dot was illuminated by first by one beam and then by the other and two images were acquired, so that two images series relative to different wavelengths were produced. Plotting the z-axis intensity profile of the two series, the information about the distance of the two foci is extracted. For each tested wavelengths couple the distance between the foci is lower for Olympus objective, which reveals a higher achromaticity, optimized for the couple 800 nm -1000 nm. Furthermore, the axial and lateral extents of the objective PSF were estimated analyzing the previous images. The smaller is the spatial volume occupied by 3D-PSF, the better is the imaging system resolution. On average, the axial size of Olympus PSF is around 40% narrower than the Nikon one. As concerns the lateral size of PSF, the average diameter of the PSF at the focal plane is comparable for Nikon and Olympus objectives at smaller wavelengths (800 nm), while the Nikon diameter measures nearly twice the Olympus one at higher wavelengths (1200 nm). Finally, a relative transmittance measurement is taken into account. Olympus transmittance is about 10% superior to the Nikon one in the range 700 – 1000 nm, while Nikon transmittance is about 9% higher in the range 1025 – 1200 nm; at higher wavelengths the two are comparable. In this case, looking forward to implement in the setup STED nanoscopy functionality, the beam responsible of the depletion must have as much power as possible to increase process probability. The best choice is to privilege higher transmittance in the lower wavelength range, in fact the depletion wavelength must be within the fluorophore emission spectrum, namely more in the range 700-900 nm than at higher wavelengths. Thanks to all previous results the choice for more suitable objective is directed towards Olympus objective.

The setup was set in conditions of spatial and temporal overlap of laser trains, so that two-beam multiphoton processes can be produced in the observed specimen. The quality spatial and temporal alignment was first tested on KDP powder, a not fluorescent and not biological sample. KDP crystals illuminated by a certain wavelength produce second harmonic generation signals; if two beams with different wavelengths are focused around the same geometrical point and synchronized, the nonlinear phenomenon of sum frequency generation is observed: the two waves frequencies sum up to provide a third equivalent wavelength; the result is the simultaneous detection of three colors signals. After this achievement, the multicolor multiphoton potentialities of the imaging apparatus were tried in preliminary tests on fluorescent samples. The simultaneous absorption of a photon belonging to the first beam and one coming from the second beam permits to excite a fluorophore whose absorption spectrum is intermediate between the two excitation beams wavelengths.

With regard to the implementation of STED nanoscopy technique in the setup, the first step has been the injection of one beam inside a single-mode optic fiber with 5 μm core diameter for the required temporal stretching of the pulse aimed to spontaneous fluorescence depletion. Two focusing optic elements were tried for the beam injection in the fiber, a doublet and an objective. Both reached in optimized conditions essentially the same efficiency in the beam-fiber coupling, around 40%. This suggests that at present the quality of the coupling depends more on the sensibility limit that can be reached in manual alignment of the optics and on the precision of the mounting elements available on the bench (up to 0.5 μm). Since fluorescence depletion phenomenon in biological samples requires at least 50 mW on the back focal plane of the objective, a possible future improvement for beam injection in the fiber is represented by the automatization of the fiber entrance alignment with respect to the beam optic axis. An automatic 3-axis fiber launch with higher precision could increase the fiber coupling efficiency and reduced significantly the time spent for manual alignment.

The final significant achievement was the observation of depletion effect in a fluorescent sample (Alexa 594). The test clearly confirm that the apparatus has the capability to perform imaging at the nanoscale resolution, once the depletion effect is combined with the modulation of the pump beam wavefront by the phase plate.

In conclusion, the performance of many critical parts in the setup is now optimized (beam power modulation system, temporal synchronization of pulses, fluorescence signal acquisition). The imaging apparatus in able to perform with ease two-beam multicolor microscopy, over the basic 2PE microscopy. The future goal is to accomplish the integration of multiphoton imaging with the super-resolution STED technique. In particular, a first experiment that can be accomplished is the imaging of a fixed biological specimen with very small structures (for example mitochondria), adding the phase plate for pump beam wavefront modulation to the setup configuration needed to obtain depletion. Depletion efficiency, currently amounting to 26%, can be improved by further optimization of the beam power in output from the fiber and improving the chromatic aberration correction.

The combination of multicolor multiphoton imaging and STED techniques would bring the instrument to a powerful configuration for the study of *in vivo* biological processes at the nanoscale, simultaneously observing many different features of the specimen. An imaging setup with these capabilities is currently missing in Padova, and we believe it could achieve a better understanding of signal pathways in the tumor microenvironment.

BIBLIOGRAPHY

1. *Erlauterungstaflen zur Physiologie und Entwicklungsgeschichte.* **Wagner, R.** 1839.

2. *Observation on living preformed blood vessels as seen in the trasparent chamber inserted into the rabbit's ear.* **Clark, , E. R. and Clark, E. L.** 49, 1932, Am. J. Anat. , p. 441-477.

3. *Preclinical intravital microscopy of the tumor stroma interface: invasion, metastasis and therapy response.* **Alexander, S. et al.** 2013, Current Opinion in Cell Biology , Vol. 25, p. 659-671.

4. *Memoir on inventing the confocal scanning microscope.* **Minsky, L.** 4, 1988, Scanning, Vol. 10, p. 128-138.

5. *Confocal scanning light microscopy with high aperture immersion lenses.* **Brakenhoff, G. J., Blom, P. and Barends, P.** 2, 1979, Journal of Microscopy , Vol. 117, p. 219-232.

6. *How the confocal laser scanning microscope entered biological research.* **White, W. B. and Amos, J. G.** 6, 2003, Biology of the cell, Vol. 95, p. 335-342.

7. *Photon upmanship: why multiphoton imaging is more than a gimmick.* **Svoboda, W. and Denk, K.** 1997, Neuron, Vol. 18, p. 351-357.

8. *Principles of two photon excitation microscopy and its applications to neuroscience.* **Yasuda, K. and Svoboda, R.** 6, 2006, Neuron, Vol. 50, p. 823-839.

9. *Two-photon laser scanning fluorescence microscopy.* **Denk, W., Strickler, J. H. and Webb, W.W.** 1990, Science, Vol. 248, p. 73-76.

10. *Nonlinear magic: multiphoton microscopy in the biosciences.* **Zipfel, W. R., Williams, R. M. and Webb W. W.** 11, 2003, Nature Biotechnology, Vol. 21, p. 1369-1377.

11. *Ueber elementarakte mit zwei Quantenspruengen.* **Goeppert-Mayer, M.** 1931, Ann. Phys., Vol. 9, p. 273.

12. ***Garrett, Kaiser.*** *1961.*

13. Multiphoton excitation provide optical sections from deeper within scattering specimens than confocal imaging. ***White, V. E. and Centoze, J. G.*** *1998, Biophysical journal, Vol. 75, p. 2015-2024.*

14. In vivo developmental biology study using noninvasive multi-harmonic generation microscopy. ***Chu, S. W. et al.*** *23, 2003, Optics express, Vol. 11, p. 3093-3099.*

15. Nonlinear Optics. ***Boyd, R. W.***

16. ***Franken.*** *1961.*

17. Application of a femtosecond self-sustaining mode-locked Ti:sapphire laser to the field of laser scanning confocal microscopy. ***Curley, P. F. et al.*** *8, 1992, Optical and Quantum Electronics, Vol. 24, p. 851-859.*

18. 3D microscopy of transparent objects using third-harmonic generation. ***Muller, M. et al.*** *3, 1998, Journal of Microscopy, Vol. 191, p. 266-274.*

19. Multicolor two-photon tissue imaging by wavelength mixing. ***Mahou, P. et al.*** *8, 2012, Nature Methods, Vol. 9, p. 815-818.*

20. Two-color two-photon Excitation of Indole. ***Gryczynski, I. et al.*** *1996, Biospectroscopy, p. 97-101.*

21. Breaking the diffraction resolution limit by stimulated-emission-depletion fluorescence microscopy. ***Hell, S. W. and Wichmann, J.*** *11, 1994, Optics Letters , Vol. 19.*

22. On the quantum theory of radiation. ***Einstein, A.*** *1917, Phys. Z., Vol. 18, p. 121-128.*

23. Live-cell superresolution imaging by pulsed STED two-photon excitation microscopy. ***Takasaki, K. T., Ding, J. B. and Sabatini, B. L.*** *2013, Biophysical Journal, Vol. 104, p. 770-777.*

24. STED microscopy reveals crystal colour centres with nanometric resolution. ***Rittweger, E. et al.*** *2009, Nature Photonics, Vol. 33, p. 144-147.*

25. Imaging hallmarks of cancer in living mice. ***Ellenbroek, S. I. J. and van Rheenen, J.*** *2014, Nature, Vol. 14, p. 406-418.*

26. Long-term, high-resolution imaging in the mouse neocortex through a chronic cranial window. ***Holtmaat, A. et al.*** *8, 2009, Nature Protocols, Vol. 4, p. 1128-1144.*

27. Intravital imaging reveals p53-dependent cancer cell death induced by phototherapy via calcium signaling. ***Giorgi, C. at al.*** *3, 2014, Oncotarget, Vol. 6, p. 1435-1445.*

28. Advances in multiphoton microscopy technology. ***Hoover, E. E. and Squier, J. A.*** *2013, Nature Photonics, Vol. 7, p. 93-101.*

29. Video-rate resonant scanning multiphoton microscopy: An emerging technique for intravital imaging of the tumor microenvironment. ***Kirkpatrick, N. D. et al.*** *1, 2012, IntraVital, Vol. 1, p. 60-68.*

30. High-throughput spatial light modulation two-photon microscopy for fast functional imaging. ***Pozzi, P. et al.*** *1, 2015, Neurophotonics, Vol. 2.*

31. Multiphoton imaging microscopy at deeper layers with adaptive optics control of sperical aberration. ***Bueno, J. M. et al.*** *1, 2014, Journal of Biomedical Optics, Vol. 19.*

32. Imaging cell biology in live animals: ready for prime time. ***Weigert, R., Porat-Shliom, N. and Amornphimoltham, P.*** *7, 2013, Journal of cell biology, Vol. 201, p. 969-979.*

33. Electro-optic devices in review. ***FastPulse Technology, Inc. Lasermetrics Division.*** *1986, Lasers and Applications.*

34. Pockels cell primer. ***Goldstein, Robert.*** *Laser Focus Magazine.*

35. Incorporation of a highly luminescent semiconductor quantum dot in ZrO2-SiO2 hybrid sol-gel glass film. ***Bullen, C. et al.*** *14, 2004, Journal of Materials Chemistry, p. 1112-1116.*

36. Fundamentals of Photonics . ***Saleh, B. E. A. and Teich, M. C.*** *s.l. : Wiley, 2007.*